



WILLIAM & MARY

CHARTERED 1693

W&M ScholarWorks

Dissertations, Theses, and Masters Projects

Theses, Dissertations, & Master Projects

1996

Propagation of guided acoustic waves in composite media

Michael David Seale

College of William & Mary - Arts & Sciences

Follow this and additional works at: <https://scholarworks.wm.edu/etd>

 Part of the Acoustics, Dynamics, and Controls Commons, and the Materials Science and Engineering Commons

Recommended Citation

Seale, Michael David, "Propagation of guided acoustic waves in composite media" (1996). *Dissertations, Theses, and Masters Projects*. Paper 1539623884.

<https://dx.doi.org/doi:10.21220/s2-yfgk-5y37>

This Dissertation is brought to you for free and open access by the Theses, Dissertations, & Master Projects at W&M ScholarWorks. It has been accepted for inclusion in Dissertations, Theses, and Masters Projects by an authorized administrator of W&M ScholarWorks. For more information, please contact scholarworks@wm.edu.

INFORMATION TO USERS

This manuscript has been reproduced from the microfilm master. UMI films the text directly from the original or copy submitted. Thus, some thesis and dissertation copies are in typewriter face, while others may be from any type of computer printer.

The quality of this reproduction is dependent upon the quality of the copy submitted. Broken or indistinct print, colored or poor quality illustrations and photographs, print bleedthrough, substandard margins, and improper alignment can adversely affect reproduction.

In the unlikely event that the author did not send UMI a complete manuscript and there are missing pages, these will be noted. Also, if unauthorized copyright material had to be removed, a note will indicate the deletion.

Oversize materials (e.g., maps, drawings, charts) are reproduced by sectioning the original, beginning at the upper left-hand corner and continuing from left to right in equal sections with small overlaps. Each original is also photographed in one exposure and is included in reduced form at the back of the book.

Photographs included in the original manuscript have been reproduced xerographically in this copy. Higher quality 6" x 9" black and white photographic prints are available for any photographs or illustrations appearing in this copy for an additional charge. Contact UMI directly to order.



A Bell & Howell Information Company
300 North Zeeb Road, Ann Arbor MI 48106-1346 USA
313/761-4700 800/521-0600



PROPAGATION OF GUIDED ACOUSTIC WAVES IN COMPOSITE MEDIA

A Dissertation

Presented to

The Faculty of the Department of Physics

The College of William and Mary in Virginia

In Partial Fulfillment

Of the Requirements for the Degree of

Doctor of Philosophy

by

Michael David Seale

July, 1996

UMI Number: 9707509

**UMI Microform 9707509
Copyright 1996, by UMI Company. All rights reserved.**

**This microform edition is protected against unauthorized
copying under Title 17, United States Code.**

UMI
300 North Zeeb Road
Ann Arbor, MI 48103

APPROVAL SHEET

This dissertation is submitted in partial fulfillment of
the requirements for the degree of

Doctor of Philosophy

Michael D. Seale
Michael D. Seale

Approved, July 1996

Barry T. Smith
Barry T. Smith, Chair

R. L. Champion
Roy L. Champion

Carl E. Carlson
Carl E. Carlson

Dennis M. Manos
Dennis M. Manos

Mark K. Hinders
Mark K. Hinders
Department of Applied Science

Table of Contents

Acknowledgments	vi
List of Tables	vii
List of Figures	ix
Abstract	xiv
1 Introduction	2
2 Composites	11
2.1 Types of Composites	12
2.2 Fibers and Matrices	13
2.2.1 Fibers	14
2.2.2 Matrices	15
2.2.3 Continuous Fiber/Polymer Matrix Composites	16
2.3 Fabrication and Identification	17
2.3.1 Fabrication	17
2.3.2 Classification	18
2.4 Composite Applications.....	19
2.4.1 Military Aircraft.....	21
2.4.2 Commercial Aircraft	22
2.4.2.1 Boeing.....	22
2.4.2.2 Douglas.....	23
2.4.2.3 High-Speed Civil Transport	23
2.4.3 Other Composite Applications.....	26
3 Acoustic Waves in Solids	28

3.1	One-Dimensional Spring Model of a Continuous Material	29
3.2	Definitions and the Development of Elastic Equations	32
3.2.1	Particle Displacement, Deformation, and Strain Defined	32
3.2.2	Abbreviated Subscript Notation	37
3.2.3	Stress	38
3.2.4	Elastic Constants and the Stress-Strain Relation	42
3.2.5	Bond Transformation Properties	45
3.2.6	One-Dimensional Example	48
3.3	Guided Waves	50
3.3.1	Development of Equations	50
3.3.2	Low Frequency Limit	60
4	Numerical Modeling	64
4.1	Finite Element Model	64
4.2	Evaluation of Numerical Model	75
4.3	Influence of the Elastic Constants on the Dispersion Curves	81
5	Experimental Techniques	86
5.1	Generation and Detection of Lamb Waves	86
5.1.1	Lead Break Source	87
5.1.2	Tone Burst Excitation of Lamb Modes	91
5.2	Velocity Measurements	95
5.2.1	Distance Measurements	98
5.2.2	Time Measurements	98
5.2.3	Comparison of Lead Break and Tone Burst Velocities	100
5.3	Immersion Method	103
6	Lamb Wave Monitoring of Damage in Composites	108
6.1	First Fatigue Damage Study	109
6.1.1	Samples	109
6.1.2	Fatigue Process	112
6.1.3	Contact Measurement	113

6.1.4	Contact Results	114
6.1.5	Immersion Measurement	119
6.1.6	Immersion Results	120
6.1.7	Discussion	124
6.2	Second Fatigue Damage Study	125
6.2.1	Samples	126
6.2.2	Fatigue Process	127
6.2.3	Velocity and Crack Density Measurements	127
6.2.4	Results	129
6.2.5	Discussion	136
6.3	Thermal Damage	137
6.3.1	Samples	138
6.3.2	Velocity Measurement	138
6.3.3	Results	139
6.3.4	Discussion	144
6.4	Combined Thermal and Mechanical Damage	144
6.4.1	Samples	145
6.4.2	Thermal-Mechanical Cycling	146
6.4.3	Velocity Measurements	151
6.4.4	Results	154
6.4.4.1	Results From the Boeing Samples	154
6.4.4.2	Results From the Douglas Samples	156
6.4.5	Discussion	160
7	Summary and Conclusions	162
Appendices		167
A	Relationship Between the Engineering Constants and the C_{IJ} 's	167
B	Computer Program for Calculating Dispersion Curves	171
Bibliography		187
Vita		194

Acknowledgments

I would like to express my appreciation to Barry Smith for his guidance, insight, and, most of all, for his enthusiasm in this project. Thank you for making the many years of work enjoyable. I would also like to thank the members of my committee for their reading and criticism of this manuscript. They include: Barry Smith, Roy Champion, Carl Carlson, Dennis Manos, and Mark Hinders. I am also indebted to Bill Prosser of NASA Langley Research Center in Hampton, Virginia for his wisdom, assistance, reading and criticism of this manuscript, and the many hours of consultation during the time I spent conducting research at NASA Langley. Thanks also to John Masters of Lockheed Engineering and Sciences in Hampton, Virginia for his assistance in obtaining the composite samples used in two of these studies. Additionally, I would like to thank the personnel in the Nondestructive Evaluation Sciences Branch at NASA Langley for all of the help and providing a comfortable work environment. In particular, I would like to thank Ken Hodges for his assistance in the lab and for keeping things fun.

I wish to express thanks to the Physics Department at William and Mary. My interactions with the faculty and staff have benefited me both intellectually and personally. Thanks to thank Paula, Sylvia, and Dianne for taking good care of me and keeping me in line. Thanks also to the many graduate students with whom I have spent the last six years of my life.

I would also like to express my appreciation to those individuals who wrote the many letters of recommendation for me during my job search. They include: Barry Smith, Marc Sher, Bill Prosser, and Vernon Easterling of Wabash College. Thanks also to Bob Welsh for all of his advice and help during my job search.

There are many individuals outside the academic world to whom I would like to express my thanks. Thanks to Cecilia Williams for her love, concern, and support over the past year. Thanks to Tracy Camp for being a wonderful friend for many years and allowing me to win so many racquetball games. Thanks to Lewis Edwards, Bonnie Christie, and to everyone else with whom I played volleyball.

Finally, I would like to express my most sincere appreciation to my family. Thanks to my mother, father, brother, and grandmother for believing in me and supporting my endeavors. I would especially like to thank my parents for their faith, prayers, guidance, and inspiration. Their love and support meant a great deal me and I could not have done this without them.

List of Tables

2.1	Properties of various composite fibers (from reference 2).....	14
2.2	Various matrices and their intended maximum operating temperatures (from reference 2).	15
2.3	Advantages and disadvantages of thermoplastic polymers (from reference 44).	16
2.4	Properties of metals versus those of some common composites, where the strength and modulus are taken along the fiber direction for the composites (from reference 2).....	17
2.5	Classification of composites includes: (a) the name, designated by the manufacturer [2], and (b) the fiber orientation.....	20
4.1	Material properties for an AS4/3501-6 composite (from reference 2).	78
4.2	Comparison of material properties obtained from the manufacturer (Row 1) versus those obtained using experimental Lamb wave velocity measurements (Rows 2 and 3). Data is from reference 28.....	81
5.1	Tone burst velocity measurements versus lead break velocity measurements for nine composite samples with the same architecture.....	102
6.1	Results for two samples loaded to failure.	112
6.2	Data for various samples loaded to a terminal number of cycles.	114
6.3	Data from samples fatigued 10^n cycles.	117
6.4	Results from four samples loaded to failure.	126
6.5	Data for fatigue samples.	130
6.6	Data for the thermally damaged samples.....	140
6.7	Engineering constants [†] and associated elastic stiffness parameters.	141

6.8	Engineering constants [†] and associated elastic stiffness parameters for the Boeing samples.	147
6.9	Engineering constants [†] and associated elastic stiffness parameters for the Douglas samples.	147
6.10	Description of HSR test samples.....	151
6.11	Baseline velocity measurements for the Boeing samples.	155
6.12	Velocity measurements for the Boeing samples which have had fatigue time.	155
6.13	Velocity data for Douglas samples 1-4.	157
6.14	Velocity measurements for remaining Douglas samples.....	159

List of Figures

2.1	Various types of composites include: (a) particle composites with reinforcing stiffeners varying in size and shape and (b) continuous fiber composites with unidirectional and woven architectures.	13
2.2	Construction of composite showing an individual unidirectional lamina, a stacking sequence, and the finished laminate.	19
2.3	Composite materials are used in both (a) the X-29A fighter and (b) the B2 stealth bomber. Images downloaded from references 46 and 47, respectively.....	21
2.4	The Darkstar is made almost entirely of composite materials. Image downloaded from reference 48.	22
2.5	A composite horizontal stabilizer to be used in the Boeing 777. Reproduced with permission from reference 3. Copyright by Advanstar Communications, Inc.....	24
2.6	Composites use in the Boeing 777. Reproduced with permission from reference 3. Copyright by Advanstar Communications, Inc.....	24
2.7	Composites use on the proposed Douglas MD-12X. Reproduced with permission from reference 3. Copyright by Advanstar Communications, Inc.	25
3.1	A three-dimensional spring model for an elastic solid.	28
3.2	One-dimensional model of particles connected by massless springs to approximate an elastic solid (from reference 54).	30
3.3	Differential particle displacement, du , defined for a solid in a deformed state (from reference 55).	33
3.4	Rigid body rotation demonstrating that the vector quantity, du , does not reduce to zero for such cases (from reference 55)....	35

3.5	Traction forces, \mathbf{T}_i , acting on each face of a volume element (from reference 55).	39
3.6	An acoustic wave travelling in a plate (from reference 56).	51
3.7	Two classes of Lamb waves: (a) symmetric and (b) antisymmetric. The solid lines indicate the displacement field in the z -direction and the dotted lines indicate the displacement field in the x -direction.	58
3.8	Dispersion curves for aluminum showing the first few symmetric (S_i) and antisymmetric (A_i) modes.	59
3.9	Particle displacements u_x (solid) and u_z (dashed) showing the symmetry of the first two Lamb modes in aluminum: (a) S_0 and (b) A_0	60
3.10	Plot of the ratio of the displacements as approximated in equation (3.94) versus exact values given by equations (3.91) and (3.92) for an fd product of 0.02 MHz•mm: (a) approximate u_z/u_x for S_0 , (b) approximate u_x/u_z for A_0 , (c) exact u_z/u_x for S_0 , and (d) exact u_x/u_z for A_0	62
4.1	Finite element layer for a composite laminate.	65
4.2	Nodal displacements at the back, middle, and front of a finite element layer.	68
4.3	Demonstration of overlap of two finite element layers, where X in the figure indicates the overlap region in which the elements of the individual 6 by 6 matrices are added together.	73
4.4	Analytical solution (solid circles) versus a 5 layer numerical model (open triangles) for a 0.1 cm thick aluminum plate.	76
4.5	A 2 layer model (solid circles) versus a 5 layer model (open triangles) for aluminum showing the breakdown at higher frequencies when using fewer layers.	77
4.6	Plot of the particle displacements u_x (solid) and u_z (dashed) showing the symmetry of the first four Lamb modes in aluminum: (a) S_0 , (b) A_0 , (c) S_1 , and (d) A_1 . Note: $d = 0.1$ cm is the plate thickness..	78
4.7	Numerical dispersion curves for an AS4/3501-6, [0/90 ₃] _S composite.	79
4.8	Plot of the particle displacements u_x (solid) and u_z (dashed) through the thickness of the plate showing the behavior in the 0° and 90° plies for (a) the S_0 mode and (b) the A_0 mode.	80

4.9	The effect of reducing the various elastic stiffness constants by 20% on the dispersion curves for a unidirectional composite. The propagation direction is parallel to the fibers and the parameters reduced are: (a) c_{11} , (b) c_{13} , (c) c_{23} , (d) c_{33} , and (e) c_{55} . All of the constants were reduced in (f). In all figures, circles represent calculations with full parameters and triangles represent calculations using reduced parameters.....	83
4.10	The effect of reducing the various elastic stiffness constants by 20% on the dispersion curves for a unidirectional composite. The propagation direction is perpendicular to the fibers and the parameters reduced are: (a) c_{11} , (b) c_{13} , (c) c_{23} , (d) c_{33} , and (e) c_{55} . All of the constants were reduced in (f). In all figures, circles represent calculations with full parameters and triangles represent calculations using reduced parameters.....	84
5.1	Signals from a lead break source on top of a unidirectional composite plate (AS4/3502, [0 ₁₆]): (a) transducer 4 cm from source and (b) transducer 8 cm from source. Propagation was along the fiber direction.....	89
5.2	Signals from a lead break source on the edge of a unidirectional composite plate (AS4/3502, [0 ₁₆]): (a) transducer 4 cm from source and (b) transducer 8 cm from source. Propagation was along the fiber direction.....	90
5.3	Signals generated from a tone burst source by a longitudinal transducer on the top of a crossply composite plate (AS4/3501-6, [0/90 ₃]S): (a) transducer 4 cm from source and (b) transducer 8 cm from source. Propagation was along the 0° direction.	93
5.4	The same signal shown in Figure 5.3a, except remaining signal has been saturated to obtain a good signal-to-noise ratio for the S_0 mode.	96
5.5	Possible experimental arrangements include: (a) a lead break source, reference transducer, and second transducer at a distance x from the reference and (b) a tone burst source and pinducer array.	97
5.6	Sample signals separated by a distance of 5.5 cm. The amplitudes have been offset from each other in order to show the waveforms clearly.....	99
5.7	Cross-correlation technique for determining the time difference between signals showing: (a) the original signal, (b) the initial portion of the wave cut off for correlation, and (c) the resulting cross-correlation of the cut-off waveforms.	100
5.8	Experimental arrangement for determining dispersion curves of thin plates. .	103
5.9	Plot of (a) the reflected signal and (b) the Fourier transform, showing a minimum.	105

5.10	Experimentally determined dispersion curves for an AS4/3501-6, [0/90 ₃] _S composite. Circles represent values obtained using a 1.0 MHz transducer and triangles are those obtained using a 2.25 MHz transducer.	105
5.11	A comparison of numerical (solid circles) and experimental (open triangles) dispersion curves for an AS4/3501-6, [0/90 ₃] _S composite.	106
6.1	Plot of strain gage data to obtain (a) Young's modulus and (b) Poisson's ratio from the slope.	111
6.2	Plot of normalized modulus (solid circles) and normalized velocity squared (open triangles) versus fatigue cycles for various samples fatigued to terminal levels.	115
6.3	Photomicrographs of the edge of a composite sample: (a) without a crack and (b)-(d) with a transverse matrix crack. The magnification for each was: (a) 5.5, (b) 5.5, (c) 11.0, and (d) 28.0. The thickness of the sample is 0.12 cm....	118
6.4	Plot of normalized modulus (solid circles) and normalized velocity squared (open triangles) versus fatigue cycles for sample f1-8.	119
6.5	Experimental dispersion curves for a sample which is undamaged (solid circles) and one which has been fatigued 10^5 cycles (open triangles)....	121
6.6	Experimental dispersion curves for a sample which is undamaged (solid circles) and one which has been fatigued 10^6 cycles (open triangles)....	121
6.7	Plot of the lower two modes of the dispersion curve shown in Figure 6.6.	122
6.8	Comparison of numerical dispersion curve with c_{33} reduced by 5% in the 90° layers (solid circles) and experimental curve for a one million cycle fatigue sample with transverse matrix cracks (open triangles).	123
6.9	Comparison of lower modes of numerical curves using full parameters (solid circles) and with c_{33} reduced by 5% (open triangles).	124
6.10	Crack density versus fatigue cycles for all samples listed in Table 6.5.....	131
6.11	Normalized velocity squared versus fatigue cycles for all samples listed in Table 6.5.....	131
6.12	Calculated normalized modulus (solid line) versus normalized velocity squared (solid circles) as a function of crack density.	133

6.13	Plot of normalized modulus (solid circles) and normalized velocity squared (open triangles) for all data obtained in previous fatigue study.....	134
6.14	A plot of the normalized velocity squared for sample jm1-7 (solid circles) versus data from Dayal, et al. [23] (open triangles). Curve fits are shown for the data in this study (short dashes) and for the data of Dayal, et al. [23] (long dashes). The solid line is the theoretical modulus reduction described earlier.....	135
6.15	Plot of S_0 velocity for a range of samples exposed to different temperatures for durations of 3 minutes (solid circles) and 10 minutes (open triangles)....	140
6.16	Theoretical dispersion curves for an AS4/977-3 unidirectional composite....	142
6.17	Plot of the normalized S_0 velocity of samples exposed to different temperatures. The duration times are 3 minutes (solid circles) and 10 minutes (open triangle). Also shown (dashed lines) is the theoretically determined normalized S_0 velocity with reduced values of c_{11} , as described in the text.....	143
6.18	Plot of the dispersion curves for the 16 layer Boeing samples.....	148
6.19	Plot of the dispersion curves for the 16 layer Douglas samples.	148
6.20	A typical several hour flight profile for the temperature (dashed line) and strain (solid line) incurred by a supersonic aircraft. The temperature profile is adapted from references 71 and 72. The strain profile is adapted from reference 73.....	150
6.21	Identification of the regions for (a) the four 0° and (b) the three 90° measurements on the HSR samples. The shaded circles indicate the placement of the pinducer array.....	153
6.22	Plot of the normalized velocity in the 0° direction (solid circles) and 90° direction (open triangles) versus damage hours for the Douglas samples....	160

Abstract

Composite materials are being more widely used today by aerospace, automotive, and a number of other commercial industries because of their advantages over conventional metals. Composites are finding applications ranging from bicycle frames to the proposed High-Speed Civil Transport (HSCT). Determining the response to a variety of damage mechanisms is necessary for a complete understanding of the total use environment of composite structures. The objective of the research presented here is to provide a method of quantifying the amount of damage in composite materials for a number of different damage scenarios. Components which have non-visible damage, but have degraded performance, are of interest. At this level of damage, the safety margin designed into the structure may be compromised.

Nondestructive Evaluation (NDE) is a field of measurement physics where energy is imparted to a material and information is obtained from observing how the energy interacts with the system. Many different forms of energy can be used to obtain useful information from these measurements: acoustic, thermal, x-ray, optical, and electromagnetic. Among the many various techniques available, ultrasonic Lamb waves offer a convenient method of evaluating these composite materials. As a material is damaged, the elastic parameters of the structure change. Since the Lamb wave velocity depends on these properties, an effective tool exists to monitor damage in composites by measuring the velocity of these waves. Additionally, Lamb wave measurements are beneficial because they can propagate over long distances and are sensitive to the desired in-plane elastic properties of the material.

Presented in this study are the results involving the investigation of a variety of damage mechanisms (fatigue, thermal, and thermal-mechanical) using the Lamb wave technique. Two fatigue studies were conducted which showed that the change in modulus and change in velocity of the Lamb wave squared follow the same general trend. The Lamb wave velocity was also observed to decrease with increasing crack density. For the thermal damage study, the results showed that the velocity of the lowest order symmetric Lamb mode dropped significantly for extended thermal damage. When the experimental results were compared to model calculations, good agreement was observed for both fatigue and thermal damage. Finally, for thermal-mechanical damage, it was found that the Lamb wave technique was also able to predict a local defect in a specimen, which was later found to have a large delamination zone.

The Lamb wave velocity is a quantitative measurement and it has been shown by this work to be an effective tool in monitoring different types of damage in composites. Since the Lamb wave velocity depends on a variety of material properties, an ideal technique exists to monitor composites as damage is incurred. With the continued development of damage assessment techniques such as the Lamb wave method, the safety of such structures can be assured.

**PROPAGATION OF GUIDED ACOUSTIC WAVES
IN COMPOSITE MEDIA**

Chapter 1

Introduction

Composite materials are being more widely used today by aerospace, automotive, sports equipment, and a number of other commercial industries because of their advantages over conventional metals. Composites have a high strength-to-weight ratio and can be constructed to meet specific design needs.

Nature offers excellent examples of the efficient use of materials to satisfy design requirements. Baer, et al. [1] states that biological composites are “organized in a way that is optimized for the ultimate function and performance of the overall system.” An example of this can be seen in tendons, where stresses are almost entirely in one direction. To meet the required functional need, tendons are unidirectional in nature and have good tensile properties in one direction. Another example given by Baer, et al. [1], is that of disks in the spine. Disks are subjected to mainly compressional loads. Again, by the nature of the design, disks respond very well to compression. Nature constructs systems to meet specific design requirements and is quite efficient in this regard.

Similar techniques can be adapted to synthetic materials used today, and structures can be designed to meet the particular need of the system. Composites are inhomogeneous and anisotropic by nature and, thus, have several independent material

parameters associated with the fiber direction and the architecture of the structure.

Each of these independent parameters represents a degree of freedom for the design of a system. Besides the previously mentioned advantage of a high strength-to-weight ratio, this anisotropy also gives composite materials design advantages over isotropic metals, which have only two degrees of freedom.

Daniel and Ishai [2] note that optimization as well as design are much easier with the added degrees of freedom afforded by composites. In addition to satisfying the design specifications, composites offer weight savings over traditional metals without sacrificing strength. In fact, the specific strength (strength/density) is, in most composites, greater than that of metals [2]. With the advantages of composite materials, their use is continually increasing and becoming more widespread to a variety of fields.

Composites are finding use everywhere from bicycle frames to advanced military aircraft such as the stealth bomber [2]. Stover [3] details the increased use of composites by Airbus, Boeing, and Douglas in present as well as future designs of commercial aircraft. Composite structures are already in use in secondary parts of the Douglas MD-11, and future plans include their use in the new MD-12X. They are also now in use in primary and secondary structures on the new Boeing 777, whose maiden flight took place on June 12, 1994. Douglas' proposed MD-XX may also incorporate composite materials into primary structures such as the wings and tail. Additionally, composites have been used to repair cracks in many B-1Bs, where traditional repair techniques were not very effective, and plans have been made to reinforce all of the remaining B-1s with composite materials [4]. Further details on the extent of composite uses in these structures will be given in Chapter 2.

The NASA Advanced Composite Technology (ACT) program is another initiative which is evaluating high performance fibers and polymer matrices. It will also examine advanced architectures including 2-dimensional and 3-dimensional woven and stitched textile preforms. These materials will be used for the next generation of aerospace structures, such as the proposed High-Speed Civil Transport (HSCT). The flight profile of this aircraft will include speeds of up to Mach 2.4, altitudes of 60,000 feet, and exterior temperatures up to 200°C [1]. The materials used in the design of such a structure will need to perform well under these strenuous conditions for thousands of flight hours. Additionally, the X33/RLV (Reusable Launch Vehicle) program will rely heavily on the use of composite materials to reduce the weight and, thus, the cost of future space shuttle flights.

The Aloha Airlines accident on April 28, 1988, increased the concern for the safe operation of aircraft [5]. Fatigue and corrosion are believed to be important factors in the structural failure of the Boeing 737-200. With the increased use of advanced materials in aerospace vehicles today, the verification of the structural integrity of composite components is needed to insure safe operation of these aircraft. With this in mind, much attention has been given to understanding how composites respond to various types of damage.

O'Brien, et al. [6] and Charewicz and Daniel [7] have examined the fatigue behavior of laminates and proposed lifetime prediction models based on fatigue factors such as increased matrix cracking, delamination growth, and stiffness loss. Ogin, et al. [8,9] and Lim and Hong [10] have modeled the stiffness reduction in composites due to

the effects of matrix cracking. Laws and Dvorak [11] have investigated the progression of matrix cracking as well as stiffness loss due to transverse cracking.

In addition to fatigue, thermal degradation of composites is of concern. Street, et al. [12] have examined how composites respond to thermal damage of temperatures up to 350°C for short durations, as well as exposure times as long as 30 minutes for temperatures of 225°C. Herakovich and Hyer [13] and Ermer and Mall [14] have studied the effects on composites which were thermally cycled. The temperature range used was -250°F to +250°F in [13] and 149°C to 427°C in [14]. Stansfield and Pritchard [15] have subjected composites to rapid changes in temperature. These fluctuations, similar to the flight profile of supersonic aircraft, can lead to moisture absorption and matrix cracking. The effects of combined thermal and mechanical loading have been investigated by Griffis, et al. [16] and Schubbe and Mall [17].

With the recent development of advanced composite structures for aerospace applications, fatigue and thermal degradation have received much attention. These types of damage, as well as other damage mechanisms not mentioned, can severely affect the integrity and safety of composite aerospace structures. To track the progression of damage in aerospace structures, a convenient method to nondestructively monitor these materials needs to be developed.

Nondestructive Evaluation (NDE) is a field of measurement physics where energy is imparted to a material and information is obtained from observing how the energy interacts with the system. Many different forms of energy can be used to obtain useful information from these measurements: acoustic, thermal, x-ray, optical, and electromagnetic. A simple form of NDE is used by many individuals when finding a stud

in a wall. An example of a destructive method would be to pound a series of nail holes in the wall to probe for the stud. However, most people do not want to have to repair holes in their wall, so they opt for a nondestructive method. This common NDE technique involves knocking on the wall (imparting acoustic energy) and listening to the echo. When the material properties of the wall change, i.e. a stud is found, the echo pattern changes. Thus, by adding energy and observing how it interacts, information about the system is obtained without any detriment to the material.

Traditional NDE techniques used on metals are often not easily adaptable to composites due to the inhomogeneous and anisotropic nature of these materials. When the complexity of the material increases, the means by which the energy interacts with the system also becomes more complex. As mentioned earlier, it is the anisotropy that gives composites advantages over metals in both design and optimization. The disadvantage of adding extra degrees of freedom is that additional material properties are introduced. Therefore, the analysis of these materials becomes much more complex than that of metals.

Finding an effective means of nondestructively monitoring damage in composites is a challenging task, but it is extremely important to the safety and reliability of such structures. Several techniques are available to nondestructively evaluate damage in materials [18-20]. Salkind [18] and Stinchcomb [19] detail various methods used for damage detection in composites such as ultrasonics, X-ray radiography, thermography, and holography. In addition, Daniel, et al. [20] examined the use of ultrasonic back-scatter to monitor crack density and compared the results to those obtained using X-ray radiography.

Among the many various techniques available, ultrasonic Lamb waves offer a convenient method of evaluating these composite materials. As a material is damaged, the elastic parameters of the structure change. Since the Lamb wave velocity depends on these properties, an effective tool exists to monitor damage in composites by measuring the velocity of these waves. Additionally, Lamb waves measurements are better than conventional through-the-thickness ultrasonic measurements because they can propagate over long distances and are sensitive to the desired in-plane elastic properties of the material.

Studies have been conducted which show a reduction in Lamb wave velocity due to a loss of stiffness caused by matrix cracking [21-23]. All of the authors noted that the in-plane properties of a composite are affected by cracking and that they can be monitored through the use of Lamb waves, which travel perpendicular to the crack direction. Dayal and Kinra [21] showed that for through-the-thickness measurements, the attenuation is sensitive to cracking, while the velocity is not. For Lamb wave propagation in the plane of the plate, both wavespeed and attenuation were found to be sensitive to cracking. Tang and Henneke, [22] noted that Lamb waves provide information about the in-plane properties of a plate, and this type of measurement is more useful due to the fact that composites are commonly designed to carry in-plane loads. Similarly, Dayal, et al. [23] noted that the Lamb wave interaction with cracks is much stronger in the plane of the plate and, thus, provides an effective method to detect damage due to transverse matrix cracking.

Lamb waves are named for Horace Lamb for his studies in 1917 on guided acoustic waves in plates structures [24]. In 1957, Worlton [25] showed that Lamb waves

could be used to nondestructively inspect thin plates and cylindrical structures for defects. In 1961, Wrolton [26] experimentally confirmed the generation of Lamb waves in aluminum and zirconium.

Given the ability to nondestructively monitor materials using guided waves, studies have been conducted which use Lamb waves to monitor a variety of material properties in composite structures. Karim, et al. [27] and Mal, et al. [28] have used inversion techniques to determine the material parameters of composites from experimental Lamb wave data. Habeger, et al. [29] studied the use of plate waves to monitor the strength of paper for the purpose of monitoring quality control on line for the paper industry. Several authors [30-32] have used Lamb waves to inspect adhesively bonded joints. Lamb wave techniques have also been used to study delaminations [33-36], porosity [36,37], and fiber misalignment [37]. Recently, Lamb waves have even been used by Lee, et al. [38] to measure the temperature of silicon wafers during processing and by Pei, et al. [39] for *in situ* measurements of thin film thickness. Both of these techniques would be of interest to the semiconductor processing industry.

Lamb waves can be used to monitor a variety of different material properties. The focus of this work, however, is the use of Lamb waves to nondestructively monitor fatigue, thermal, and combined thermal-mechanical damage in composite structures. Fatigue in composites initially causes matrix cracks to develop in the material. To study the effect of cracking, several authors have examined the scattering of Lamb wave by cracks [40-43].

In addition to scattering, fatigue cracks result in a loss of stiffness. In the Lamb wave studies previously mentioned [21-23], only Tang and Henneke, [22] made modu-

lus measurements separate from the velocity measurements. They showed a change in the dispersion curve for the lowest order antisymmetric Lamb wave for both laminated and woven composites. However, to compare to the change in Lamb wave velocity, modulus measurements were only conducted on the woven samples. In contrast to these studies, the research which will be presented in this work monitors the velocity of the lowest order *symmetric* Lamb mode in laminated composites and compares the results to the modulus reduction measured using strain gages.

In the studies of Dayal and Kinra [21] and Dayal, et al. [23], the modulus was simply calculated from the velocity measurement using the approximation that the modulus is equal to the density times the square of the symmetric Lamb wave velocity. However, no separate modulus measurements were conducted to compare to the velocity measurements. In Dayal, et al. [23], the measured decrease in velocity was compared to the analytical results (based on a model) and static stiffness measurements of other authors. A noticeable difference between these measurements and the Lamb wave velocity measurements was noted. Again, in contrast to the work which will be presented here, these studies measure the lowest order symmetric Lamb wave velocity, but they do not compare velocity measurements to actual modulus measurements.

While there have been numerous studies which examine fatigue damage in composites using nondestructive techniques, few (if any) have been conducted which monitor thermal damage using ultrasonic nondestructive evaluation techniques. In the studies mentioned earlier [12-16], the effects of thermal damage were measured using mainly mechanical tests and microscopic observation. Additionally, the combined effects of thermal and mechanical damage [16,17] are of interest due to the demands

placed on present and future aerospace vehicles. Providing a method to measure thermal, as well as thermal-mechanical, degradation using ultrasonic Lamb waves would prove very useful.

In the following, Chapter 2 describes the different types of composites, nomenclature, and various applications. Chapter 3 details the theory of acoustic waves in solids and Lamb wave propagation. In Chapter 4, a review of theoretical modeling of wave propagation in plate structures is given. Also, the effects on the Lamb wave velocity due to changes in various material parameters are discussed. Chapter 5 discusses various techniques available to generate, detect, and measure the velocity of Lamb waves. Chapter 6 describes experimental procedures for detecting fatigue, thermal, and a combination of these damage mechanisms in composites. Subsequent results are discussed, and comparisons are made to model calculations. The final chapter provides the conclusions from this work.

Chapter 2

Composites

A composite structure consists of two or more materials that, when combined, yield properties which are better than those offered by the individual components. In general, metals have high strength, but they are also heavy and susceptible to corrosion. Polymers are lightweight and have good corrosion resistance, but they are not very strong. Carbon fibers have high tensile strength but a very poor response to compression. One compound alone cannot meet the requirements needed for today's aerospace structures: low weight, high strength, fatigue tolerance, and good corrosion resistance. If two or more materials can be combined to take advantage of the strengths of each of its constituents, then compounds can be manufactured which satisfy the demands of advanced aircraft as well as other structures.

Composites, combined in an effective manner, can offer weight savings, superior strength, and better corrosion resistance than conventional metal materials. It is also easier to optimize the design of complicated structures with the use of composite materials. With these obvious advantages over metals, the use of composites is continually growing. Due to the high cost and manufacturing difficulty, however, their use was originally limited to "hi-tech" structures such as advanced military aircraft and space structures. Despite the cost, composites were also used in applications where no other

material could meet the design requirements. As technology has increased and the cost decreased, the use of composites has spread into many areas: commercial transports, sports equipment, automotive components, medical applications, as well as a vast number of other fields. Additionally, near net shape manufacturing techniques that reduce machining and scrap are further decreasing costs and broadening the potential for composite applications. This chapter covers the different types of composites, fibers and matrices used in these structures, methods of manufacturing, identification and nomenclature, and the extent of use by commercial aircraft, as well as other applications.

2.1 Types of Composites

Composite materials, in general, consist of two or more distinct parts. One serves as a reinforcement, which provides the strength, and the other is called the matrix, whose job is to transfer load to the reinforcing agent. Types of composites include particle and continuous fiber structures. Particle materials have small, discontinuous reinforcements embedded within the matrix. The particles can vary in size and shape, similar to rocks in concrete, or can be short fibers, similar to straw used in ancient bricks. Continuous fiber composites consist of long fibers supported by the matrix. An example is given by reinforcement rods placed in concrete for highways and other large cement structures which provide high strength in the fiber direction. Additionally, the fibers can be woven, stitched, or laminated in various orientations to provide support in a number of directions. Various composite structures are shown in Figure 2.1.

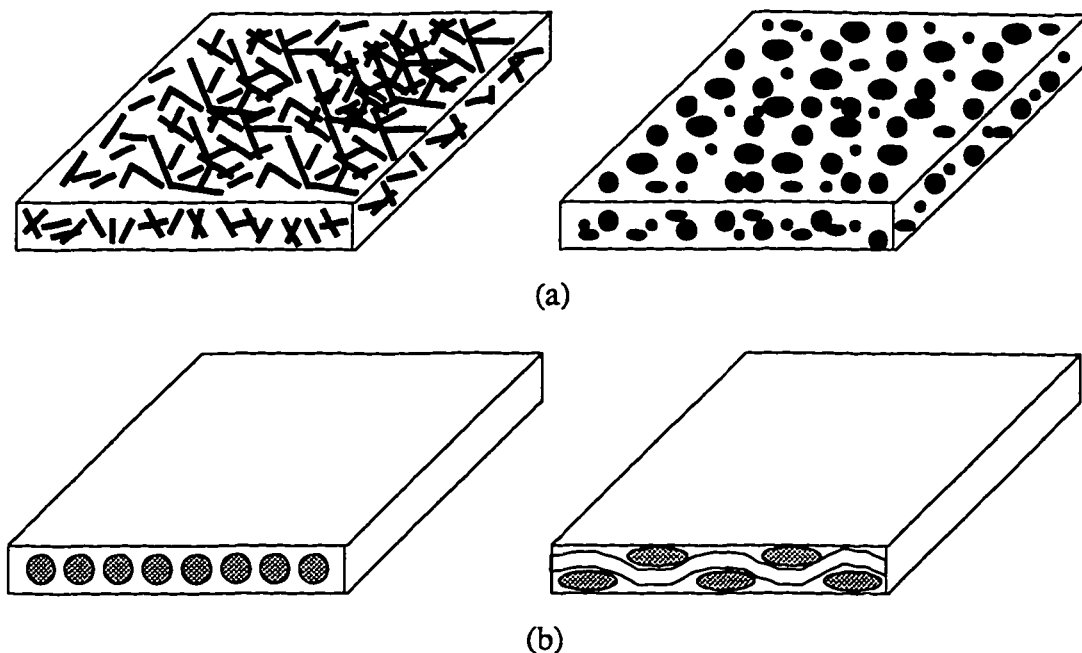


Figure 2.1 Various types of composites include: (a) particle composites with reinforcing stiffeners varying in size and shape and (b) continuous fiber composites with unidirectional and woven architectures.

Continuous fiber composites are the main type used in advanced aerospace structures. This chapter concentrates on a variety of aspects related to the use of this type of composite. As woven and advanced architecture composites become more proven and accepted, they will probably soon replace laminates. However, this discussion will be limited to laminated geometries due to the fact that these composites are still more widely used for actual applications.

2.2 Fibers and Matrices

Fibers for composite applications are made of various materials which have different tensile strengths and stiffnesses. The types of fibers include fiberglass, carbon,

ceramics, and metals. The type of matrix used depends mainly on the temperature regime and required toughness of the intended application. They include resins (polymers), metal, ceramic, and carbon.

2.2.1 Fibers

The advantages of fibers used in advanced composite materials include high strength, high stiffness, and low densities (i.e. high strength-to-weight ratio). Tensile strength of fibers can be as great as ten times that of typical metals such as aluminum, steel, and titanium. The main disadvantage is the high cost of the materials. Listed in Table 2.1 are the mechanical properties of a variety of fibers. When compared to steel [2], the strengths of the various fibers are on the order of 10 times the strength of steel (394 MPa), the moduli are comparable to that of steel (207 GPa), and the densities are 3 to 5 times less than the density of steel (7,800 kg/m³).

Table 2.1 Properties of various composite fibers (from reference 2).

Material	Tensile Strength (MPa)	Modulus (GPa)	Density (kg/m ³)
E-glass	3,450	72.5	2,540
S-glass	4,480	85.6	2,490
Carbon (AS4)	3,730	235	1,810
Carbon (IM7)	5,170	290	1,800
Graphite (T-50)	2,070	393	1,670
Kevlar	3,800	131	1,450

2.2.2 Matrices

The type of matrix used depends greatly on the intended application temperature. Polymer matrices are intended for lower temperature applications, and ceramic and carbon matrices are used where extreme operating conditions are present. Typical matrices with relative high temperature limit values are shown in Table 2.2.

Polymer matrices are widely used to support various fiber types. Polymers include thermosets, which harden as heat is applied, and thermoplastics, which soften when heated and set when cooled. Thermosets, such as epoxies and polyimides, degrade at elevated temperatures and cannot be molded or reshaped after they are initially cured. In contrast, thermoplastics soften at elevated temperatures and can be reshaped a number of times. Because of these and other advantages over thermosets, the use of thermoplastics is becoming more widespread. A list of some advantages and disadvantages of thermoplastics is shown in Table 2.3.

Table 2.2 Various matrices and their intended maximum operating temperatures (from reference 2).

Matrix	Various Types	High Temperature Limit (°C)
Polymer	Epoxy, Polyimide, and Thermoplastic	120-400
Metal	Aluminum, Titanium, and Copper	800
Ceramic	Silicon Carbide, Silicon Nitride, and Alumina	over 1000
Carbon	Carbon	2600

Table 2.3 Advantages and disadvantages of thermoplastic polymers (from reference 44).

Advantages	Disadvantages
<ul style="list-style-type: none"> • lower manufacturing cost • no cure • reprocessing (repair and recycling) • thermal shaping possible • fusion bonding possible • better performance • damage tolerance 	<ul style="list-style-type: none"> • high processing temperatures • limited processing methods • high viscosities • fiber surface treatments less developed

2.2.3 Continuous Fiber/Polymer Matrix Composites

With the obvious variety of fibers and matrices available, composites can be constructed to meet a number of different applications. Polymer matrix epoxies and polyimides are commonly used with a variety of different fibers in today's structural composites. As stated earlier, these materials have advantages over typical metals which include lower densities and high stiffness-to-weight and strength-to-weight ratios. Table 2.4 shows properties for common composites as compared to those of metals.

From the table, it can bee seen that carbon/epoxy composites offer superior properties and lower densities than metals. Because of these favorable qualities, this type of composite has found applications in many structures. The following section details the manufacturing and nomenclature of continuous fiber/polymer matrix type composites.

Table 2.4 Properties of metals versus those of some common composites, where the strength and modulus are taken along the fiber direction for the composites (from reference 2).

Material	Tensile Strength (MPa)	Modulus (GPa)	Density (kg/m ³)
Aluminum (2024 T3)	414	73	2,800
Steel (AISI 1025)	394	207	7,800
Titanium (MIL-T)	550	108	4,400
E-glass/Epoxy	1,080	39	2,100
S-glass/Epoxy	1,280	43	2,000
Carbon/Epoxy (AS4/3501-6)	2,280	142	1,580
Carbon/Epoxy (IM6/SC1081)	2,860	177	1,600

2.3 Fabrication and Identification

Continuous fiber/polymer matrix composites can be designed many ways. They can be stitched, woven, or made by laminating unidirectional layers together at various orientations. Since laminated composites are extensively used for many commercial applications, the discussion will be limited to this type of composite.

2.3.1 Fabrication

Common methods of manufacturing individual laminas of unidirectional tape include impregnation of the fibers via solution and hot-melt processes [45]. Impregna-

tion using a solution involves passing the fibers through a liquid resin bath, through rollers, and finally, through an oven. Hot-melt impregnation entails passing the fibers between sheets of paper coated with resin. The resin-fiber-resin “sandwich” is then heated and pressed together to squeeze resin between fibers and, finally, cooled.

Whichever technique is used, careful steps must be taken to make sure the fibers are well saturated and that air pockets are removed. If fibers are not well saturated, adhesion between the fiber and matrix, which is important for load transfer, may be compromised. Failure to remove air pockets causes porosity (voids in the material), and this can seriously degrade the properties of the material.

Once the individual, unidirectional laminas are made, they can be stacked together in various orientations to meet specific design requirements for an application. If strength is only needed in one direction, the laminas can be stacked with all of the fibers in the same direction to construct a unidirectional composite laminate. They can also be stacked at 90° angles to each other (crossply) or at a variety of different angles, depending on the desired design. The process of forming a composite laminate from individual laminas is shown in Figure 2.2.

2.3.2 Classification

Important features of composite laminates are the type of fiber and polymer used, the number of plies and their stacking sequence, and the fiber volume fraction (percent of the total volume occupied by the fibers). The composite is named as a fiber/matrix combination with a designation which identifies the total number and orientation of the

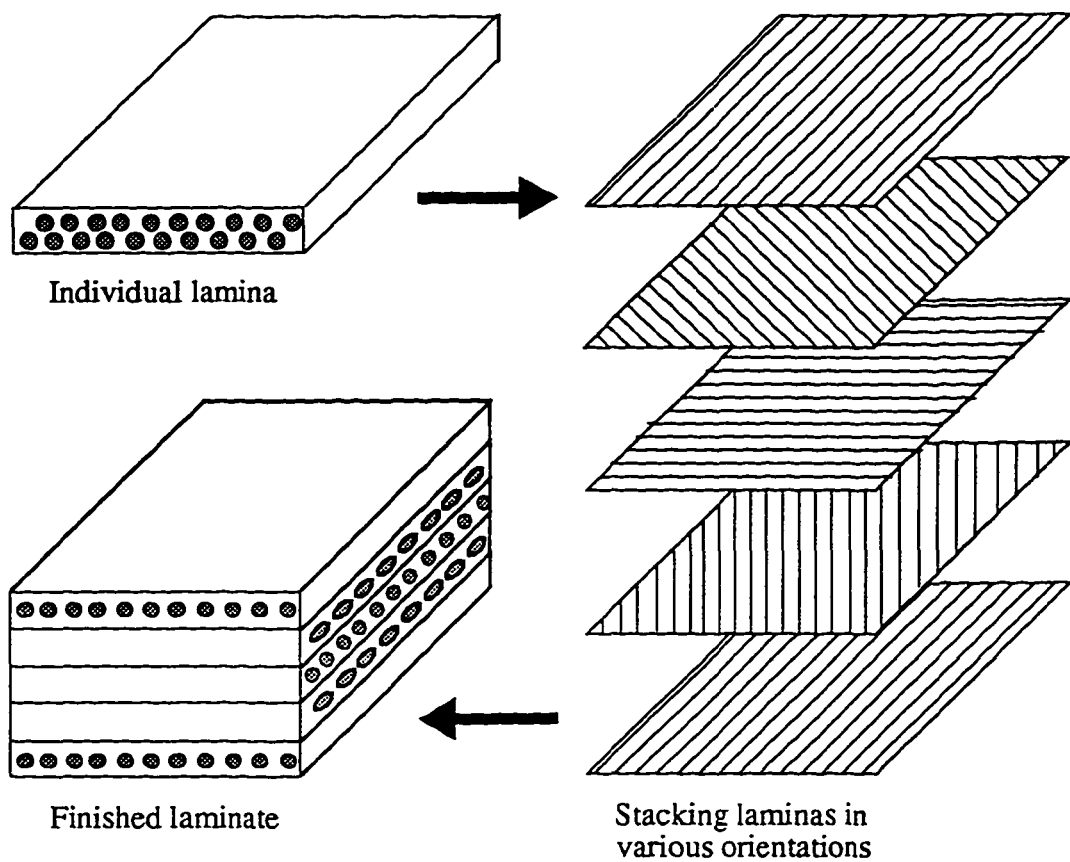


Figure 2.2 Construction of composite showing an individual unidirectional lamina, a stacking sequence, and the finished laminate.

layers. The nomenclature is shown in Table 2.5. The type of composite can, therefore, be identified by listing its fiber/matrix and its fiber orientation, i.e. AS4/3501-6 with a stacking sequence of $[0/90_2]_S$.

2.4 Composite Applications

Composites were first limited to advanced military aircraft, where high performance is at a premium. As technology has evolved and cost decreased, though, the

Table 2.5 Classification of composites includes: (a) the name, designated by the manufacturer [2], and (b) the fiber orientation.

(a) Identification of the fiber and matrix:

<u>Name</u>	<u>Fiber and Matrix</u>
AS4/3501-6	Hercules AS4 carbon fibers in a 3501-6 epoxy matrix
T300/5208	Union Carbide T300 carbon fibers in a 5208 epoxy matrix
IM7/977-3	Hercules IM7 carbon fibers in a 977-3 epoxy matrix

(b) Identification of the lamina orientation[†]:

<u>Classification</u>	<u>Layer Orientation</u>
[0 ₈]	8 layer, unidirectional: [0/0/0/0/0/0/0/0]
[0/90 ₂] _S	6 layer, crossply: [0/90/90/90/90/0]
[0/90] _{2S}	8 layer: [0/90/0/90/90/0/90/0]
[0/±45/90] _S	8 layer: [0/+45/-45/90/90/-45/+45/0]
[90 ₂ /0/±45] _S	10 layer: [90/90/0/+45/-45/-45/+45/0/90/90]

[†]The number refers to multiple layers and S refers to a symmetric stacking sequence about the mid-plane of the plate.

scope of composite applications has increased. Today, composites can be found in recreational items such as fishing poles, golf clubs, tennis rackets, and bicycle frames.

This section details a variety of uses for composite components and the importance of each particular application.

2.4.1 Military Aircraft

Composite materials are being used to meet the high speed and durability requirements of military aircraft. Flying at supersonic speeds places extreme thermal and mechanical stresses on structural components. Today's most advanced fighters and bombers are being constructed using composite components (Figure 2.3). The experimental forward-swept-wing X-29A fighter incorporates the use of advanced composite materials in its construction [46]. Structural composites are also being used in the outboard wing as well as sections of the fuselage on the B2 stealth bomber [47]. Additionally, the Darkstar unmanned reconnaissance plane (Figure 2.4), which took its maiden flight on March 29, 1996 [48], is made, with the exception of an aluminum main wing spar, completely of carbon-fiber composite materials [49]. The use of composites offers a 25% weight savings over the same structure made with aluminum, which allows the Darkstar to carry additional payload [49]. Composites are, therefore, meet-



(a)



(b)

Figure 2.3 Composite materials are used in both (a) the X-29A fighter and (b) the B2 stealth bomber. Images downloaded from references 46 and 47, respectively.

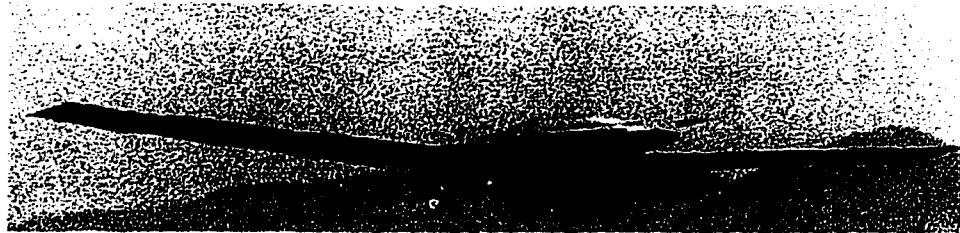


Figure 2.4 The Darkstar is made almost entirely of composite materials.
Image downloaded from reference 48.

ing the extreme requirements demanded by today's military aircraft and will continue to meet them in the future as well.

2.4.2 Commercial Aircraft

Composite applications are not limited just to military aircraft. Commercial aircraft companies are taking advantage of the unique properties of these materials as well. Airbus, in 1985, delivered a commercial aircraft with the vertical stabilizer (a primary structure) made of a composite material [3]. Airbus has also increased its composites use from 8,640 pounds (4.5% of the structural weight) on the A300-600 to over 34,000 pounds (13.0% of the structural weight) in the A340 [3]. Airbus is not the only commercial aircraft company incorporating composites into its structures, though. Boeing and Douglas are using composites in the construction of new aircraft as well.

2.4.2.1 Boeing

Boeing became the first American commercial aircraft company to make use of composites in a primary structure with the introduction of the 777. Sections of the tail,

in particular, the horizontal and vertical stabilizers, are manufactured using composite materials (Figure 2.5). In addition to the tail, extensive use is made of composites in other parts of the aircraft. Included are components such as the rudders, flaps, ailerons, elevators, and landing gear doors (Figure 2.6). In all, composites will make up roughly 10% (18,500 pounds) of the aircraft's total weight [3]. This is a dramatic increase from Boeing's past airplanes which used at most 3% composite materials.

2.4.2.2 Douglas

Douglas Aircraft Company is also making extensive use of composites in commercial aircraft. Although composites are not used in primary structures, the MD-11 contains over 10,000 pounds of composite materials [3]. The MD-12X, a proposed longer version of the MD-11, would use over 11,000 pounds of composites, but none in a primary structure (Figure 2.7) [3]. The best hope for a Douglas commercial aircraft which includes composites in primary structures is the proposed MD-XX. The plans call for a composite wing and tail, with the overall composite use totalling 35-40% of the structural weight [3].

2.4.2.3 High-Speed Civil Transport

The materials used in the proposed HSCT must meet the design specifications of carrying several hundred passengers, cargo, and sufficient fuel to fly nearly 7,000 miles [50]. Also, the aircraft will need to cruise at speeds of Mach 2.4 and fly at altitudes of



Figure 2.5 A composite horizontal stabilizer to be used in the Boeing 777. Reproduced with permission from reference 3. Copyright by Advanstar Communications, Inc.

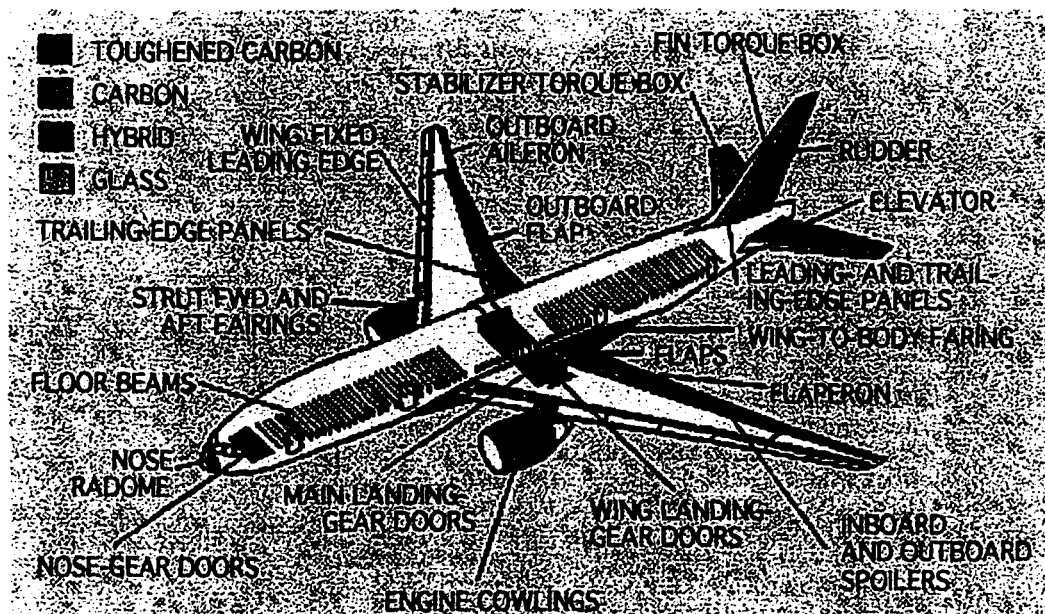


Figure 2.6 Composites use in the Boeing 777. Reproduced with permission from reference 3. Copyright by Advanstar Communications, Inc.

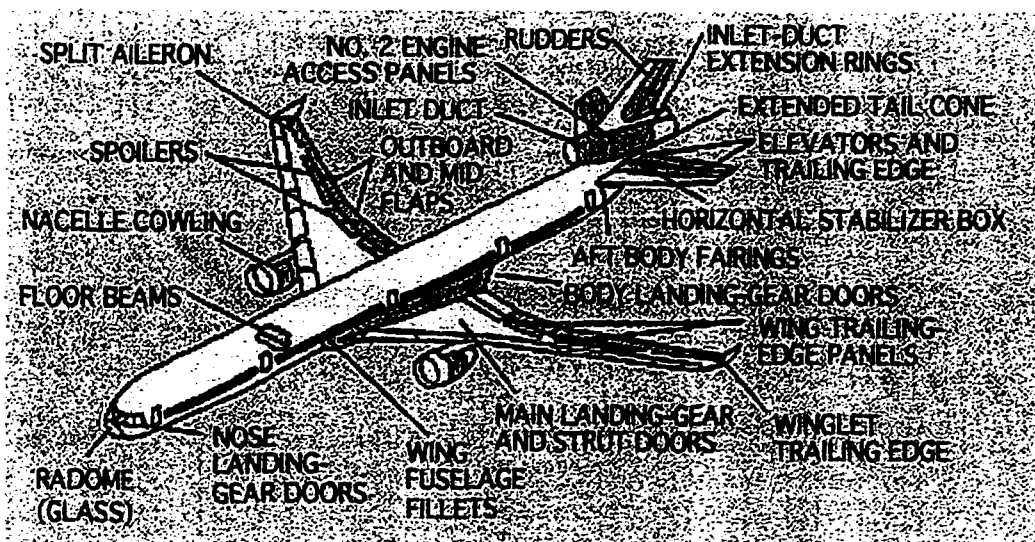


Figure 2.7 Composites use on the proposed Douglas MD-12X. Reproduced with permission from reference 3. Copyright by Advanstar Communications, Inc.

60,000 feet. To meet these requirements, the composites used in the construction of the aircraft must have several features. First, to carry this many passengers at speeds of Mach 2.4, the materials used in the construction of this aircraft must be lightweight. Second, to withstand the high speed and high altitude, the composite must be durable enough to endure these extreme conditions for many thousands of flight hours. For this type of flight profile, the skin of the airplane will reach temperatures of up to 350°F [50]. Finally, the materials used must be cost effective.

It is obvious that aircraft can be built which fly at these speeds. The Concorde flies at Mach 2.0 at an altitude of 55,000 feet [51], but the passenger capacity is limited to 100 people [51] and the price of a round-trip ticket from New York to London is in the neighborhood of \$7,500. Thus, designing a cost effective composite which meets the required specifications is an extremely challenging task.

2.4.3 Other Composite Applications

Besides being used as in primary and secondary structures of military as well as commercial aircraft, composites are finding other aerospace applications. Boron/epoxy composites are being used to repair cracks in B-1 bombers [4]. Traditional repair techniques, a bolted aluminum doubler and holes drilled at the ends of cracks, were found to be ineffective. The boron/epoxy prepreg used for the repair was laid on the surface of the airplane, heated, and cured under pressure to adhesively attach the material to the structure. This method provides several advantages over traditional bolted aluminum doubler techniques [4]. First, the aluminum doubler does not stop crack growth, and drilling and bolting increase stresses in the area around the crack. Second, the downtime for repairs is about $\frac{1}{10}$ as long because the use of a composite to effect the repair does not require disassembly of the structure. Finally, it has been shown that a boron/epoxy repair of cracking can increase the fatigue life of the aircraft by 25 times. With these obvious advantages, repairs are being made on the aircraft that exhibit cracking, and plans are underway to structurally reinforce the remaining fleet [4].

Although composites with polymer matrices are mainly used in aerospace structures, they are finding applications in a wide variety of other areas. The automobile industry is using composites to build cars that are over 31% lighter than the same car made of steel [44]. A concept vehicle called the XCAR has been fabricated with an all composite chassis and is estimated to get 90 miles per gallon, have an 80% reduction in emissions, and would be priced under \$15,000 [52]. Because of its composite structure, this automobile is also lightweight, noncorrosive, and its major components can

be recycled [52]. Medical applications of composites include artificial limbs [2] and bone plates to mend fractures [44]. Other applications involve bicycle frames [3] and reinforcement for concrete [44].

As can be seen, composites are being widely used in aerospace structures as well as a number of other applications. The advantages over metals are many, and as technology increases, the use of composite structures will continue to spread to more and more areas. Composites are becoming an integral part of our lives, whether it be travel, health, or recreation. Further understanding of these materials is, therefore, vital in determining the safety and reliability of such structures. To this end, this dissertation entails the use of ultrasonic measurement techniques to study damage in polymer matrix composites. With the development of damage assessment techniques, the safety of such structures can be assured.

Chapter 3

Acoustic Waves in Solids

Oscillations in elastic systems arise when particles are displaced from equilibrium. This deformation gives rise to restoring forces which act on the body to bring it back to its original state. As illustrated in Figure 3.1, an elastic solid can be approximated by a large number of particles connected together by massless springs [53].

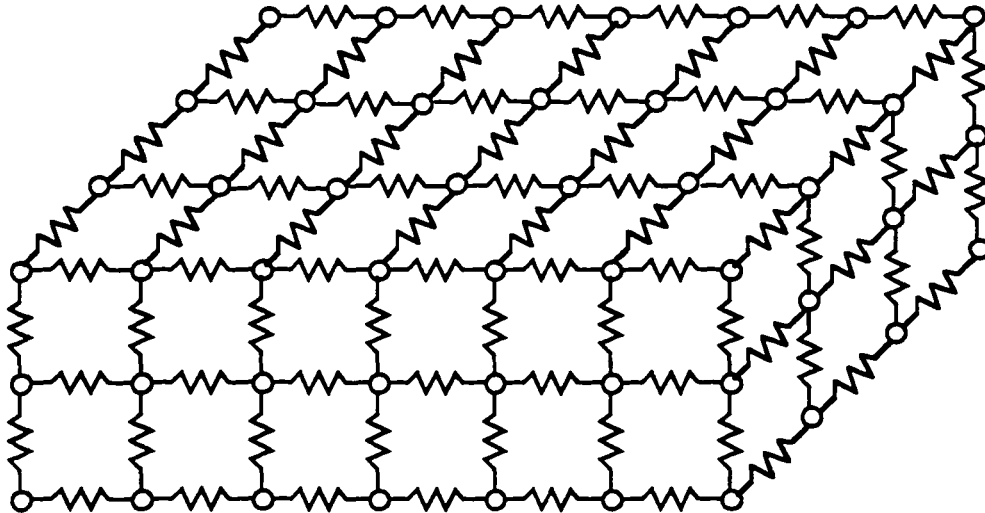


Figure 3.1 A three-dimensional spring model for an elastic solid.

A deformation in the system occurs when the particles are displaced with respect to one another. Because the particles are connected by springs, a displacement of one particle with respect to its neighbors will cause a displacement in the neighboring parti-

cles, which, in turn, displace their neighbors, and so on. The resulting particle motion is what is known as elastic wave propagation in solids.

It is important to note that elastic wave propagation is not dependent on the particle displacement, but on the deformation (particle displacement relative to the other particles). Rigid body motion such as translations or rotations displace particles from their original state, but there is no deformation and, hence, no wave propagation. This chapter develops the governing equations for acoustic wave propagation and examines the solution to guided waves in solids.

3.1 One-Dimensional Spring Model of a Continuous Material

For simplicity, a one-dimensional spring model for a continuous solid will be examined. Consider an infinite number of particles connected together by massless springs which have an equilibrium separation a . The system is now deformed such that the particles are at a distance α from their equilibrium position. This is shown schematically in Figure 3.2 [54].

Following the development of Goldstein [54], the Lagrangian for the system can be written in terms of the kinetic and potential energies of the system of particles. For the above case,

$$L = T - V = \frac{1}{2} \sum_i m \dot{\alpha}_i^2 - \frac{1}{2} \sum_i k (\alpha_{i+1} - \alpha_i)^2, \quad (3.1)$$

where T is the kinetic energy, V is the potential energy, m is the mass of the particle, a is the equilibrium separation, k is the spring constant, and the dot denotes differentiation with respect to time.

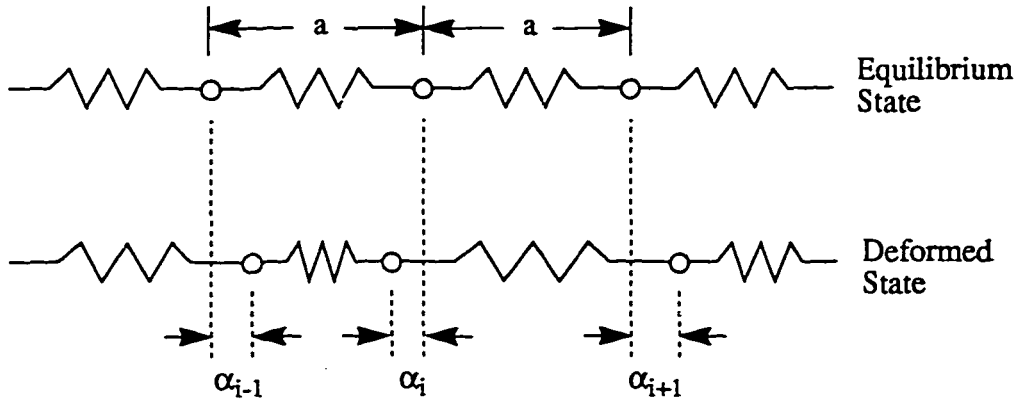


Figure 3.2 One-dimensional model of particles connected by massless springs to approximate an elastic solid (from reference 54).

tion with respect to time. Factoring out a , equation (3.1) can be expressed as [54]

$$L = \frac{1}{2} \sum_i a \left[\frac{m}{a} \dot{\alpha}_i^2 - ka \left(\frac{\alpha_{i+1} - \alpha_i}{a} \right)^2 \right] = \sum_i a L_i. \quad (3.2)$$

For a continuous system, the limit as $a \rightarrow 0$ is taken. In this limit, it can be seen in equation (3.2) that the term, $\frac{m}{a}$, just becomes the mass per unit length, μ . The behavior of the second term in L_i , in the limit, is not as simple to see. Examining Figure 3.2 and using Hooke's law, it can be seen that the force required to stretch a spring from its equilibrium length, a , is given by [54]

$$F = k(\alpha_{i+1} - \alpha_i) = ka \left(\frac{\alpha_{i+1} - \alpha_i}{a} \right). \quad (3.3)$$

The last term, $(\alpha_{i+1} - \alpha_i)/a$, is just the change in length per unit length. The force needed to deform a solid rod a given distance is [54]

$$F = E\xi, \quad (3.4)$$

where ξ is defined as the change in length per unit length and E is defined as Young's modulus. Relating equations (3.3) and (3.4), ka can be identified as Young's modulus of the elastic solid.

Next, it is noted that in the limit of a continuous system, α no longer represents a discrete point in space. Therefore, the variable i now becomes the coordinate x [54]. The change in length per unit length can now be written as

$$\frac{\alpha_{i+1} - \alpha_i}{a} \Rightarrow \frac{\alpha(x+a) - \alpha(x)}{a}. \quad (3.5)$$

In the limit as $a \rightarrow 0$, equation (3.5) is just defined as

$$\lim_{a \rightarrow 0} \left[\frac{\alpha(x+a) - \alpha(x)}{a} \right] \equiv \frac{d\alpha}{dx}. \quad (3.6)$$

Finally, in the continuous limit, the summation in equation (3.2) is converted to an integral, and the discrete length, a , is converted to the continuous term dx . This gives the Lagrangian of an elastic solid as [54]

$$L = \frac{1}{2} \int \left(\mu \dot{\alpha}^2 - E \left(\frac{d\alpha}{dx} \right)^2 \right) dx. \quad (3.7)$$

Lagrange's equation of motion in terms of the coordinate α is given by

$$\frac{\partial L}{\partial \alpha} - \frac{d}{dt} \left(\frac{\partial L}{\partial \dot{\alpha}} \right) - \frac{d}{dx} \left(\frac{\partial L}{\partial \alpha'} \right) = 0, \quad (3.8)$$

where the dot and prime denote differentiation with respect to t and x , respectively. For

the above Lagrangian, the equation of motion is given by [54]

$$\mu \frac{d^2 \alpha}{dt^2} - E \frac{d^2 \alpha}{dx^2} = 0, \quad (3.9)$$

which has a velocity of [54]

$$v = \sqrt{\frac{E}{\mu}}. \quad (3.10)$$

3.2 Definitions and the Development of Elastic Equations

The equation of motion and related velocity have been shown in the previous section for a one-dimensional continuous solid rod using Lagrangian mechanics. This section develops the definitions and equations governing particle displacement, deformation, strain, stress, and the elastic stiffness parameters.

3.2.1 Particle Displacement, Deformation, and Strain Defined

From the development of Auld [55], a relation can be derived for the differential particle displacement, which is a measure of particle deformation from its original state. Consider a particle whose location, L , is defined with respect to an arbitrary origin. Consider also a second particle in equilibrium with the first, which is at a location dL with respect to the first particle. The particles are then deformed. The first particle is moved u , defined as the particle displacement, from its original state, and its new location with respect to the origin is defined to be l . The second particle is now at a

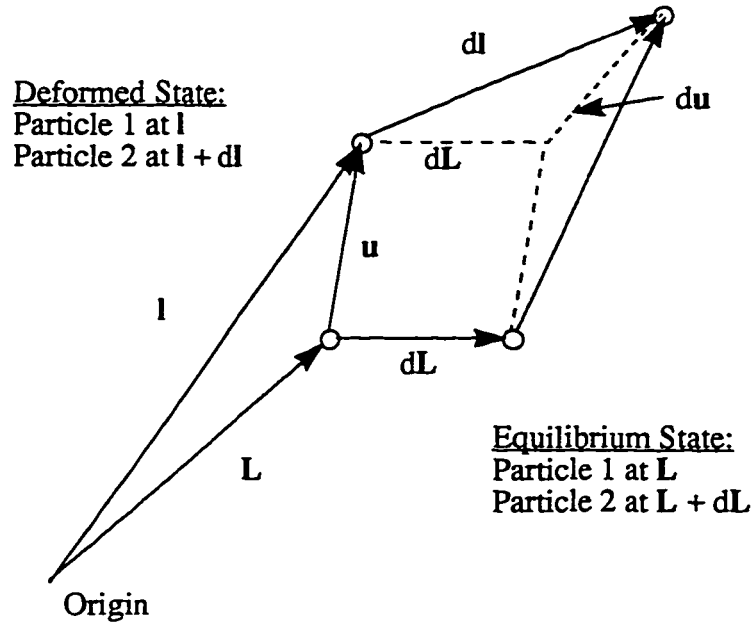


Figure 3.3 Differential particle displacement, du , defined for a solid in a deformed state (from reference 55).

location dl with respect to the first and has undergone a differential particle displacement, du . This is shown schematically, after Auld [55], in Figure 3.3.

Following the development of Auld [55], it can be seen from the figure that the differential particle displacement is [55]

$$du = dl - dL. \quad (3.11)$$

The differential particle displacement can be written in terms of partial derivatives as

$$du_i = \frac{\partial u_i}{\partial L_j} dL_j, \quad (3.12)$$

$$i, j = x, y, z,$$

where summation is assumed over repeated indices. In matrix form, this can be written as [55]

$$\begin{bmatrix} du_x \\ du_y \\ du_z \end{bmatrix} = \begin{bmatrix} \frac{\partial u_x}{\partial L_x} & \frac{\partial u_x}{\partial L_y} & \frac{\partial u_x}{\partial L_z} \\ \frac{\partial u_y}{\partial L_x} & \frac{\partial u_y}{\partial L_y} & \frac{\partial u_y}{\partial L_z} \\ \frac{\partial u_z}{\partial L_x} & \frac{\partial u_z}{\partial L_y} & \frac{\partial u_z}{\partial L_z} \end{bmatrix} \begin{bmatrix} dL_x \\ dL_y \\ dL_z \end{bmatrix}, \quad (3.13)$$

or, in a more compact notation,

$$[du] = [\varepsilon][dL], \quad (3.14)$$

where $[\varepsilon]$ is defined as the displacement gradient matrix.

To be a measure of deformation and not displacement, du must be equal to zero for any rigid body motion. The displacement gradient matrix reduces to zero for translations, but not for rotations. This is illustrated in Figure 3.4 for a rotation of a rigid body by an angle ϕ [55]. Since du is a vector quantity, it does not reduce to zero for a rigid body rotation. Note in the figure, however, that $|dL| = |dl|$. A scalar value which does reduce to zero for all rigid body motions is, thus [55],

$$\Delta = (dl)^2 - (dL)^2, \quad (3.15)$$

where the quantity, Δ , is defined as the deformation of a material. Alternately, this can be written as

$$\Delta = (dl_i)^2 - (dL_i)^2. \quad (3.16)$$

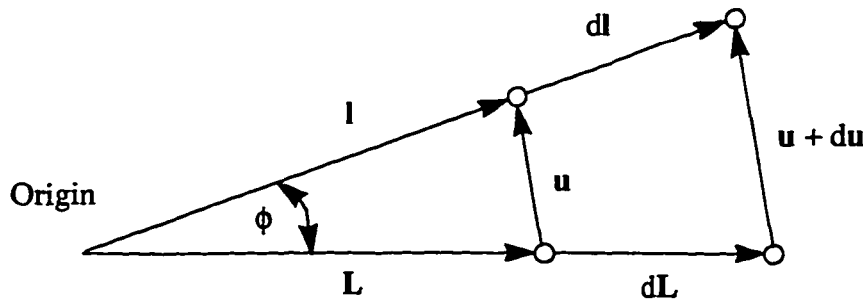


Figure 3.4 Rigid body rotation demonstrating that the vector quantity, du , does not reduce to zero for such cases (from reference 55).

Using equations (3.11) and (3.12), dl_i can be written as

$$dl_i = dL_i + \frac{\partial u_i}{\partial L_j} dL_j. \quad (3.17)$$

Substituting (3.17) into (3.16) yields

$$\Delta = \left(dL_i + \frac{\partial u_i}{\partial L_j} dL_j \right)^2 - (dL_i)^2. \quad (3.18)$$

Multiplying out gives

$$\Delta = \left(dL_i + \frac{\partial u_i}{\partial L_j} dL_j \right) \left(dL_i + \frac{\partial u_i}{\partial L_k} dL_k \right) - (dL_i)^2, \quad (3.19)$$

or,

$$\Delta = \frac{\partial u_i}{\partial L_k} dL_i dL_k + \frac{\partial u_i}{\partial L_j} dL_i dL_j + \frac{\partial u_i}{\partial L_j} \frac{\partial u_i}{\partial L_k} dL_j dL_k. \quad (3.20)$$

Since i, j , and k are just dummy indices, we can rewrite the first term in (3.20) by substituting j for i , and rewrite the second term by substituting k for i . Doing this leads to

$$\Delta = \left(\frac{\partial u_j}{\partial L_k} + \frac{\partial u_k}{\partial L_j} + \frac{\partial u_i}{\partial L_j} \frac{\partial u_i}{\partial L_k} \right) dL_j dL_k. \quad (3.21)$$

If small deformations are assumed so that the material is not permanently deformed or fractured, then the quadratic terms in (3.21) can be considered small compared to the remaining terms. This leaves

$$\Delta = \left(\frac{\partial u_j}{\partial L_k} + \frac{\partial u_k}{\partial L_j} \right) dL_j dL_k. \quad (3.22)$$

Equation (3.22) can be rewritten in the form [55]

$$\Delta = 2S_{jk} dL_j dL_k, \quad (3.23)$$

where [55]

$$S_{jk} = \frac{1}{2} \left(\frac{\partial u_j}{\partial L_k} + \frac{\partial u_k}{\partial L_j} \right), \quad (3.24)$$

$$j, k = x, y, z.$$

Here, S_{jk} is defined as the linearized strain-displacement relation, and its individual elements give the components of the strain on a material [55]. Another consequence of assuming small deformations is that the position vectors in the equilibrium and deformed states are approximately equal [55],

$$\mathbf{L} \equiv \mathbf{I} = \mathbf{r}. \quad (3.25)$$

Therefore, the strain-displacement relation can be written as [55]

$$S_{jk} = \frac{1}{2} \left(\frac{\partial u_j}{\partial r_k} + \frac{\partial u_k}{\partial r_j} \right), \quad (3.26)$$

$$j, k = x, y, z.$$

Equation (3.26) can be written in terms of symbolic notation of vectors and matrices as [55]

$$\mathbf{S} = \frac{1}{2} (\nabla \mathbf{u} + [\nabla \mathbf{u}]^T). \quad (3.27)$$

Defining [55]

$$\nabla_s \mathbf{u} = \frac{1}{2} (\nabla \mathbf{u} + [\nabla \mathbf{u}]^T), \quad (3.28)$$

the strain-displacement relation can now be written as [55]

$$\mathbf{S} = \nabla_s \mathbf{u}. \quad (3.29)$$

3.2.2 Abbreviated Subscript Notation

The strain matrix in (3.26) is symmetric and, thus, allows the equation to be simplified. It is noted from the symmetry that $S_{xy} = S_{yx}$, $S_{xz} = S_{zx}$, and $S_{yz} = S_{zy}$. This reduces the number of subscripts needed from nine to six. These are customarily defined as [55]

$$\mathbf{S} = \begin{bmatrix} S_{xx} & S_{xy} & S_{xz} \\ S_{xy} & S_{yy} & S_{yz} \\ S_{xz} & S_{yz} & S_{zz} \end{bmatrix} = \begin{bmatrix} S_1 & \frac{1}{2}S_6 & \frac{1}{2}S_5 \\ \frac{1}{2}S_6 & S_2 & \frac{1}{2}S_4 \\ \frac{1}{2}S_5 & \frac{1}{2}S_4 & S_3 \end{bmatrix}. \quad (3.30)$$

The factor of $\frac{1}{2}$ is introduced because it serves to simplify the strain-displacement equation, as well as equations which will be developed later. In terms of abbreviated subscripts, \mathbf{S} , \mathbf{u} , and ∇_s in (3.29) now take the form [55]

$$\mathbf{S} = \begin{bmatrix} S_1 \\ S_2 \\ S_3 \\ S_4 \\ S_5 \\ S_6 \end{bmatrix}, \quad \nabla_s = \begin{bmatrix} \frac{\partial}{\partial x} & 0 & 0 \\ 0 & \frac{\partial}{\partial y} & 0 \\ 0 & 0 & \frac{\partial}{\partial z} \\ 0 & \frac{\partial}{\partial z} & \frac{\partial}{\partial y} \\ \frac{\partial}{\partial z} & 0 & \frac{\partial}{\partial x} \\ \frac{\partial}{\partial y} & \frac{\partial}{\partial x} & 0 \end{bmatrix}, \quad \mathbf{u} = \begin{bmatrix} u_x \\ u_y \\ u_z \end{bmatrix}. \quad (3.31)$$

3.2.3 Stress

The previous section defined deformation and derived the strain-displacement equation in terms of abbreviated subscripts. As a material is deformed, restoring forces develop between the particles. This concept was shown schematically in Figure 3.1, where the restoring forces were modeled as massless springs which connected the particles. These restoring forces between the particles are defined as the stress.

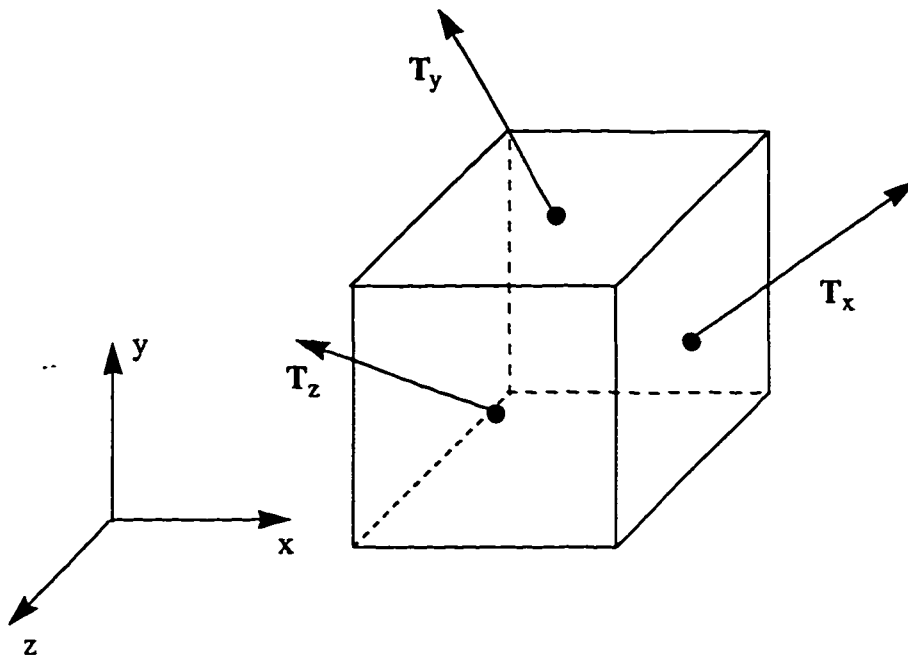


Figure 3.5 Traction forces, T_i , acting on each face of a volume element (from reference 55).

Consider a small volume element which has forces acting on the surface. These forces are known as traction forces and cause stresses to develop between the particles. This is illustrated in Figure 3.5 [55]. Since the traction forces are vector quantities, there exist three components to these forces on each surface. The forces can be written as

$$\mathbf{T}_j = T_{xj}\hat{\mathbf{x}} + T_{yj}\hat{\mathbf{y}} + T_{zj}\hat{\mathbf{z}}, \quad (3.32)$$

$$j = x, y, z.$$

The values T_{ij} represent the i^{th} component of stress on the j^{th} face and are known as the stresses.

The equation of motion can now be developed, after Auld [55], for a volume element subjected to surface and body forces. Consider a small element of a material with a surface area of δS and a volume of δV . The two forces acting on the volume element are the surface forces and a body force. These can be written as

$$\mathbf{F}_{\text{total}} = \mathbf{F}_{\text{surface}} + \mathbf{F}_{\text{body}}, \quad (3.33)$$

or,

$$\mathbf{F}_{\text{total}} = \int_{\delta S} \mathbf{T} \cdot \hat{\mathbf{n}} dS + \int_{\delta V} \mathbf{F} dV, \quad (3.34)$$

where \mathbf{T} represents the stresses, $\hat{\mathbf{n}}$ is a unit vector normal to the surface, and \mathbf{F} is the body force. Using Newton's Law, $\Sigma \mathbf{F} = m\mathbf{a}$, the above can be written as [55]

$$\int_{\delta S} \mathbf{T} \cdot \hat{\mathbf{n}} dS + \int_{\delta V} \mathbf{F} dV = \int_{\delta V} \rho \frac{\partial^2 \mathbf{u}}{\partial t^2} dV, \quad (3.35)$$

where ρ is the density and \mathbf{u} is the particle displacement. If the volume element is assumed to be infinitesimally small, the integrands can be considered constant and brought outside of the integral. Using this fact, equation (3.35) becomes [55]

$$\frac{\int_{\delta S} \mathbf{T} \cdot \hat{\mathbf{n}} dS}{\delta V} = \rho \frac{\partial^2 \mathbf{u}}{\partial t^2} - \mathbf{F}. \quad (3.36)$$

If the volume element is now taken in the limit to go to zero, the left-hand side of equation (3.36) is simply defined as the divergence. This leads to the translational equation of motion for the medium [55],

$$\nabla \cdot \mathbf{T} = \rho \frac{\partial^2 \mathbf{u}}{\partial t^2} - \mathbf{F}. \quad (3.37)$$

As was seen in equation (3.32),

$$\mathbf{T}_j = T_{ij} \hat{\mathbf{i}}, \quad (3.38)$$

$$i, j = x, y, z.$$

Recalling that the definition of divergence of a vector, \mathbf{A} , is

$$\nabla \cdot \mathbf{A} \equiv \frac{\partial A_x}{\partial x} + \frac{\partial A_y}{\partial y} + \frac{\partial A_z}{\partial z}, \quad (3.39)$$

and using (3.38), the divergence may be rewritten as [55]

$$\nabla \cdot \mathbf{T} = \frac{\partial T_j}{\partial r_j} = \frac{\partial T_{ij}}{\partial r_j} \hat{\mathbf{i}}. \quad (3.40)$$

Substituting this into equation (3.37) yields [55]

$$\frac{\partial T_{ij}}{\partial r_j} = \rho \frac{\partial^2 u_i}{\partial t^2} - F_i, \quad (3.41)$$

$$i, j = x, y, z.$$

As with strain, advantage of symmetry can be taken, and the stresses may be written in terms of abbreviated subscripts with the definition [55]

$$\mathbf{T} = \begin{bmatrix} T_{xx} & T_{xy} & T_{xz} \\ T_{xy} & T_{yy} & T_{yz} \\ T_{xz} & T_{yz} & T_{zz} \end{bmatrix} = \begin{bmatrix} T_1 & T_6 & T_5 \\ T_6 & T_2 & T_4 \\ T_5 & T_4 & T_3 \end{bmatrix}, \quad (3.42)$$

where the factor of $\frac{1}{2}$ introduced in the definition of strain is now omitted. Equation (3.37) now takes the form [55]

$$\nabla \cdot \mathbf{T} = \begin{bmatrix} \frac{\partial}{\partial x} & 0 & 0 & 0 & \frac{\partial}{\partial z} & \frac{\partial}{\partial y} \\ 0 & \frac{\partial}{\partial y} & 0 & \frac{\partial}{\partial z} & 0 & \frac{\partial}{\partial x} \\ 0 & 0 & \frac{\partial}{\partial z} & \frac{\partial}{\partial y} & \frac{\partial}{\partial x} & 0 \end{bmatrix} \begin{bmatrix} T_1 \\ T_2 \\ T_3 \\ T_4 \\ T_5 \\ T_6 \end{bmatrix} = \rho \frac{\partial^2 \mathbf{u}}{\partial t^2} - \mathbf{F}, \quad (3.43)$$

where

$$\mathbf{u} = \begin{bmatrix} u_x \\ u_y \\ u_z \end{bmatrix}, \quad \mathbf{F} = \begin{bmatrix} F_x \\ F_y \\ F_z \end{bmatrix}. \quad (3.44)$$

3.2.4 Elastic Constants and the Stress-Strain Relation

Section 3.2.1 defined deformation and developed a relationship between the strain and the particle displacement (3.29). In Section 3.2.3, the translational equation of motion, which relates the stress to the particle displacement and body forces, was developed (3.37). This section focuses on the relationship between stress and strain.

Stresses are restoring forces which arise when a particle is deformed from its

equilibrium position. Strain gives a measure of the material deformation. It was mentioned at the beginning of this chapter that a continuous material can be modeled as particles connected by massless springs. These springs are what provide the restoring forces between the particles. If a simple one-dimensional Hooke's Law model is examined, it is known that the restoring force is proportional to the displacement of the particle, i.e.

$$F_x = -k\Delta x, \quad (3.45)$$

where k is the spring constant, F is the restoring force, and Δx is the particle displacement from equilibrium. In the model of an elastic solid, stress is a restoring force per unit area, and the strain is related to the change in particle displacement, as was seen in equation (3.29). Therefore, stress takes the place of F , and strain assumes the role of Δx in equation (3.45). The "spring constants" which now relate the two values are defined as the elastic stiffness constants, which vary with direction and the type of material being considered. The relationship between stress and strain is written as [55]

$$T_{ij} = c_{ijkl} S_{kl}, \quad (3.46)$$

$$i, j, k, l = x, y, z,$$

where the stress and the elastic stiffness constants both have dimensions of force per unit area and the strain is dimensionless.

Recalling, though, from abbreviated subscript notation, Section 3.2.2, that

$$xx \rightarrow 1, yy \rightarrow 2, zz \rightarrow 3, yz \rightarrow 4, xz \rightarrow 5, xy \rightarrow 6,$$

where the numbers indicated the abbreviated subscripts, the stress-strain relation can now be written as [55]

$$T_I = c_{IJ} S_J, \quad (3.47)$$

$$I, J = 1, 2, 3, 4, 5, 6.$$

Equation (3.47) can be written in matrix notation as

$$[T] = [c][S], \quad (3.48)$$

where $[c]$ is a 6 by 6 matrix. The number of independent elastic stiffness constants for a material depends on the symmetry of the structure. The most general system (triclinic symmetry) has 21 independent elastic parameters. Isotropic systems have only two independent parameters and the matrix $[c]$ takes the form

$$[c] = \begin{bmatrix} c_{11} & c_{12} & c_{12} & 0 & 0 & 0 \\ c_{12} & c_{11} & c_{12} & 0 & 0 & 0 \\ c_{12} & c_{12} & c_{11} & 0 & 0 & 0 \\ 0 & 0 & 0 & c_{44} & 0 & 0 \\ 0 & 0 & 0 & 0 & c_{44} & 0 \\ 0 & 0 & 0 & 0 & 0 & c_{44} \end{bmatrix}, \quad (3.49)$$

where $c_{12} = c_{11} - 2c_{44}$. For the cases of interest here, a unidirectional composite has transversely isotropic symmetry, which has five associated elastic stiffness parameters, and a laminate with various fiber orientations has orthotropic symmetry, which has nine independent stiffness parameters.

The inverse of the elastic stiffness matrix relates the strain to the stress and is

known as the compliance of the material, s . Equation (3.47), written in terms of the compliance is [55]

$$S_I = s_{IJ} T_J, \quad (3.50)$$

where $I, J = 1, 2, 3, 4, 5$, and 6 . In matrix form, equation (3.50) can be written as

$$[S] = [s][T], \quad (3.51)$$

where

$$[s] = [c]^{-1}. \quad (3.52)$$

3.2.5 Bond Transformation Properties

Abbreviated subscripts provide a convenient notation for writing down the stresses, strains, and elastic stiffness components. However, the coordinate transformation properties, which redefine the elastic stiffness parameters for different directions of wave propagation, become a bit more difficult. It is, therefore, of interest to develop a procedure to transform components directly in terms of abbreviated subscripts.

Assume a rotation of an angle θ about an axis is desired. The transformation matrix for each axis is given by

$$\begin{aligned} a_{x\text{-axis}} &= \begin{bmatrix} 1 & 0 & 0 \\ 0 & \cos\theta & \sin\theta \\ 0 & -\sin\theta & \cos\theta \end{bmatrix}, & a_{z\text{-axis}} &= \begin{bmatrix} \cos\theta & \sin\theta & 0 \\ -\sin\theta & \cos\theta & 0 \\ 0 & 0 & 1 \end{bmatrix}, \\ a_{y\text{-axis}} &= \begin{bmatrix} \cos\theta & 0 & -\sin\theta \\ 0 & 1 & 0 \\ \sin\theta & 0 & \cos\theta \end{bmatrix}. \end{aligned} \quad (3.53)$$

In full subscript notation, where $[T]$ and $[S]$ are 3 by 3 matrices, the transformations for a matrix, $[B]$, are given by

$$[B'] = [a][B][a]^T, \quad (3.54)$$

or, equivalently,

$$B'_{ij} = a_{ik}a_{jl}B_{kl}, \quad (3.55)$$

$i, j, k, l = x, y, z.$

If each transformed term in full subscript notation is compared to its abbreviated subscript counterpart, the coordinate transformation of the stresses can be written in terms of abbreviated subscripts as [55]

$$T_H = M_{HI}T_I, \quad (3.56)$$

$H, I = 1, 2, 3, 4, 5, 6,$

where M_{HI} is a 6 by 6 transform defined by [55]

$$[M] = \begin{bmatrix} a_{xx}^2 & a_{xy}^2 & a_{xz}^2 & 2a_{xy}a_{xz} & 2a_{xz}a_{xx} & 2a_{xx}a_{xy} \\ a_{yx}^2 & a_{yy}^2 & a_{yz}^2 & 2a_{yy}a_{yz} & 2a_{yz}a_{yx} & 2a_{yx}a_{yy} \\ a_{zx}^2 & a_{zy}^2 & a_{zz}^2 & 2a_{zy}a_{zz} & 2a_{zz}a_{zx} & 2a_{zx}a_{zy} \\ (a_{yx}a_{zx})(a_{yy}a_{zy}) & (a_{yz}a_{zz})(a_{yy}a_{zz} + a_{yz}a_{zy}) & (a_{yx}a_{zz} + a_{yz}a_{zx})(a_{yy}a_{zx} + a_{yx}a_{zy}) & (a_{zx}a_{xx})(a_{zy}a_{xy}) & (a_{zz}a_{xz})(a_{xy}a_{zz} + a_{xz}a_{zy}) & (a_{xx}a_{zy} + a_{xy}a_{zx})(a_{xx}a_{yy} + a_{xy}a_{yz}) \\ (a_{zx}a_{xx})(a_{zy}a_{xy}) & (a_{zz}a_{xz})(a_{xy}a_{zz} + a_{xz}a_{zy}) & (a_{xz}a_{zx} + a_{xx}a_{zz})(a_{xx}a_{zy} + a_{xy}a_{zx}) & (a_{xx}a_{yz})(a_{xy}a_{yy}) & (a_{xz}a_{yz})(a_{xy}a_{yz} + a_{xz}a_{yy}) & (a_{xz}a_{yz} + a_{xx}a_{yz})(a_{xx}a_{yy} + a_{xy}a_{yz}) \end{bmatrix}. \quad (3.57)$$

Similarly, the transform of the stain is given by [55]

$$\begin{aligned} S'_K &= N_{KJ} S_J, \\ K, J &= 1, 2, 3, 4, 5, 6, \end{aligned} \quad (3.58)$$

where N_{KJ} is defined as [55]

$$[N] = \begin{bmatrix} a_{xx}^2 & a_{xy}^2 & a_{xz}^2 & a_{xy}a_{xz} & a_{xz}a_{xx} & a_{xx}a_{xy} \\ a_{yx}^2 & a_{yy}^2 & a_{yz}^2 & a_{yy}a_{yz} & a_{yz}a_{yx} & a_{yx}a_{yy} \\ a_{zx}^2 & a_{zy}^2 & a_{zz}^2 & a_{zy}a_{zz} & a_{zz}a_{zx} & a_{zx}a_{zy} \\ (2a_{yx}a_{zx}) & (2a_{yy}a_{zy}) & (2a_{yz}a_{zz}) & (a_{yy}a_{zz} + a_{yz}a_{zy}) & (a_{yx}a_{zz} + a_{yz}a_{zx}) & (a_{yy}a_{zx} + a_{yx}a_{zy}) \\ (2a_{zx}a_{xx}) & (2a_{zy}a_{xy}) & (2a_{zz}a_{xz}) & (a_{xy}a_{zz} + a_{xz}a_{zy}) & (a_{xz}a_{zx} + a_{xx}a_{zz}) & (a_{xx}a_{zy} + a_{xy}a_{zx}) \\ (2a_{xx}a_{yx}) & (2a_{xy}a_{yy}) & (2a_{xz}a_{yz}) & (a_{xy}a_{yz} + a_{xz}a_{yy}) & (a_{xz}a_{yz} + a_{xx}a_{yy}) & (a_{xx}a_{yy} + a_{xy}a_{yx}) \end{bmatrix}. \quad (3.59)$$

The transforms $[M]$ and $[N]$ are known as the Bond transforms, and the values of a_{ij} ($i, j = x, y, z$) are defined by the rotations given in equation (3.53). Recalling that

$$[T] = [c][S], \quad (3.60)$$

the transform of the stress can now be written as [55]

$$[T] = [M][c][S]. \quad (3.61)$$

The inverse of the strain transform is given by [55]

$$[S] = [N]^{-1}[S'], \quad (3.62)$$

which leads to the transformed stress being written as [55]

$$[T'] = [M][c][N]^{-1}[S']. \quad (3.63)$$

By comparing this result to equation (3.60), the transformed elastic stiffness matrix is given by [55]

$$[c'] = [M][c][N]^{-1}. \quad (3.64)$$

Similarly, the transformed compliances are given by [55]

$$[s'] = [N][s][M]^{-1}. \quad (3.65)$$

The above relation for the transformed elastic stiffness constants (3.64) will be used in subsequent numerical calculations for laminated composites.

3.2.6 One-Dimensional Example

For wave propagation in solids, there exist two types of waves: compressional and shear. Compressional (P) waves travel such that the particle displacements are parallel to the direction of propagation and shear waves have displacements which are perpendicular to the direction of propagation. Additionally, shear waves are classified into shear-horizontal (SH) waves, where the displacements are taken in the plane of the plate, and shear-vertical (SV) waves, where the displacements are perpendicular to the plane of the plate.

A simple one-dimensional example of a compressional wave is travelling along the x -axis is presented here. The displacement field can be written as

$$u = \hat{x} \cos(kx - \omega t). \quad (3.66)$$

The corresponding strain field is

$$S_{xx} = S_1 = \frac{\partial u_x}{\partial x} = -k \sin(kx - \omega t), \quad (3.67)$$

with all other strain components equal to zero. Substituting this into equation (3.48) gives the stresses as

$$\begin{aligned} T_1 &= c_{11}S_1 = -c_{11}k \sin(kx - \omega t), \\ T_2 &= c_{12}S_1 = -c_{12}k \sin(kx - \omega t), \\ T_3 &= c_{13}S_1 = -c_{13}k \sin(kx - \omega t). \end{aligned} \quad (3.68)$$

Since the strains and stresses only vary with the x -coordinate and the body forces, F_i , are taken to be zero, the equation of motion, (3.43), can be written as

$$\begin{aligned} \frac{\partial T_1}{\partial x} &= \rho \frac{\partial^2 u_x}{\partial t^2}, \\ \frac{\partial T_6}{\partial x} &= \rho \frac{\partial^2 u_y}{\partial t^2}, \\ \frac{\partial T_5}{\partial x} &= \rho \frac{\partial^2 u_z}{\partial t^2}. \end{aligned} \quad (3.69)$$

The only non-zero value surviving is the first term in the above equation. Using T_1 from equation (3.68) and u_x from equation (3.66) yields

$$c_{11}k^2 = \rho \omega^2. \quad (3.70)$$

The velocity of the wave is given by

$$v = \frac{\omega}{k} = \sqrt{\frac{c_{11}}{\rho}}. \quad (3.71)$$

The velocity in (3.71) is the same expression as was arrived at in equation (3.10) using a Lagrangian formulation for the one-dimensional spring model examined in Section 3.1. The only difference is that the linear mass density, μ , is replaced by the volume density, ρ , and Young's modulus, E , is replaced by the elastic stiffness parameter, c_{ll} . The appearance of these parameters is merely a result of moving from a one-dimensional solution to a three-dimensional solution.

3.3 Guided Waves

The previous section developed the necessary equations to describe acoustic wave propagation in solids. The core equations are the strain-displacement relation (3.29), the translational equation of motion (3.37), and the stress-strain relationship (3.48). This section will make use of these equations to solve for the propagation of guided acoustic waves in plates.

3.3.1 Development of Equations

Assume there exists a plate of thickness $2h$ in the x - y plane, in which a wave is propagating in the x -direction. This is shown schematically in Figure 3.6 [56]. As mentioned previously, both compressional (P) and shear waves (SV and SH) can propagate in the structure. In this case, the plate acts as an acoustic wave guide, similar to electromagnetic wave guides, by reflecting the propagating waves at the stress-free boundaries. Two classes of solutions exist for guided modes: shear-horizontal (SH)

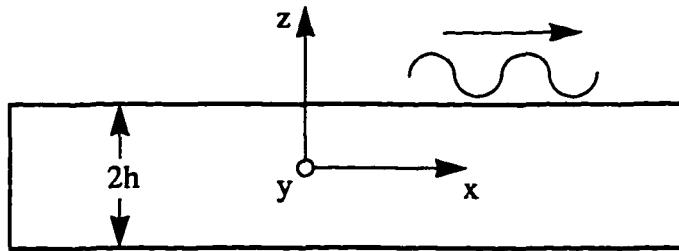


Figure 3.6 An acoustic wave travelling in a plate (from reference 56).

waves and Lamb waves. SH waves propagate in the x -direction and have displacements only in the y -direction. Lamb waves arise from a coupling at the free boundaries between the shear-vertical (SV) waves and the compressional (P) waves. For SH waves, the only non-zero displacement component is u_y . For Lamb waves, u_y is equal to zero. Only the solution for the Lamb waves will be treated here.

Assume a Lamb wave is travelling in an isotropic medium. For an isotropic case, there exist only two independent elastic stiffness parameters and the stiffness matrix is given by equation (3.49). Using Helmholtz's theorem, the displacement vector, \mathbf{u} , can be written in terms of a scalar and a vector potential as [56]

$$\mathbf{u} = \nabla\phi + \nabla \times \Psi, \quad (3.72)$$

where $\nabla\phi$ is defined as irrotational and $\nabla \times \Psi$ as solenoidal [57]. Since displacement in the y -direction must equal zero, the only non-zero component to the vector potential is Ψ_y . It is also noted that since the displacements do not vary in the y -direction, all derivatives with respect to y will also be equal to zero.

Using equation (3.72), the two non-zero components of displacement can be written as [56]

$$\begin{aligned} u_x &= \frac{\partial \phi}{\partial x} - \frac{\partial \psi}{\partial z}, \\ u_z &= \frac{\partial \phi}{\partial z} + \frac{\partial \psi}{\partial x}, \end{aligned} \quad (3.73)$$

where ψ is taken to be the component Ψ_y for ease of writing. The non-zero components of strain may now be written in terms of the potentials, using equation (3.29), as

$$\begin{aligned} S_1 &= \frac{\partial u_x}{\partial x} = \frac{\partial^2 \phi}{\partial x^2} - \frac{\partial^2 \psi}{\partial x \partial z}, \\ S_3 &= \frac{\partial u_z}{\partial z} = \frac{\partial^2 \phi}{\partial z^2} + \frac{\partial^2 \psi}{\partial x \partial z}, \\ S_5 &= \frac{\partial u_x}{\partial z} + \frac{\partial u_z}{\partial x} = -\frac{\partial^2 \psi}{\partial z^2} + \frac{\partial^2 \psi}{\partial x^2} + 2 \frac{\partial^2 \phi}{\partial x \partial z}. \end{aligned} \quad (3.74)$$

The stresses can be written in terms of the strains and elastic stiffness constants using (3.47) and (3.49) as

$$\begin{aligned} T_1 &= c_{11}S_1 + c_{12}S_3, \\ T_3 &= c_{12}S_1 + c_{11}S_3, \\ T_5 &= c_{44}S_5, \end{aligned} \quad (3.75)$$

where the remaining stresses are equal to zero. Plugging the stresses into the translational equation of motion (3.37), with the body forces set equal to zero, and using the relations (3.75) yields

$$\begin{aligned} \frac{\partial T_1}{\partial x} + \frac{\partial T_5}{\partial z} &= \frac{\partial}{\partial x}(c_{11}S_1 + c_{12}S_3) + \frac{\partial}{\partial z}(c_{44}S_5) = \rho \frac{\partial^2 u_x}{\partial t^2}, \\ \frac{\partial T_3}{\partial z} + \frac{\partial T_5}{\partial x} &= \frac{\partial}{\partial z}(c_{12}S_1 + c_{11}S_3) + \frac{\partial}{\partial x}(c_{44}S_5) = \rho \frac{\partial^2 u_z}{\partial t^2}. \end{aligned} \quad (3.76)$$

Using (3.73) and (3.74) to write the displacements and strains in terms of the potentials and collecting terms gives

$$\begin{aligned}\frac{\partial}{\partial x} \left(c_{11} \left(\frac{\partial^2 \phi}{\partial x^2} + \frac{\partial^2 \phi}{\partial z^2} \right) \right) + \frac{\partial}{\partial z} \left(-c_{44} \left(\frac{\partial^2 \psi}{\partial x^2} + \frac{\partial^2 \psi}{\partial z^2} \right) \right) &= \rho \left(\frac{\partial}{\partial x} \left(\frac{\partial^2 \phi}{\partial t^2} \right) - \frac{\partial}{\partial z} \left(\frac{\partial^2 \psi}{\partial t^2} \right) \right), \\ \frac{\partial}{\partial z} \left(c_{11} \left(\frac{\partial^2 \phi}{\partial x^2} + \frac{\partial^2 \phi}{\partial z^2} \right) \right) + \frac{\partial}{\partial x} \left(c_{44} \left(\frac{\partial^2 \psi}{\partial x^2} + \frac{\partial^2 \psi}{\partial z^2} \right) \right) &= \rho \left(\frac{\partial}{\partial z} \left(\frac{\partial^2 \phi}{\partial t^2} \right) + \frac{\partial}{\partial x} \left(\frac{\partial^2 \psi}{\partial t^2} \right) \right),\end{aligned}\quad (3.77)$$

where the relation $c_{12} = c_{11} - 2c_{44}$ has been used to eliminate c_{12} . The elastic constants are assumed to be constant and can, therefore, be brought outside the derivative. The above equations decouple in terms of ψ and ϕ , and the resulting equations of motion are

$$\begin{aligned}c_{11} \left(\frac{\partial^2 \phi}{\partial x^2} + \frac{\partial^2 \phi}{\partial z^2} \right) &= \rho \left(\frac{\partial^2 \phi}{\partial t^2} \right), \\ c_{44} \left(\frac{\partial^2 \psi}{\partial x^2} + \frac{\partial^2 \psi}{\partial z^2} \right) &= \rho \left(\frac{\partial^2 \psi}{\partial t^2} \right).\end{aligned}\quad (3.78)$$

If the fields are assumed to vary in time as $e^{-i\omega t}$, the above equation can be written as

$$\begin{aligned}c_{11} \left(\frac{\partial^2 \phi}{\partial x^2} + \frac{\partial^2 \phi}{\partial z^2} \right) &= -\rho \omega^2 \phi, \\ c_{44} \left(\frac{\partial^2 \psi}{\partial x^2} + \frac{\partial^2 \psi}{\partial z^2} \right) &= -\rho \omega^2 \psi,\end{aligned}\quad (3.79)$$

or, alternately, as [56]

$$\begin{aligned}\frac{\partial^2 \phi}{\partial x^2} + \frac{\partial^2 \phi}{\partial z^2} + k_l^2 \phi &= 0, \\ \frac{\partial^2 \psi}{\partial x^2} + \frac{\partial^2 \psi}{\partial z^2} + k_t^2 \psi &= 0.\end{aligned}\tag{3.80}$$

The values $k_l = \omega \sqrt{\frac{\rho}{c_{11}}}$ and $k_t = \omega \sqrt{\frac{\rho}{c_{44}}}$ are identified as the longitudinal and transverse wave numbers, respectively. It should be noted that the velocity associated with the scalar potential equation is the same as the velocity obtained for the compressional wave in equation (3.71). For an isotropic solid, it can be seen from equation (3.75) that c_{44} corresponds to the xz component of stress and strain. Thus, the transverse wave number, k_t , is identified with a z -polarized shear wave propagating in the x -direction. The scalar and vector potentials can, therefore, be identified as travelling compressional (P) and shear vertical (SV) waves, respectively. It is the coupling of these components at the free boundaries which gives rise to Lamb waves.

Following the development of Viktorov [56], the most general solution for a Lamb wave travelling in the x -direction which satisfies (3.80) is

$$\begin{aligned}\phi &= (A \cosh(qz) + B \sinh(qz))e^{i(kx - \omega t)}, \\ \psi &= (C \cosh(sz) + D \sinh(sz))e^{i(kx - \omega t)},\end{aligned}\tag{3.81}$$

where k and ω are the Lamb wave number and circular frequency, respectively. A , B , C , and D are constants; $q = \sqrt{k^2 - k_l^2}$ and $s = \sqrt{k^2 - k_t^2}$. Since the boundaries of the plate are free, the stress components $T_3 = T_{zz}$ and $T_5 = T_{xz}$ must disappear at $z = \pm h$. Using the relations in equations (3.74) and (3.75), the stresses may be written in terms of the scalar and vector potentials (3.81). Applying the boundary conditions at the surface of the plate shows that the equations which must be satisfied are [56]

$$\begin{aligned}
 (k^2 + s^2)A\cosh(qd) + (k^2 + s^2)B\sinh(qd) + 2iksC\sinh(sd) + 2iksD\cosh(sd) &= 0, \\
 (k^2 + s^2)A\cosh(qd) - (k^2 + s^2)B\sinh(qd) - 2iksC\sinh(sd) + 2iksD\cosh(sd) &= 0, \\
 2ikqA\sinh(qd) + 2ikqB\cosh(qd) - (k^2 + s^2)C\cosh(sd) - (k^2 + s^2)D\sinh(sd) &= 0, \\
 -2ikqA\sinh(qd) + 2ikqB\cosh(qd) - (k^2 + s^2)C\cosh(sd) + (k^2 + s^2)D\sinh(sd) &= 0.
 \end{aligned} \tag{3.82}$$

The first two equations in (3.82) are the results for T_3 going to zero at $+h$ and $-h$, respectively, and the last two results are for T_5 going to zero at $+h$ and $-h$, respectively. It can be seen from the symmetry that the set of equations (3.82) will be satisfied if [56]

$$\begin{aligned}
 [(k^2 + s^2)\cosh(qh)]A + [2iks\cosh(sh)]D &= 0, \\
 [2ikq\sinh(qh)]A - [(k^2 + s^2)\sinh(sh)]D &= 0,
 \end{aligned} \tag{3.83}$$

and

$$\begin{aligned}
 [(k^2 + s^2)\sinh(qh)]B + [2iks\sinh(sh)]C &= 0, \\
 [2ikq\cosh(qh)]B - [(k^2 + s^2)\cosh(sh)]C &= 0.
 \end{aligned} \tag{3.84}$$

For nontrivial solutions, the determinant of the above sets of equations must equal zero. The resulting relations which must be satisfied are [56]

$$(k^2 + s^2)^2\cosh(qh)\sinh(sh) - 4k^2sq\cosh(sh)\sinh(qh) = 0, \tag{3.85}$$

and

$$(k^2 + s^2)^2\sinh(qh)\cosh(sh) - 4k^2sq\sinh(sh)\cosh(qh) = 0. \tag{3.86}$$

Equations (3.85) and (3.86) define two separate dispersion relations that can be solved for the Lamb wave number, k , for a given frequency, ω , where the value of ω is related through the definitions of q and s . Equations (3.83) and (3.84) may now be used to express D and C in terms of A and B , respectively. Equation (3.81) now takes the form

$$\begin{aligned}\phi &= \phi_s + \phi_a, \\ \psi &= \psi_s + \psi_a,\end{aligned}\tag{3.87}$$

where

$$\begin{aligned}\phi_s &= A \cosh(q_s z) e^{i(k_s x - \omega t)}, \\ \phi_a &= B \sinh(q_a z) e^{i(k_a x - \omega t)}, \\ \psi_s &= \left(\frac{2ik_s q_s \sinh(q_s h)}{(k_s^2 + s_s^2) \sinh(s_s h)} \right) A \sinh(s_s z) e^{i(k_s x - \omega t)}, \\ \psi_a &= \left(\frac{2ik_a q_a \cosh(q_a h)}{(k_a^2 + s_a^2) \cosh(s_a h)} \right) B \cosh(s_a z) e^{i(k_a x - \omega t)}.\end{aligned}\tag{3.88}$$

The values of k_s and k_a are the values of k which satisfy the symmetric and antisymmetric dispersion relations (3.85) and (3.86), respectively; $q_{s,a} = \sqrt{k_{s,a}^2 - k_t^2}$ and $s_{s,a} = \sqrt{k_{s,a}^2 - k_t^2}$ [56]. In the above equation, the potentials are broken into a symmetric part (subscript s) and an antisymmetric part (subscript a), where the symmetry is defined with respect the z -mid-plane. The displacements can now be calculated from equation (3.73). The resulting equations are

$$\begin{aligned}u_x &= u_{x,s} + u_{x,a}, \\ u_z &= u_{z,s} + u_{z,a},\end{aligned}\tag{3.89}$$

where

$$\begin{aligned}u_{x,s} &= \frac{\partial \phi_s}{\partial x} - \frac{\partial \psi_s}{\partial z}, & u_{x,a} &= \frac{\partial \phi_a}{\partial x} - \frac{\partial \psi_a}{\partial z}, \\ u_{z,s} &= \frac{\partial \phi_s}{\partial z} + \frac{\partial \psi_s}{\partial x}, & u_{z,a} &= \frac{\partial \phi_a}{\partial z} + \frac{\partial \psi_a}{\partial x}.\end{aligned}\tag{3.90}$$

Substituting (3.88) into (3.90), the resulting displacements are

$$\begin{aligned} u_{x,s} &= k_s A \left(\cosh(q_s z) - \frac{2q_s s_s}{(k_s^2 + s_s^2)} \cdot \frac{\sinh(q_s h)}{\sinh(s_s h)} \cosh(s_s z) \right) e^{i(k_s x - \omega t + \frac{\pi}{2})}, \\ u_{z,s} &= q_s A \left(\sinh(q_s z) - \frac{2k_s^2}{(k_s^2 + s_s^2)} \cdot \frac{\sinh(q_s h)}{\sinh(s_s h)} \sinh(s_s z) \right) e^{i(k_s x - \omega t)}, \end{aligned} \quad (3.91)$$

and

$$\begin{aligned} u_{x,a} &= k_a B \left(\sinh(q_a z) - \frac{2q_a s_a}{(k_a^2 + s_a^2)} \cdot \frac{\cosh(q_a h)}{\cosh(s_a h)} \sinh(s_a z) \right) e^{i(k_a x - \omega t + \frac{\pi}{2})}, \\ u_{z,a} &= q_a B \left(\cosh(q_a z) - \frac{2k_a^2}{(k_a^2 + s_a^2)} \cdot \frac{\cosh(q_a h)}{\cosh(s_a h)} \cosh(s_a z) \right) e^{i(k_a x - \omega t)}. \end{aligned} \quad (3.92)$$

The displacement field (3.91) defines a class of P and SV waves travelling with the same wavenumber, k_s , and the same circular frequency, ω . The displacements are, therefore, coupled together and the wavenumber, k_s , is just the solution to the eigen-value dispersion relation (3.85). It is also seen that the displacements are symmetric with respect to the z-mid-plane. Similarly, the displacement field (3.92) defines coupled P and SV waves travelling with a wavenumber, k_a , and a circular frequency, ω . The displacement field is antisymmetric with respect to the z-mid-plane, and the values of k_a are the eigenvalue solutions to the dispersion relation (3.86).

The two classes of solutions described above define propagating modes known as Lamb waves. Those which satisfy the displacement relations (3.91) and dispersion equation (3.85) are known as the symmetric, or dilational, waves. Those which satisfy (3.92) and (3.86) are known as antisymmetric, or flexural, waves. A diagram of the particle displacements for the two lowest order modes is shown in Figure 3.7. The particle

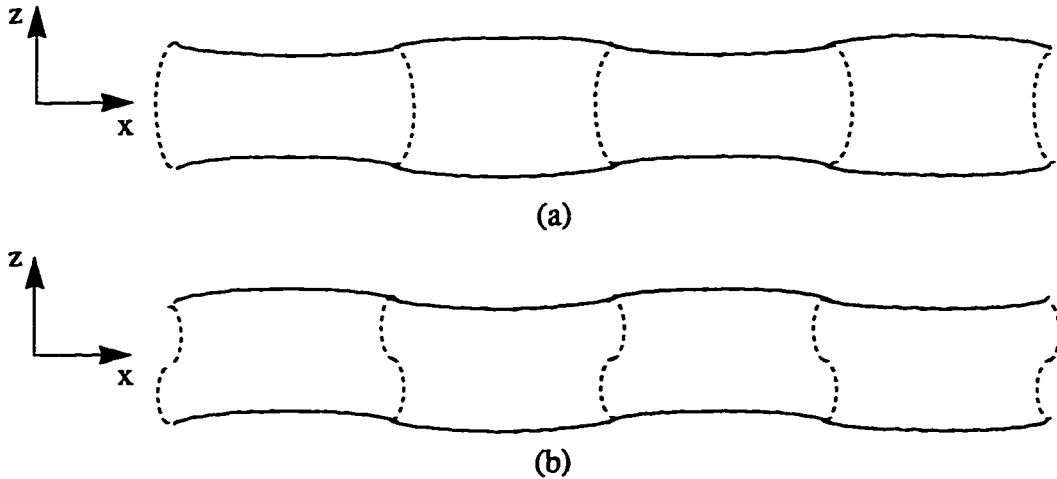


Figure 3.7 Two classes of Lamb waves: (a) symmetric and (b) antisymmetric. The solid lines indicate the displacement field in the z -direction and the dotted lines indicate the displacement field in the x -direction.

displacements for the higher order modes are more complex, but the symmetry with respect to the mid-plane is the same.

The dispersion relations, (3.85) and (3.86), show that the solutions for the wave-number, k , depend on the circular frequency, ω , the density, ρ , the thickness of the plate, $2h$, and the elastic stiffness constants of the material, c_{IJ} . The solutions also involve harmonic functions, which means that an infinite number of modes can exist. In addition, the velocity dependence on the frequency shows that the modes are dispersive. A dispersion curves for an isotropic material is shown in Figure 3.8. The total thickness of the plate, $d = 2h$, was taken to be 0.1 cm in the calculation and the material properties for aluminum were used and have the values [55]

$$c_{11} = 111 \times 10^9 \frac{\text{N}}{\text{m}^2}, \quad c_{44} = 25 \times 10^9 \frac{\text{N}}{\text{m}^2}, \quad (3.93)$$

$$\rho = 2695 \frac{\text{kg}}{\text{m}^3}.$$

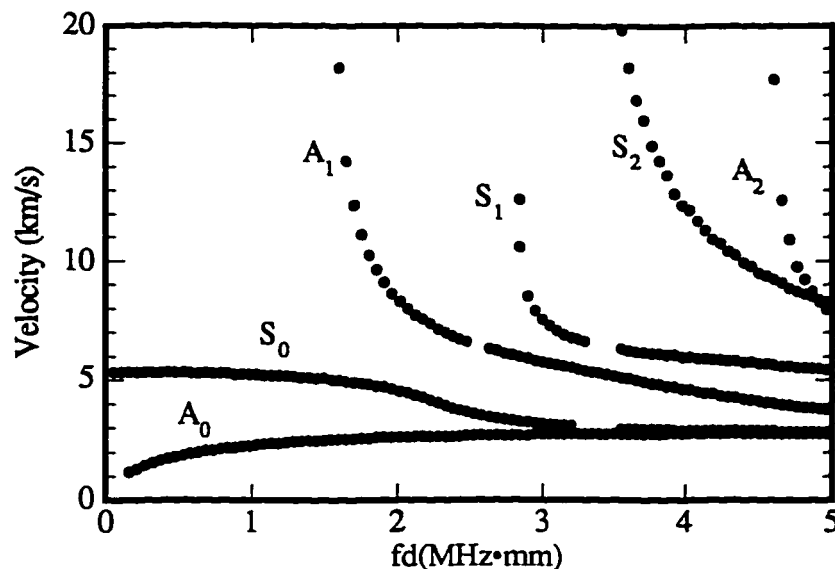


Figure 3.8 Dispersion curves for aluminum showing the first few symmetric (S_i) and antisymmetric (A_i) modes.

There are several interesting features seen in the behavior of the dispersion curves. First, the velocity is plotted against the frequency-thickness product, fd . This serves to normalize the curves so that they can be used for any thickness of a given material. Second, the velocity of each curve depends on the frequency of propagation. Thus, the modes are dispersive. Third, as fd increases, additional modes begin to propagate. Therefore, there are an unlimited number of modes that can exist. Fourth, the higher order modes (A_i and S_i for $i \geq 1$) have a particular fd product where they begin to propagate. At this point, the phase velocity $\rightarrow \infty$, and below this value, the modes do not propagate. Hence, there exists a cutoff frequency for these modes. Fifth, at large fd products, i.e. thick plates, the velocity approaches the Rayleigh (surface) wave solution. Finally, the two lowest order modes (A_0 and S_0) are the only ones which

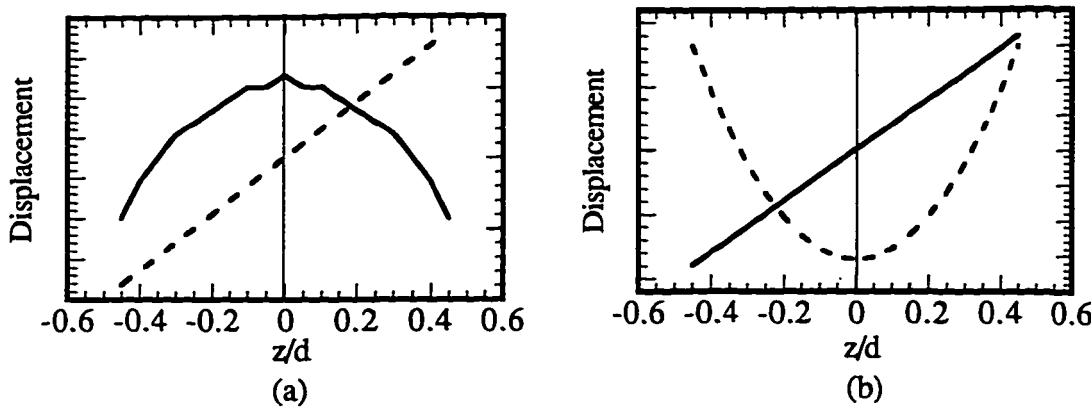


Figure 3.9 Particle displacements u_x (solid) and u_z (dashed) showing the symmetry of the first two Lamb modes in aluminum: (a) S_0 and (b) A_0 .

exist for all frequencies, and their behavior is much different than that of the higher modes. The unique properties of these two modes are examined more fully in the next section.

The symmetry of the various modes can be identified by examining the displacements through the thickness of the material. To demonstrate this symmetry, the displacements through the thickness of the plate, as calculated from equations (3.91) and (3.92), are plotted in Figure 3.9 for the first two Lamb modes. The values were calculated for an fd product of 0.02 MHz•mm.

3.3.2 Low Frequency Limit

In the low frequency-thickness limit, $fd < 1.5$ for aluminum, only the two lowest order modes propagate, one symmetric and one antisymmetric. The A_0 mode is highly dispersive in this region, and the S_0 mode is approximately nondispersive. Another interesting feature of these modes involves the particle displacements. If fd is assumed

to be very small, the particle displacements in equations (3.91) and (3.92) can be approximated. In this limit, the hyperbolic functions can be replaced by their small-argument approximation. With this substitution, the ratio of the displacements for each mode is given by

$$S_0 \Rightarrow \frac{u_{z,s}}{u_{x,s}} \approx \alpha fz, \quad A_0 \Rightarrow \frac{u_{x,a}}{u_{z,a}} \approx \beta fz. \quad (3.94)$$

The values of the constants in the above equation are

$$\alpha = \frac{\left(1 - \left(\frac{v_s}{v_l}\right)^2\right)}{v_s \left(1 - 2 \frac{c_{44}}{c_{11}}\right)}, \quad \beta = \frac{-2\pi}{v_a}, \quad (3.95)$$

where v_l is the longitudinal wave velocity, c_{11} and c_{44} are the elastic stiffness parameters, and v_s and v_a are the symmetric and antisymmetric Lamb wave velocities, respectively.

In the limit of fz being small, since $z \leq d$, it can be seen from (3.94) that the S_0 mode is dominated by the in-plane displacements, u_x , and the A_0 mode is dominated by out-of-plane displacements, u_z . At the mid-plane of the plate ($z = 0$), equations (3.91) and (3.92) show that the displacements $u_{z,s} = 0$ and $u_{x,a} = 0$. Thus, at this point, there are only in plane displacements for the symmetric mode and out of plane displacements for the antisymmetric mode. The ratios of the displacements, as approximated in equation (3.94), as well as the exact values given by equations (3.91) and (3.92), are plotted as a function of z in Figure 3.10 for an fd product of 0.02 MHz•mm.

There are several interesting features to note from the figure. First, comparison

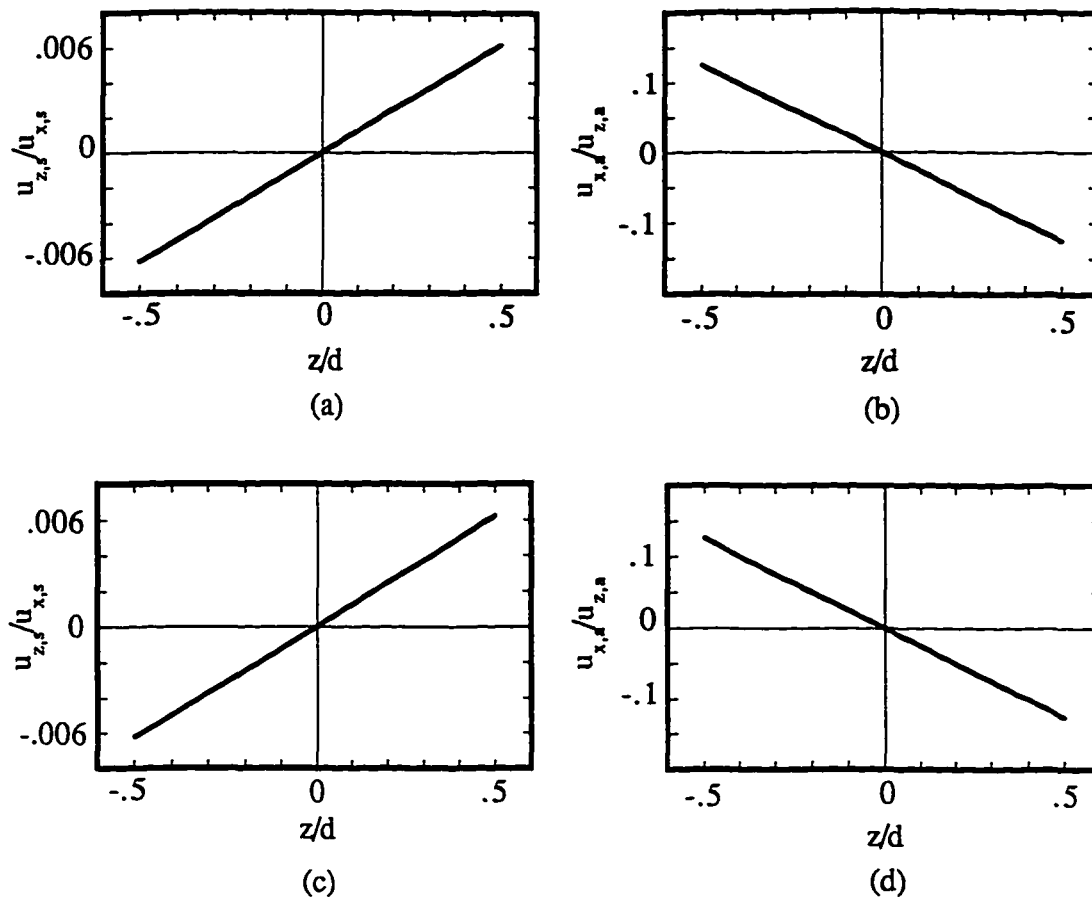


Figure 3.10 Plot of the ratio of the displacements as approximated in equation (3.94) versus exact values given by equations (3.91) and (3.92) for an fd product of 0.02 MHz•mm: (a) approximate u_z/u_x for S_0 , (b) approximate u_x/u_z for A_0 , (c) exact u_z/u_x for S_0 , and (d) exact u_x/u_z for A_0 .

of the exact solution with the approximate solution found in equation (3.94) shows that the results are identical for a small fd product. Second, the S_0 mode is highly dominated by the in-plane displacement, u_x . Finally, the A_0 mode is dominated by the out-of-plane displacements, u_z , but to a lesser degree than the in-plane dominance exhibited by the S_0 mode.

As mentioned earlier, the velocity of each Lamb mode depends on the properties of the material. This is the reason they are very useful in characterizing material prop-

erties. The lower mode behavior, detailed above, is important in this characterization process. First, only two modes propagate in the low frequency limit. Thus, the signals are not confused with four or five modes overlapping one another. Second, the velocity of the S_0 mode is greater than the A_0 mode. Hence, the modes separate after only a short distance of propagation and are easy to detect from each other. Since S_0 velocity is greater than the A_0 velocity and these are the only modes propagating, the S_0 mode can be identified as the first signal to arrive. Third, the S_0 mode is not very dispersive in this region. Therefore, the frequency at which the velocity is measured is not as critical to the result. This is an extremely important point when evaluating damage in materials because the damage incurred often causes scattering and attenuation of the higher frequency components. Finally, because the mode propagates at long wavelengths, local defects (which tend to scatter higher frequency waves) will not be observed and information about the effective elastic properties of a material can be obtained. Therefore, the measurements in this study concentrate on examining this mode.

As shown in Equations (3.85) and (3.86), analytical solutions to dispersion relations for an isotropic material are available due to the fact that isotropic solids have only two independent elastic stiffness parameters. Composites, which are anisotropic and inhomogeneous by nature, have five independent constants for a single unidirectional layer. When these layers are stacked at various orientations with respect to one another to form a laminate, the difficulty of the problem increases. Therefore, numerical techniques must be employed to solve for the dispersion relations for these complex architectures. The next chapter details the generation of theoretical dispersion curves for multidirectional composite structures.

Chapter 4

Numerical Modeling

Several theories exist which predict dispersion curves for laminated composites plates. Prosser [58] used laminated plate theory to obtain dispersion curves for composite plates and compared the solutions to experimental results for a variety of samples. The data and theory were seen to compare quite well. Presented in this study is a through-the-thickness finite element method. The Lagrangian for the composite plate is expressed in terms of nodal displacements and then minimized to obtain an eigenvalue problem which solves for the dispersion curves of the laminate.

4.1 Finite Element Model

A theoretical model, detailed in Dong and Huang [59] and Datta, et al. [60], for generating dispersion curves in laminated composites will be examined. Following the development of Datta, et al. [60], the composite sample is divided into finite element layers, each of thickness h . The z -axis is taken to be perpendicular to the layer and the x -axis is taken to be along the direction of wave propagation. This is shown schematically in Figure 4.1.

Two types of solutions exist for wave propagation in the solid: one in which the

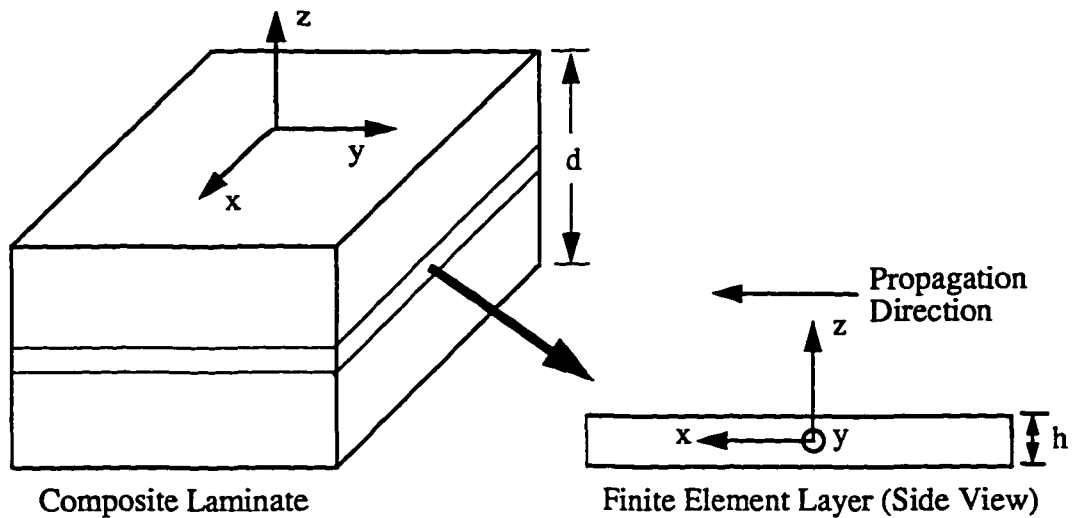


Figure 4.1 Finite element layer for a composite laminate.

displacements are non-zero in x - and z -directions and one in which the only non-zero displacement is in the y -direction. The former, which combines compressional (P) and shear vertical (SV) waves, is the previously mentioned Lamb wave solution. The latter, which only has displacements in the y -direction, identifies a class of solutions known as shear horizontal (SH) waves. Since Lamb wave propagation is of interest, the SH case will not be treated here.

Each individual unidirectional lamina in the composite can be modeled as a transversely isotropic layer, where the plane of isotropy is taken to be a plane perpendicular to the fiber direction. If the x -axis is taken as the fiber direction, then the y - z plane is considered as the plane of isotropy. Due to the symmetry, the y and z subscripts can be interchanged, which reduces the number of elastic stiffness constants required to just five. Recalling from abbreviated subscripts that

$$xx \rightarrow 1, yy \rightarrow 2, zz \rightarrow 3, yz \rightarrow 4, xz \rightarrow 5, xy \rightarrow 6,$$

one can see that the abbreviated subscripts 2 and 3, as well as 5 and 6, are interchangeable for a transversely isotropic. This leaves the relations

$$\begin{aligned} c_{22} &= c_{33}, \\ c_{12} &= c_{13}, \\ c_{55} &= c_{66}. \end{aligned} \quad (4.1)$$

Additionally, the elastic stiffness constant c_{44} is not independent and is shown to be [2]

$$c_{44} = \frac{c_{22} - c_{23}}{2}. \quad (4.2)$$

If each sublayer is assumed to be transversely isotropic, the stress-strain relation (3.48) is given by

$$[T] = [c][S], \quad (4.3)$$

where $[T]$, $[S]$, and $[c]$ now take the form

$$\begin{aligned} [T]^T &= [T_1, T_3, T_5], \\ [S]^T &= [S_1, S_3, S_5], \\ [c] &= \begin{bmatrix} c_{11} & c_{13} & 0 \\ c_{13} & c_{33} & 0 \\ 0 & 0 & c_{55} \end{bmatrix}. \end{aligned} \quad (4.4)$$

The 2, 4, and 6 components of strain vanish due to the fact that SH waves (displacements in the y-direction) are not being considered. Equation (4.3) is the governing equation for each sublayer. If a lamina is oriented such that the fibers are not aligned along the propagation direction, then the elastic stiffness constants for a sublayer in the

lamina can be obtained by using the Bond transformation (3.64) for a rotation about the z -axis. The transformed stiffness constants for a lamina making an angle θ with respect to the propagation direction are given by

$$\begin{aligned} c_{11}' &= a^2(c_{11}a^2 + c_{13}b^2) + b^2(c_{13}a^2 + c_{33}b^2) + 2c_{55}a^2b^2, \\ c_{13}' &= c_{13}a^2 + c_{23}b^2, \\ c_{33}' &= c_{33}, \\ c_{23}' &= c_{23}a^2 + c_{13}b^2, \\ c_{55}' &= c_{55}a^2 + \frac{(c_{33} - c_{23})}{2}b^2, \end{aligned} \quad (4.5)$$

where $a \equiv \cos \theta$ and $b \equiv \sin \theta$. From the above equation, it can be seen that all five stiffness constants are needed to calculate the transformed c_{ij} 's for laminas making an arbitrary angle with respect to the propagation direction. Note, however, from equation (4.4), that only four elastic stiffness parameters are needed for a unidirectional composite. The relationship between the four customarily defined engineering parameters and the five elastic stiffness constants is detailed in Appendix A and further discussion will be presented in subsequent sections.

Now that the elastic stiffness parameters in each layer are known, the displacements through the thickness of each sublayer are expressed in terms of nodal displacements at the back, middle, and front. This is shown schematically in Figure 4.2. The displacements may now be approximated using quadratic interpolation functions through the thickness as

$$\begin{aligned} u_x(z) &= az^2 + bz + c, \\ u_z(z) &= dz^2 + ez + f. \end{aligned} \quad (4.6)$$

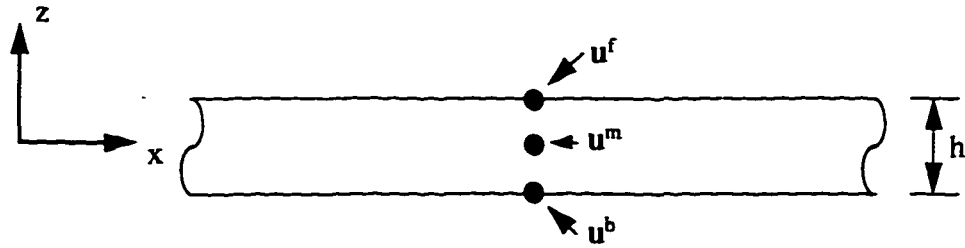


Figure 4.2 Nodal displacements at the back, middle, and front of a finite element layer.

Substituting the definitions of the nodal displacements,

$$\begin{aligned}
 u_x^b &= u_x\left(-\frac{h}{2}\right), & u_z^b &= u_z\left(-\frac{h}{2}\right), \\
 u_x^m &= u_x(0), & u_z^m &= u_z(0), \\
 u_x^f &= u_x\left(\frac{h}{2}\right), & u_z^f &= u_z\left(\frac{h}{2}\right),
 \end{aligned} \tag{4.7}$$

and solving for $a-f$, the displacements can be expressed as

$$\begin{aligned}
 u_x(z) &= n_1 u_x^b + n_2 u_x^m + n_3 u_x^f, \\
 u_z(z) &= n_1 u_z^b + n_2 u_z^m + n_3 u_z^f,
 \end{aligned} \tag{4.8}$$

where

$$\begin{aligned}
 n_1 &= -\frac{z}{h} + 2\frac{z^2}{h^2}, \\
 n_2 &= 1 - 4\frac{z^2}{h^2}, \\
 n_3 &= \frac{z}{h} + 2\frac{z^2}{h^2}.
 \end{aligned} \tag{4.9}$$

In the above, h is the thickness of the layer and $u_x^b, u_z^b, u_x^m, u_z^m, u_x^f$, and u_z^f are the x and z nodal displacements at the back, middle, and front of each finite element layer. Equation (4.8) may be written in a more compact form as [60]

$$[u] = [n][q], \quad (4.10)$$

where

$$\begin{aligned} [u]^T &= [u_x, u_z], \\ [n] &= \begin{bmatrix} n_1 & 0 & n_2 & 0 & n_3 & 0 \\ 0 & n_1 & 0 & n_2 & 0 & n_3 \end{bmatrix}, \\ [q]^T &= [u_x^b, u_z^b, u_x^m, u_z^m, u_x^f, u_z^f]. \end{aligned} \quad (4.11)$$

Using expressions for the kinetic and strain (potential) energies [55], the Lagrangian for each layer can be written as

$$L = \frac{1}{2} \int \int \rho [\dot{u}]^T [\dot{u}] dz dx - \frac{1}{2} \int \int [S]^T [c] [S] dz dx, \quad (4.12)$$

where $[u]$ is defined in equation (4.11), $[S]$ and $[c]$ are defined by (4.4), and dots denote differentiation with respect to time. Using equation (4.10) for the particle displacements and integrating in the z -direction, the first term (kinetic energy) in equation (4.12) can be written in terms of the generalized nodal displacements as

$$L_k = \frac{1}{2} \int [\dot{q}]^T [m] [\dot{q}] dx, \quad (4.13)$$

where

$$[m] = \int_{-\frac{h}{2}}^{\frac{h}{2}} \rho [n]^T [n] dz. \quad (4.14)$$

Writing the strain (potential) energy in equation (4.12) in terms of the generalized nodal displacements, $[q]$, is not as easily done. First, using the strain-displacement equation, (3.29), and the definitions (3.31), the strain can be written as

$$[S] = \begin{bmatrix} \frac{\partial}{\partial x} & 0 \\ 0 & \frac{\partial}{\partial z} \\ \frac{\partial}{\partial z} & \frac{\partial}{\partial x} \end{bmatrix} \begin{bmatrix} u_x \\ u_z \end{bmatrix}. \quad (4.15)$$

Substituting for $[u]$ using (4.10) yields

$$[S] = \begin{bmatrix} \frac{\partial}{\partial x} & 0 \\ 0 & \frac{\partial}{\partial z} \\ \frac{\partial}{\partial z} & \frac{\partial}{\partial x} \end{bmatrix} \begin{bmatrix} n_1 & 0 & n_2 & 0 & n_3 & 0 \\ 0 & n_1 & 0 & n_2 & 0 & n_3 \end{bmatrix} [q]. \quad (4.16)$$

Multiplying out gives

$$[S] = [A_1][q'] + [A_2][q], \quad (4.17)$$

where $[A_1]$ and $[A_2]$ are defined as

$$[A_1] = \begin{bmatrix} n_1 & 0 & n_2 & 0 & n_3 & 0 \\ 0 & 0 & 0 & 0 & 0 & 0 \\ 0 & n_1 & 0 & n_2 & 0 & n_3 \end{bmatrix}, \quad [A_2] = \begin{bmatrix} 0 & 0 & 0 & 0 & 0 & 0 \\ 0 & \frac{\partial n_1}{\partial z} & 0 & \frac{\partial n_2}{\partial z} & 0 & \frac{\partial n_3}{\partial z} \\ \frac{\partial n_1}{\partial z} & 0 & \frac{\partial n_2}{\partial z} & 0 & \frac{\partial n_3}{\partial z} & 0 \end{bmatrix}, \quad (4.18)$$

and prime denotes differentiation with respect to x . By substituting (4.17) into (4.12) and integrating in the z -direction, the strain energy in the Lagrangian can be written in terms of the generalized nodal displacements as

$$L_s = \frac{1}{2} \int ([q']^T [k_1] [q'] + [q']^T [k_2] [q] + [q]^T [k_2]^T [q'] + [q]^T [k_3] [q]) dx, \quad (4.19)$$

where $[k_1]$, $[k_2]$, and $[k_3]$ are defined as

$$\begin{aligned} [k_1] &= \int_{-\frac{h}{2}}^{\frac{h}{2}} [A_1]^T [c] [A_1] dz, & [k_2] &= \int_{-\frac{h}{2}}^{\frac{h}{2}} [A_1]^T [c] [A_2] dz, \\ [k_3] &= \int_{-\frac{h}{2}}^{\frac{h}{2}} [A_2]^T [c] [A_2] dz. \end{aligned} \quad (4.20)$$

Combining equations (4.13) and (4.19), the Lagrangian for a single finite element layer (4.12) may now be written in terms of the generalized displacements as

$$\begin{aligned} L &= \frac{1}{2} \int [q]^T [m] [q] - [q']^T [k_1] [q'] - [q']^T [k_2] [q] \\ &\quad - [q]^T [k_2]^T [q'] - [q]^T [k_3] [q] dx, \end{aligned} \quad (4.21)$$

where $[m]$ and $[k_i]$ ($i = 1, 2$, and 3) are 6 by 6 matrices defined by (4.14) and (4.20), respectively.

The next step is to add the individual Lagrangians for each layer to construct the Lagrangian for the entire plate. This is done by matching the displacements at the interfaces. The procedure for adding two layers is shown schematically in Figure 4.3. For n layers, the generalized displacements for the added layers, $[Q]$, will be of length $(4n+2)$ and the final matrices $[M]$, $[K_1]$, $[K_2]$, and $[K_3]$ will be of dimension $(4n+2)$ by $(4n+2)$. Once the layers are added together, the Lagrangian for the entire plate is given by

$$\begin{aligned} L = & \frac{1}{2} \int [\dot{Q}]^T [M] [\dot{Q}] - [Q']^T [K_1] [Q'] - [Q']^T [K_2] [Q] \\ & - [Q]^T [K_2]^T [Q'] - [Q]^T [K_3] [Q] dx. \end{aligned} \quad (4.22)$$

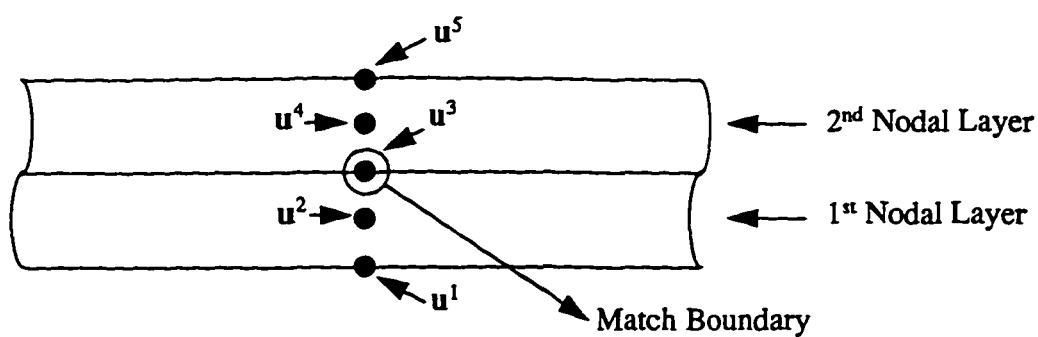
Taking the variation of L and setting it equal to zero, Hamilton's Principle, yields the governing equation for the plate [60]:

$$[K_1][Q'''] + [K_2^*][Q'] - [K_3][Q] - [M][\ddot{Q}] = 0, \quad (4.23)$$

where

$$[K_2^*] = [K_2] - [K_2]^T. \quad (4.24)$$

In equation (4.23), $[Q]$ is the vector of nodal displacements through the thickness of the entire plate, primes denote differentiation with respect to x , and dots denote differentiation with respect to time. Assuming that the wave propagates in the x -direction, $[Q]$ is taken to have the form [60]



Overlap of Nodal Displacements for Two Layers:

$$[q]_1^T = [u_x^b, u_z^b, u_x^m, u_z^m, u_x^f, u_z^f]_1 = [u_x^1, u_z^1, u_x^2, u_z^2, u_x^3, u_z^3]$$

$$[q]_2^T = [u_x^b, u_z^b, u_x^m, u_z^m, u_x^f, u_z^f]_2 = [u_x^3, u_z^3, u_x^4, u_z^4, u_x^5, u_z^5]$$

$$[Q]^T = [u_x^1, u_z^1, u_x^2, u_z^2, u_x^3, u_z^3, u_x^4, u_z^4, u_x^5, u_z^5]$$

Overlap of 6 by 6 Matrices: [m], [k₁], [k₂], and [k₃]:

Matrix elements in 1st layer

$$\left[\begin{array}{cccccc} 1 & 1 & 1 & 1 & 1 & 1 \\ 1 & 1 & 1 & 1 & 1 & 1 \\ 1 & 1 & 1 & 1 & 1 & 1 \\ 1 & 1 & 1 & 1 & 1 & 1 \\ 1 & 1 & 1 & 1 & X & X \\ 1 & 1 & 1 & 1 & X & X \end{array} \right] \quad 0 \quad \left[\begin{array}{cccccc} 2 & 2 & 2 & 2 & 2 & 2 \\ 2 & 2 & 2 & 2 & 2 & 2 \\ 2 & 2 & 2 & 2 & 2 & 2 \\ 2 & 2 & 2 & 2 & 2 & 2 \end{array} \right] [Q]$$

0

Matrix elements in 2nd layer

Figure 4.3 Demonstration of overlap of two finite element layers, where X in the figure indicates the overlap region in which the elements of the individual 6 by 6 matrices are added together.

$$[Q] = [Q_0]e^{i(kx - \omega t)}, \quad (4.25)$$

where $[Q_0]$ is the amplitude vector for the nodal displacements. Substituting equation (4.25) into equation (4.23) yields [60]

$$[-k^2[K_1] + ik[K_2^*] - [K_3] + \omega^2[M]][Q_0] = 0. \quad (4.26)$$

Equation (4.26) is an eigenvalue problem where one can choose the wavenumber, k , and solve for the eigenfrequencies, ω . The eigenvector, $[Q_0]$, for each solution is the displacement field through the thickness of the sample. From the solutions of ω and k , one can generate a dispersion curve for the composite. Examining the eigenvector for each curve allows one to label the various modes as either symmetric or antisymmetric.

To solve equation (4.26), a computer program was developed and written in FORTRAN. The code is shown in Appendix B. The user is allowed to input the material parameters (elastic stiffness constants, density, and plate thickness), the number of finite element layers to be used, and the range of wavenumbers to use. The program then steps through the various wavenumbers and its corresponding eigenfrequencies are calculated. A dispersion curve is then generated using the values for ω and k .

The symmetry of each mode can be identified by examining the amplitude eigenvector, $[Q_0]$. As can be seen from Figure 4.3, the odd elements of $[Q]$ correspond to the in-plane displacements, u_x , and the even values are identified as the out-of-plane displacements, u_z , through the thickness of the plate. Examining the symmetry of the displacements about the mid-plane of the plate for each ω and k pair allows one to identify the various modes as symmetric or antisymmetric.

The numerical calculations were performed on a DECstation 5000/200. The dura-

tion of the calculation depends on the number of layers chosen and the number of ω and k pairs for which to solve. A choice of 250 different wavenumbers, using a typical 8 layer model (which solves for 34 values of ω for each wavenumber) results in a total solution of 8500 ω and k pairs. This type of calculation takes only 45 seconds running on the above workstation. Increasing the number of layers, which increases the number of eigenfrequencies to solve for each wavenumber, or increasing the number of k -values for which to solve serves to increase the required calculation time.

4.2 Evaluation of Numerical Model

To evaluate the validity of the above numerical model, a simple isotropic case is examined. Analytical solutions exist for isotropic solids and were found in equations (3.85) and (3.86). The dispersion curves in Figure 3.8 were generated for a 0.1 cm thick aluminum plate using the material properties given in equation (3.93).

The above model was used to calculate dispersion curves for aluminum using these same material parameters. A simple 5 nodal layer model was used in the calculation and the results were compared to the analytical solutions arrived at using equations (3.85) and (3.86). The results are shown in Figure 4.4. The agreement between the two calculations is excellent, even though the plate is only divided into 5 layers. A slight deviation is seen, however, at higher frequencies. This is due to the choice of only a few layers. To achieve accuracy at higher frequencies, i.e. shorter wavelengths, additional layers are required. To show this breakdown at higher frequencies with fewer nodal layers, a 2 layer model was compared to the 5 layer model. The results are

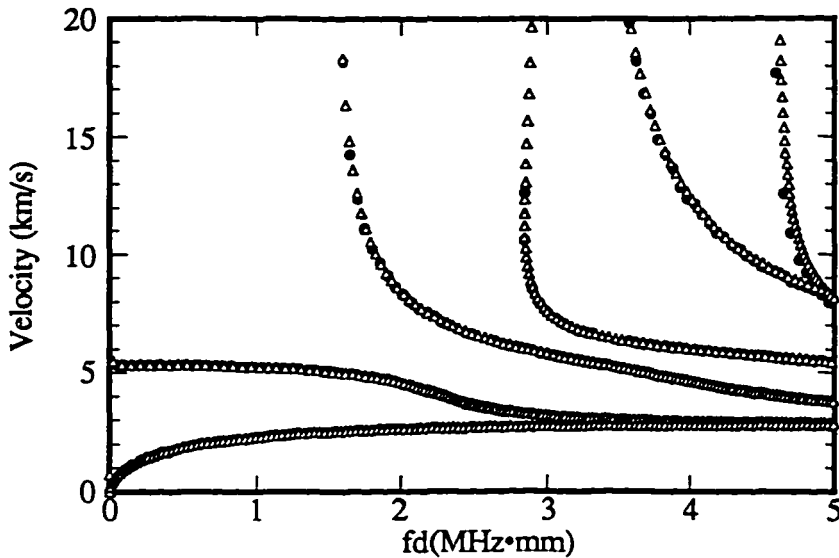


Figure 4.4 Analytical solution (solid circles) versus a 5 layer numerical model (open triangles) for a 0.1 cm thick aluminum plate.

shown in Figure 4.5. The agreement at low frequencies is extremely good, but a significant deviation between the curves is seen as the frequency increases.

To examine the symmetry of the modes, the displacements for the first four Lamb modes, obtained from the eigenvectors $[Q_0]$, are examined for a 0.1 cm thick plate of aluminum. To increase the smoothness of the curves, however, a 10 layer model was used which allows for the solution of 42 distinct displacements (21 for u_x and 21 for u_z) through the thickness of the plate. The wavenumber was chosen to be 5000 m^{-1} for each of the solutions. The solutions are shown in Figure 4.6. The exact shape of the displacements is different from the analytical values, however, the *symmetry* calculated using the model is the same as that obtained for the first two Lamb modes using the analytical solutions (Figure 3.9). The observed difference in shape between the analyti-

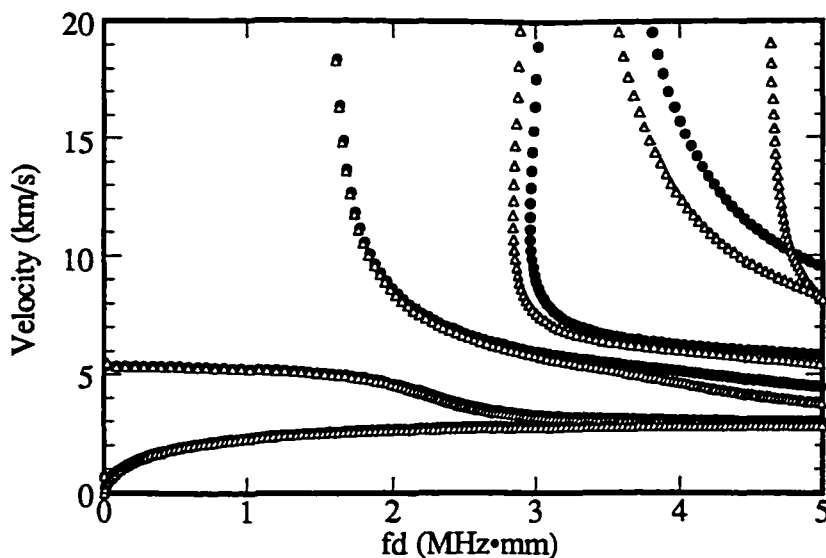


Figure 4.5 A 2 layer model (solid circles) versus a 5 layer model (open triangles) for aluminum showing the breakdown at higher frequencies when using fewer layers.

cal and numerical displacements is merely a consequence of the analytical displacements being calculated at a different fd product than the numerical displacements.

The model provides agrees well when compared with analytical solutions for an isotropic solid. To examine the validity for composites, a numerical calculation was done for an AS4/3501-6, [0/90₃]_S composite. A total of 8 nodal layers, one nodal layer for each lamina, was used in the calculation. The thickness of the plate was taken to be 0.12 cm and the material properties used are shown in Table 4.1 [2]. The values for the 90° layers were arrived at using the transformations given by equation (4.5). The results of the calculation are shown in Figure 4.7. The numerical curves shown in the figure will be compared to experimentally determined dispersion curves in the next chapter.

Examination of the displacements for the S_0 and A_0 modes of the above compos-

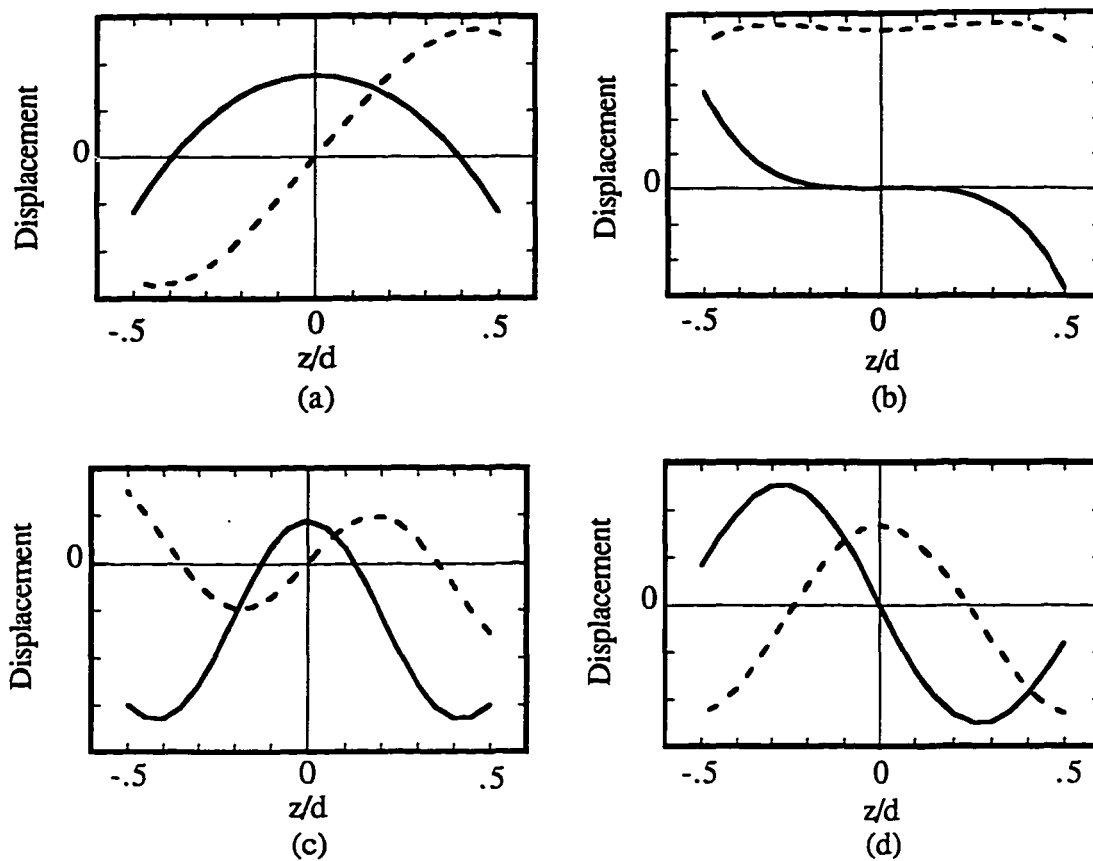


Figure 4.6 Plot of the particle displacements u_x (solid) and u_z (dashed) showing the symmetry of the first four Lamb modes in aluminum: (a) S_0 , (b) A_0 , (c) S_1 , and (d) A_1 . Note: $d = 0.1$ cm is the plate thickness.

Table 4.1 Material properties for an AS4/3501-6 composite (from reference 2).

Property	0° Layers	90° Layers
ρ (kg/m ³)	1580.0	1580.0
c_{11} (GPa)	144.54	12.23
c_{13} (GPa)	4.58	4.73
c_{33} (GPa)	12.23	12.23
c_{23} (GPa)	4.73	4.58
c_{55} (GPa)	7.17	3.75

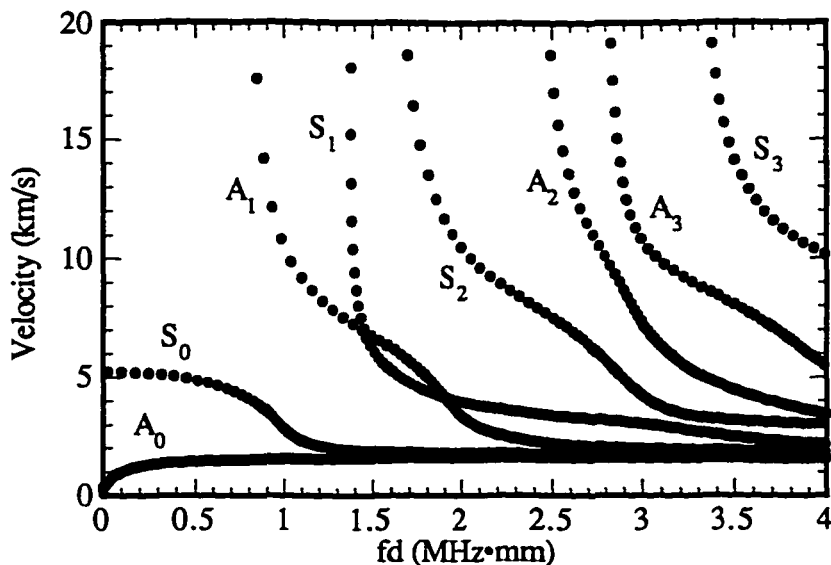


Figure 4.7 Numerical dispersion curves for an AS4/3501-6, [0/90]_S composite.

ite yields a very interesting feature, which is characteristic of these types of architectures. To increase the smoothness of the curves, four nodal layers were used in each lamina, which allows for 130 distinct displacements (65 for u_x and 65 for u_z) through the thickness of the plate. The wavenumber was chosen to be 10,000 m⁻¹ for each of the two solutions. The displacement fields through the thickness of the plate are shown in Figure 4.8.

The symmetry of the two modes shown is clear from the observed shape of the displacements. The interesting thing to note, however, is the behavior of the displacements at the boundary between the 0° and 90° layers. The transition at the interface of out-of-plane displacements, u_z , is smooth, while a “kink” is observed at the boundary for the in-plane displacements, u_x . This is a consequence of rotating the material parameters when the fiber direction of the layers is changed. The in-plane displace-

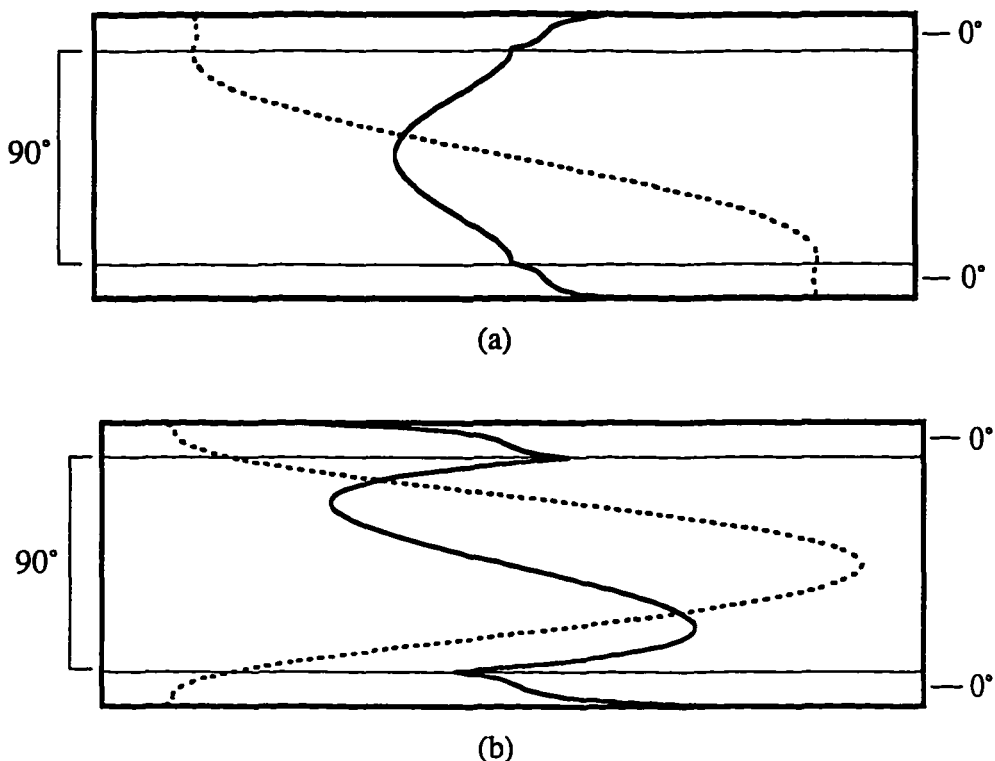


Figure 4.8 Plot of the particle displacements u_x (solid) and u_z (dashed) through the thickness of the plate showing the behavior in the 0° and 90° plies for (a) the S_0 mode and (b) the A_0 mode.

ments, u_x , do not show a smooth transition because the direction displacement changes from travelling perpendicular to the fibers to propagating parallel to them. A smooth transition is observed, however, for u_z , due to the fact that the displacements are perpendicular to the fibers for both the 0° and 90° layers, i.e. the motion is out of the plane of the plate.

The numerical curves were generated using the elastic stiffness constants in Table 4.1, but differences in the shape of the curves can arise due to the choice of the stiffness parameters. The material properties listed in the literature for graphite/epoxy com-

Table 4.2 Comparison of material properties obtained from the manufacturer (Row 1) versus those obtained using experimental Lamb wave velocity measurements (Rows 2 and 3). Data is from reference 28.

ρ (kg/m ³)	c_{11} (GPa)	c_{12} (GPa)	c_{22} (GPa)	c_{23} (GPa)	c_{55} (GPa)
1560	147.48	4.47	11.05	3.86	5.97
1580	147	4.47	14	7.35	4
1580	161	4.47	14	7.35	4.5

posites [2, 27-28, 61-64] do not all agree with one another and altering these values changes the shape of the dispersion curves. Additionally, due to variations in manufacturing such as porosity and fiber-volume fraction, the measured elastic stiffness values do not always coincide exactly with published values.

Mal, et al. [28] used an inversion scheme and experimental Lamb wave velocity measurements to determine the five independent elastic stiffness constants for a unidirectional, AS4/3502 composite. The data was then compared to the material properties provided by the manufacturer. The results are shown in Table 4.2. As is obvious from the table, the parameters as quoted by the manufacturer do not always agree with measured values. The next section of this chapter investigates the influence of each of the elastic stiffness constants on the shape of the dispersion curves.

4.3 Influence of the Elastic Constants on the Dispersion Curves

To investigate how the dispersion curves produced by the numerical model are altered by a variation in the elastic stiffness parameters, theoretical dispersion curves

were calculated for a unidirectional, AS4/3501-6 composite using reduced stiffness constants. The effect of reducing different c_{IJ} 's by 20% was investigated. Calculations were done for propagation along the fibers, as well as across the fibers. A simple 5 nodal layer model was chosen and the thickness of the plate was taken to be 0.1 cm. The material parameters used are those listed in Table 4.1. The results for propagation along the fiber direction, as well as perpendicular to the fibers, are shown in Figures 4.9 and 4.10, respectively. The influence of the elastic constants for propagation 45° with respect to the fibers is not treated here. The results for this case can be found in Mal, et al. [64] and are similar to the propagation directions reported here.

For the case of propagation along the fibers, a reduction in c_{11} serves to lower the velocity of the various modes. This is expected because the velocity in the propagation direction is related to the modulus of the material in that direction. A reduction of c_{33} shifts the frequency of mainly the symmetric modes. Reducing c_{55} predominately alters the antisymmetric modes. This is reasonable to expect because c_{55} , which equals c_{66} , is the shear modulus, which relates the out-of-plane displacements to propagation in the plane of the plate. Since the antisymmetric modes are mainly a flexing motion, a reduction in c_{55} will affect these modes. Finally, a reduction in all of the constants produces a downward shift in the curves.

For the case of propagation across the fibers, a reduction in c_{33} serves to lower the velocity. Since c_{33} is the modulus across the fibers, a drop in velocity will coincide with a decrease in this parameter. Reducing c_{23} actually serves to shift the curves up and to the right. As was seen for propagation along the fibers, reducing all of the parameters shows a similar downward shift in the curves.

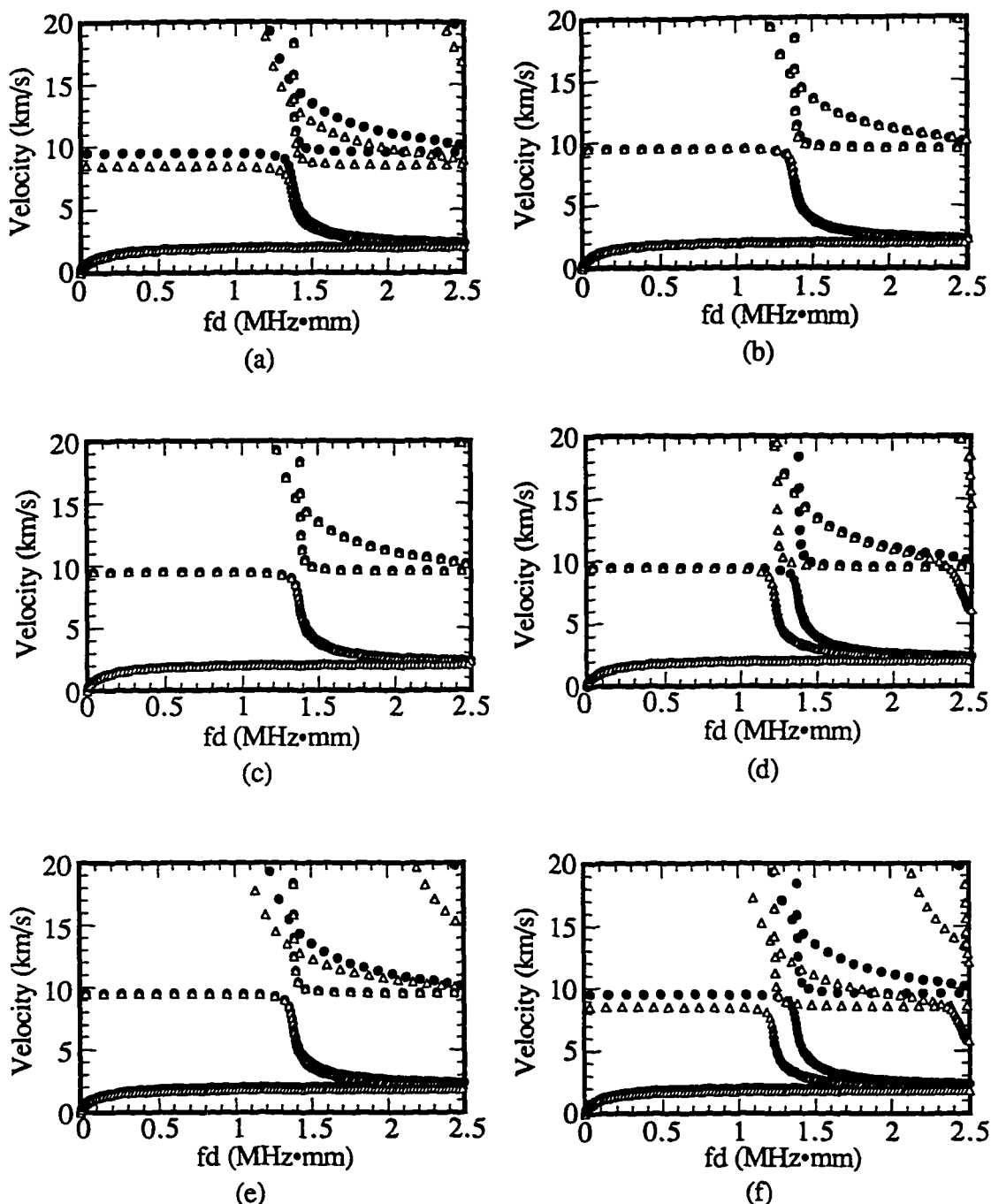


Figure 4.9 The effect of reducing the various elastic stiffness constants by 20% on the dispersion curves for a unidirectional composite. The propagation direction is parallel to the fibers and the parameters reduced are: (a) c_{11} , (b) c_{13} , (c) c_{23} , (d) c_{33} , and (e) c_{55} . All of the constants were reduced in (f). In all figures, solid circles represent calculations with full parameters and open triangles represent calculations using reduced parameters.

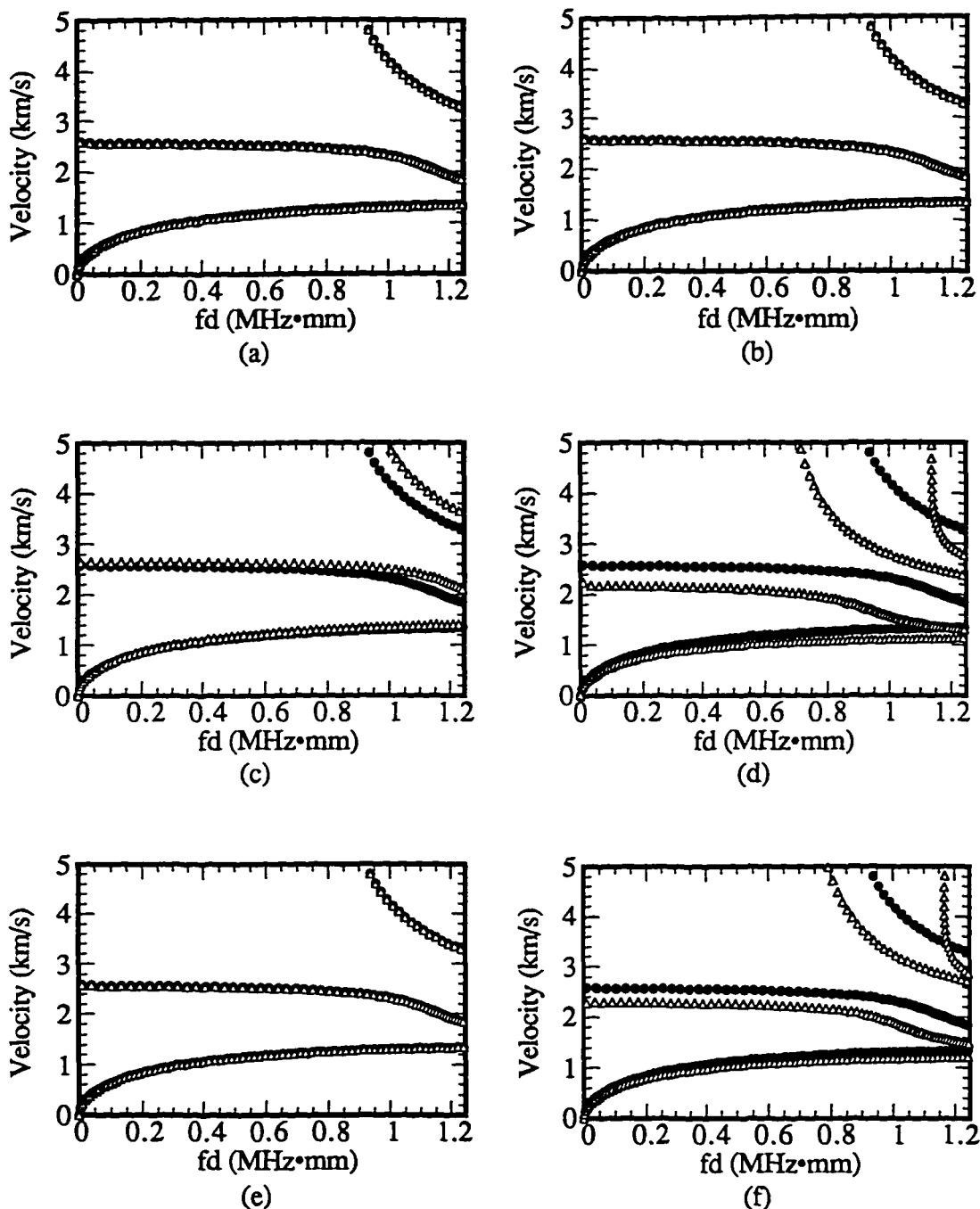


Figure 4.10 The effect of reducing the various elastic stiffness constants by 20% on the dispersion curves for a unidirectional composite. The propagation direction is perpendicular to the fibers and the parameters reduced are: (a) c_{11} , (b) c_{13} , (c) c_{23} , (d) c_{33} , and (e) c_{55} . All of the constants were reduced in (f). In all figures, solid circles represent calculations with full parameters and open triangles represent calculations using reduced parameters.

The parameter c_{13} showed no influence on the curves for propagation in either direction. In addition, c_{23} did not affect the propagation in the fiber direction and neither c_{11} nor c_{55} affected the curves for propagation across the fibers. The results shown in Figures 4.9 and 4.10, and discussed above, are in good agreement with those found by Mal, et al. [28], who studied the influence of the various parameters on the lowest order antisymmetric mode.

Depending on the propagation direction and fiber orientation, the various stiffness constants affect the behavior of the dispersion curves in different ways. It is exactly this dependence which allows one to use Lamb waves to effectively monitor damage in composite materials. Different types of damage alter different elastic stiffness parameters. By measuring a change in the Lamb wave velocity due to material degradation and comparing the experimental values to theory, an effective method to nondestructively monitor the health of composites can be developed. The following chapter discusses various experimental methods available to generate, detect, and measure the velocity of Lamb waves.

Chapter 5

Experimental Techniques

A transducer is a device which converts one form of energy into another. Materials which are capable of converting mechanical energy into electrical energy, and vice versa, are known as piezoelectrics. Here, the mechanical energy is in the form of a pressure, which serves to distort a material, and the electrical energy is in the form of an applied voltage. Due to the unique properties of these materials, piezoelectric transducers are commonly used in ultrasonic measurements.

5.1 Generation and Detection of Lamb Waves

A typical method for detecting Lamb waves involves placing a longitudinal contact transducer, which measures mainly out-of-plane displacements, onto a plate. Because of the impedance mismatch between air and common piezoelectric solids, there is almost no transmission of ultrasonic energy from the piezoelectric crystal into the air. The acoustic impedance of common piezoelectrics is on the order of 10^7 Ns/m^3 [65] and the impedance of dry air 414 Ns/m^3 [66]. This large mismatch results in a transmission of only 0.005% of the signal from the crystal into the air. Therefore, to achieve transmission of the acoustic wave, the transducer must be coupled to the plate

with water or a gel couplant. The signals from the transducer are amplified and can then be viewed on an oscilloscope or digitizer.

Several methods exist to generate Lamb waves. Breaking a pencil lead on the plate provides a step unloading on the surface, which excites Lamb modes. This type of source gives a broad range of frequencies in the signal. A longitudinal transducer can also be used to generate Lamb waves by sending a sinusoidal tone burst at a given frequency. Since the plate is being driven at a particular frequency, this method is useful if the velocity of the wave is only desired for a very narrow frequency band. Another advantage is that it provides a consistent signal source. The lead break source depends on several factors, which include the type of lead and the angle of the break with respect to the plate. Additionally, lasers may be used to excite Lamb modes. At lower powers, the waves are generated by a local thermal expansion. At higher powers, ablation occurs and generates the acoustic waves in the material. The following sections will detail lead break and tone burst sources.

5.1.1 Lead Break Source

A lead break on the surface of a plate produces a deformation in the out-of-plane direction. This will tend to preferentially excite Lamb modes which are dominated by this type of displacement. A lead break on the edge of the plate, which produces an in-plane deformation, will tend to excite those modes dominated by this motion. At low frequencies, as was seen in Section 3.3.2, the lowest order antisymmetric mode, A_0 , is dominated by out-of-plane displacements, whereas in-plane displacements are domi-

nated by the lowest order symmetric mode, S_0 . Therefore, a lead break on top of the plate will tend to excite the A_0 mode, and a lead break on the edge will tend to excite the S_0 mode.

Sample signals from a 0.5 mm diameter lead break were taken for a 16 ply unidirectional composite plate (AS4/3502) with dimensions of 16 by 20 inches. The large size was chosen to avoid unwanted reflections from the edges, which would interfere with the Lamb modes. The signals were received by a Harisonic model CM-0008-S 0.5 inch diameter longitudinal transducer with a nominal center frequency of 0.5 MHz.

Results for a lead break on top of the plate at distances of 4 and 8 cm from the receiving transducer are shown in Figure 5.1. For comparison, the signals for a lead break on the edge of the same composite are shown in Figure 5.2. Again, the distances from the break to the receiver were taken to be 4 and 8 cm. The propagation direction for both measurements was along the fibers of the composite. Also, since a longitudinal transducer was used to detect the waves, the signals shown in the figures are the out-of-plane displacements of the Lamb modes. Finally, to achieve a decent signal-to-noise ratio for the S_0 mode in Figure 5.1, the A_0 mode had to be amplified to saturation.

For all of the signals, the first mode to arrive is the lowest order symmetric mode, S_0 , followed by the antisymmetric mode, A_0 . Also noted in all of the signals is the lack of dispersion for the S_0 mode and the dispersive nature of the A_0 mode. For the anti-symmetric mode, the higher frequency components arrive first, followed by the lower frequencies. Therefore, the higher frequencies are travelling faster than the lower ones. Examination of the dispersion curves shown in Figure 3.8 shows that for low frequency-thickness values: S_0 is much faster, A_0 is highly dispersive, and the lower fre-

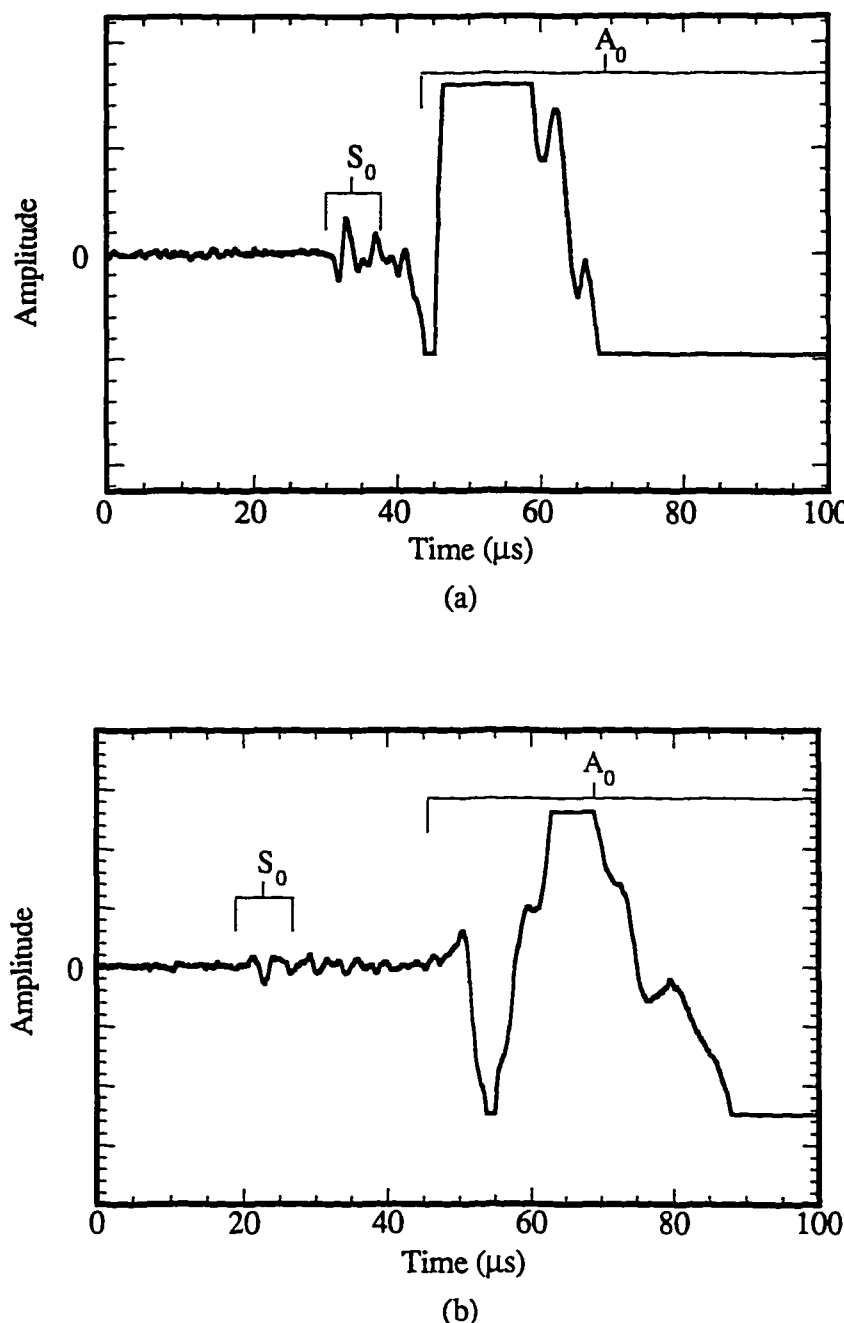


Figure 5.1 Signals from a lead break source on top of a unidirectional composite plate (AS4/3502, $[0_{16}]$): (a) transducer 4 cm from source and (b) transducer 8 cm from source. Propagation was along the fiber direction.

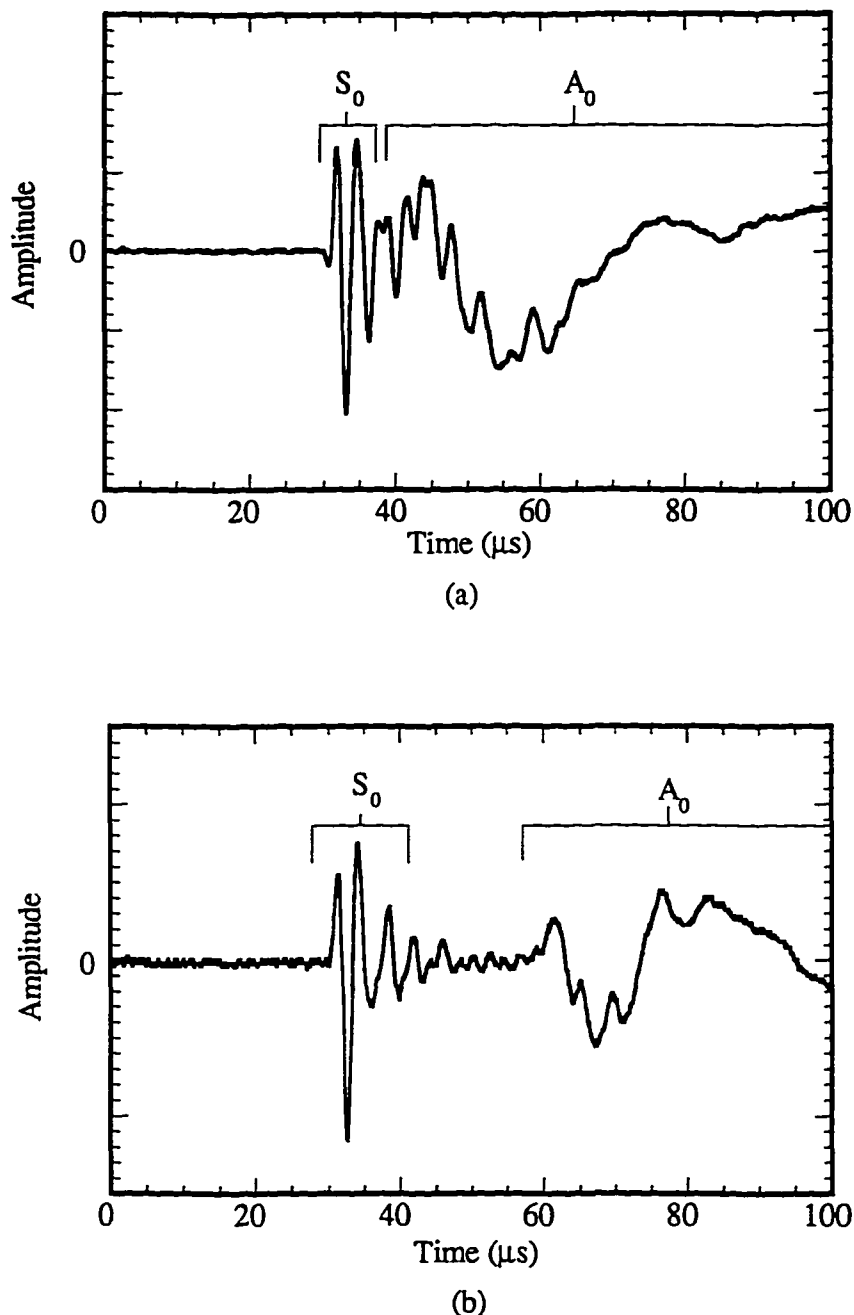


Figure 5.2 Signals from a lead break source on the edge of a unidirectional composite plate (AS4/3502, $[0_{16}]$): (a) transducer 4 cm from source and (b) transducer 8 cm from source. Propagation was along the fiber direction.

quencies of the A_0 mode, travel more slowly than the higher frequencies. Although the dispersion curves shown in Figure 3.8 are for aluminum, the general shape of dispersion curves for composites is similar. Therefore, the above results are all characteristic of the lowest order Lamb modes.

Another feature to note is that the modes separate from each other with increased propagation distance. This just shows that the modes are travelling at different velocities. Also, as mentioned at the beginning of this section, a lead break on top of the plate preferentially excites an A_0 mode, and a break on the edge tends to excite an S_0 mode. This behavior is shown quite well by Figures 5.1 and 5.2. For a break on the top, Figure 5.1, it is obvious that the antisymmetric mode is preferentially excited. For a break on the edge, Figure 5.2, the signal is dominated by the symmetric mode. Therefore, by breaking a lead on a given surface (top or edge), one can excite a desired mode.

5.1.2 Tone Burst Excitation of Lamb Modes

The lead break method of exciting Lamb waves described above excites a broad band of frequencies in the plate. An alternate method exists which drives a plate at a given frequency. This is sometimes a preferred technique because it provides a very consistent excitation source.

Lamb modes can be generated by placing a longitudinal contact transducer on a plate and driving it with a sine wave tone burst. Ditrí, et al. [67] showed that periodic loading normal to the surface of a plate, as produced by a longitudinal transducer, will excite Lamb waves at distances away from the source which are large compared to the

wavelength of the Lamb mode. The solution procedure used was similar the one described in Section 3.3.1, which made use of potentials to decouple the equations. The difference is that the equations are written in terms of cylindrical coordinates, and the boundary conditions used are for a time harmonic loading on one surface of the plate for radial distances of less than the diameter of the transducer.

The cylindrical waveforms produced by the transducer were shown by Diti, et al. [67] to have the same wavenumbers and frequencies as Lamb waves. The main difference between the two waves is that Lamb waves propagate harmonically in the radial direction, i.e. $e^{i(kr - \omega t)}$, and the solutions for the cylindrical waves vary radially as Hankel functions. It is noted, however, that in the large r limit, Hankel functions approach periodic behavior [67]. It was subsequently shown that for values of $r/\lambda \approx 0.5$, the cylindrical waves approached Lamb waves, where r is the distance from the center of the transducer, and λ is the wavelength of the Lamb mode [67].

At frequencies of 200 kHz and higher, typical Lamb wave wavelengths, depending on the type of material, are less than 1 or 2 cm for the S_0 mode and less than 0.1 cm for the A_0 mode. Thus, Lamb waves will be generated in most materials at a distance of roughly 1 cm or less. For commonly used 0.5 inch diameter transducers, this is just outside the radius of the transducer face. Since measurements are normally done anywhere from 5 to 50 cm away from the source, this does not create any difficulties in generating and measuring Lamb modes using this technique.

A sample of the signals generated by a Harisonic (model CM-0008-S) 0.5 inch, 0.5 MHz longitudinal transducer is shown in Figure 5.3. The input used was a 6 cycle, 0.5 MHz sine wave tone burst. The receiving transducer was a Valpey-Fisher model

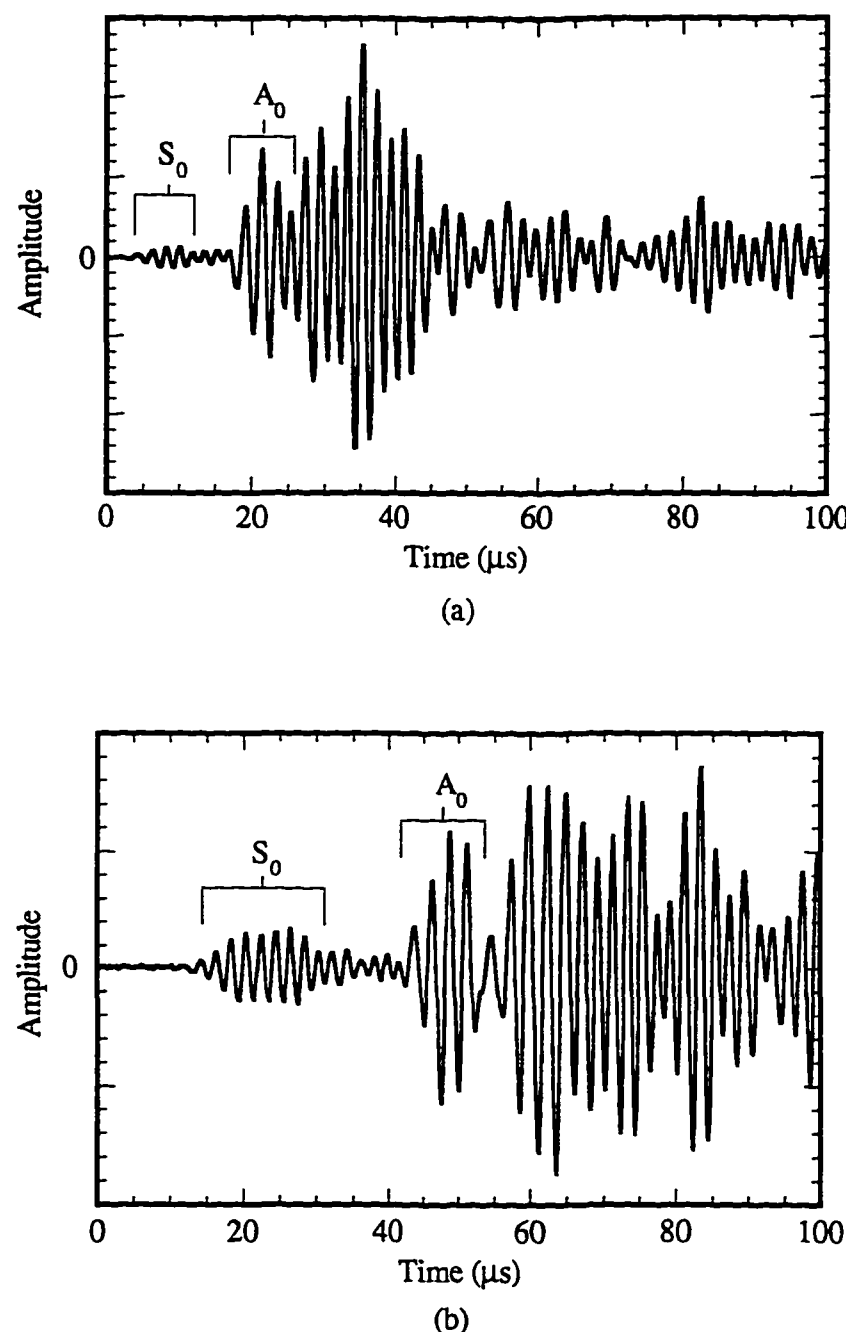


Figure 5.3 Signals generated from a tone burst source by a longitudinal transducer on the top of a crossply composite plate (AS4/3501-6, [0/90₃]_S): (a) transducer 4 cm from source and (b) transducer 8 cm from source. Propagation was along the 0° direction.

VP-1093 pinducer which had an active area of 0.135 cm. The pinducer has been characterized by Prosser [58] and is broadband with a frequency range up to 1.2 MHz. The Lamb wave velocity was measured in the 0° direction of an AS4/3501-6, [0/90₃]S composite with a thickness of 0.107 cm and a width of 3.81 cm.

Many of the characteristics of the tone burst excitation are similar to the lead break source described above. Since the plate is driven at a low frequency, only the two lowest order modes propagate, and the S₀ mode is the first to arrive. The two modes also separate with distance. A longitudinal transducer placed on top of a plate excites mainly out-of-plane displacements. Thus, similar to a lead break on top, the antisymmetric mode is preferentially excited.

There are two main differences between the tone burst signals shown in Figure 5.3 and the lead break signals shown in Figures 5.1 and 5.2. First, since the plate is being driven at a particular frequency by a tone burst, the signals in Figure 5.3 are all propagating in a narrow frequency band. This is the reason no dispersion is easily seen in the A₀ mode. In contrast, the lead break source was seen to generate a broad band of frequencies. Thus, the tone burst technique is very useful for making measurements at a particular frequency-thickness product. Second, the lead break measurements were done on a large (16 by 20 inch) composite panel. Therefore, no edge reflections were seen, and the modes were easily distinguishable. The sample used for the tone burst excitation was only 1.5 inches wide and, hence, edge reflections were observed. These reflections are what account for the signals seen after the arrival of the A₀ mode.

Most measurements are conducted in small plates where edge reflections play an important role. From Figures 5.1-5.3, it is clear that the easiest mode to detect is the

lowest order symmetric mode. It is the first arrival and does not interfere with these reflections. Thus, it is easy to identify from the other modes or reflections. Techniques to measure the velocity of this mode are detailed in the next section.

5.2 Velocity Measurements

The velocity of the lowest order symmetric mode is measured because it is easily identifiable and propagates at long wavelengths. Measurements at long wavelengths are desired in composites in order to gauge effective stiffness properties and not the individual components of the composite. Also, a significant increase in attenuation is seen as the frequency of the wave increases.

The only problem with measuring the S_0 mode is generating a good signal. Figures 5.1 and 5.2 show that a lead break on the edge of a composite preferentially excites the S_0 mode, and a lead break on top excites mainly an A_0 mode. On most composite structures, such as airplanes, an edge is not readily available on which to generate this mode. Therefore, the mode must be generated on top of the surface. A lead break or tone burst on top of a plate only generates a small amplitude S_0 mode (see Figures 5.1 and 5.3). Since one is only concerned with the first arrival, the signal is amplified in order to obtain a good signal-to-noise ratio for the symmetric mode. This may saturate the later A_0 waves and reflected signals. Figure 5.4 shows the same pulse displayed in Figure 5.3a, except the portion of the signal which follows the symmetric mode has been amplified to saturation.

To measure the velocity, the signals are received at various positions, digitized,

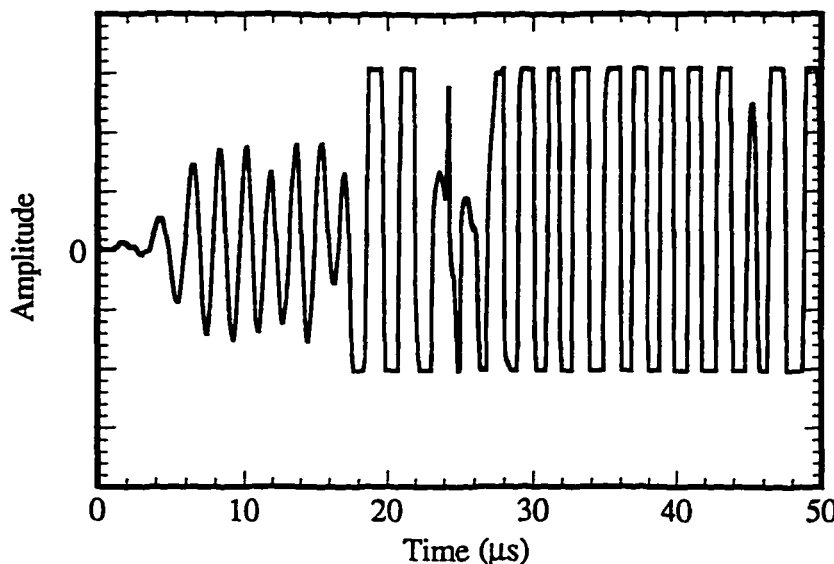


Figure 5.4 The same signal shown in Figure 5.3a, except remaining signal has been saturated to obtain a good signal-to-noise ratio for the S_0 mode.

and saved to a computer. The time differences between the signals are measured either by imposing a computational delay on the first signal to overlap the signals received at greater distances or by doing a cross-correlation on the saved waveforms. The distances between transducers can be measured by using a single transducer and moving it a known distance or by using an array of transducers fixed in a holder. From a plot of time and distance, a least-squares fit can be performed to obtain the velocity of the S_0 mode. The two experimental arrangements are shown in Figure 5.5. Figure 5.5a shows the source as a lead break with a reference transducer and a transducer which is moved. Figure 5.5b shows a tone burst with a transducer array. Any combination of sources and receivers can be used to perform the measurement. It is not limited only to the ones shown in the figure.

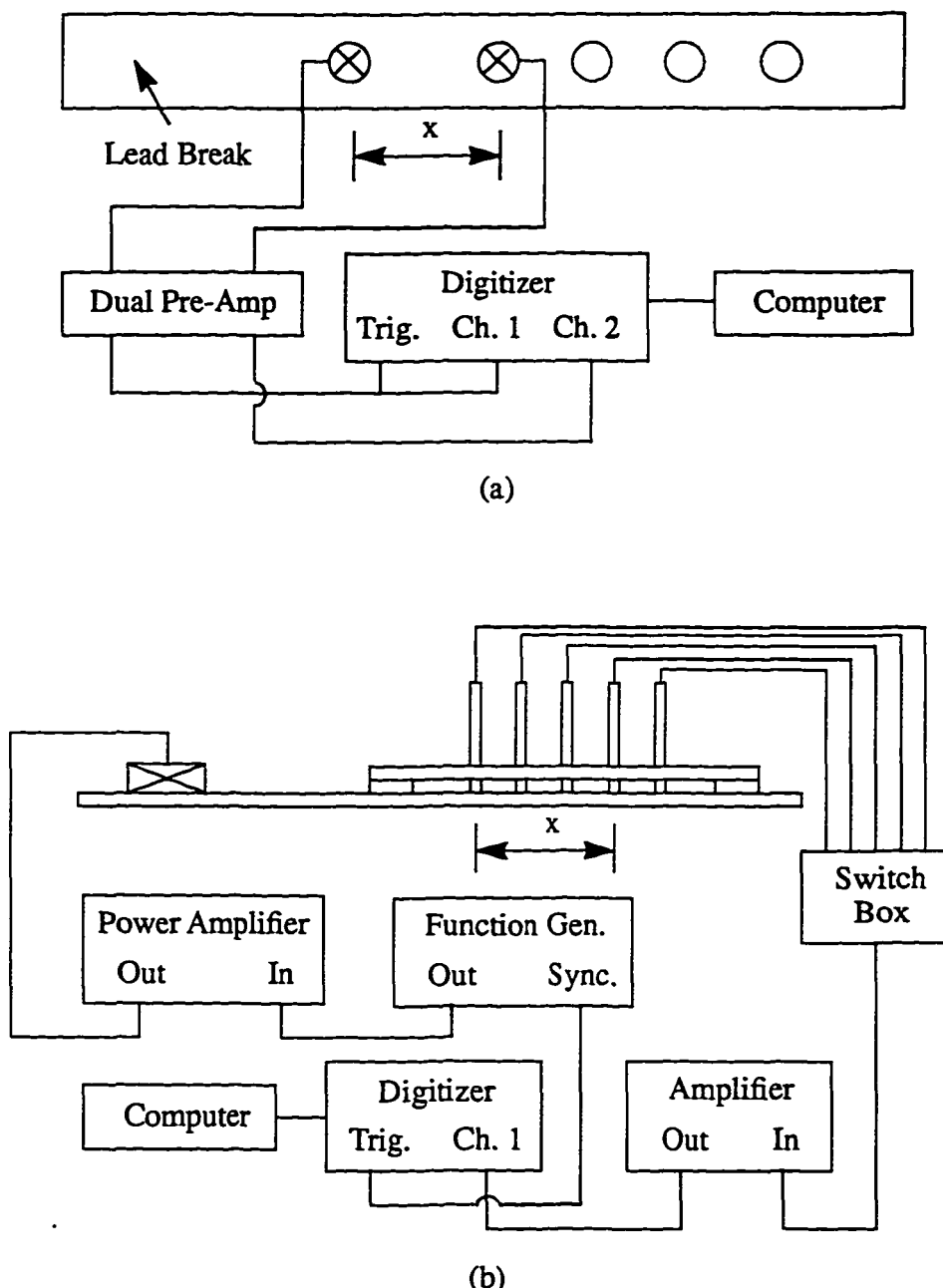


Figure 5.5 Possible experimental arrangements include: (a) a lead break source, reference transducer, and second transducer at a distance x from the reference and (b) a tone burst source and pinducer array.

5.2.1 Distance Measurements

When receiving signals using two transducers, one reference and one which is moved, the separation between the two can be measured by various means. A ruler can be used to measure the distance (center-to-center) between the transducers. The problem with this technique is that there is an error which is incurred in the distance measurement. Another method, which is very accurate, is to measure the center-to-center distance with a sonic ranger, which provides an accuracy of 0.01 cm. This allows for a precise measurement, but there still exists an error in the known distance due to the large active area of typical contact transducers (0.5 inches).

The transducer array, shown in Figure 5.5b, provides an improved method to accurately measure the separation between transducers. Because of the smaller active area (0.135 cm), the distance error due to the size of the transducer is greatly reduced. Also, the pinducers are small enough so that they can be fixed in a holder and kept at a constant separation. Even if the separation is not known exactly, the error is consistent throughout all measurements. This would result in the actual velocity being slightly incorrect, but what one is usually concerned with is a change in velocity due to a change in material properties (i.e. a differential measurement). Thus, this error would not affect this type of measurement.

5.2.2 Time Measurements

Sample signals from two transducers separated by a distance of 5.5 cm are shown in Figure 5.6. The time difference between the signals can be measured using different

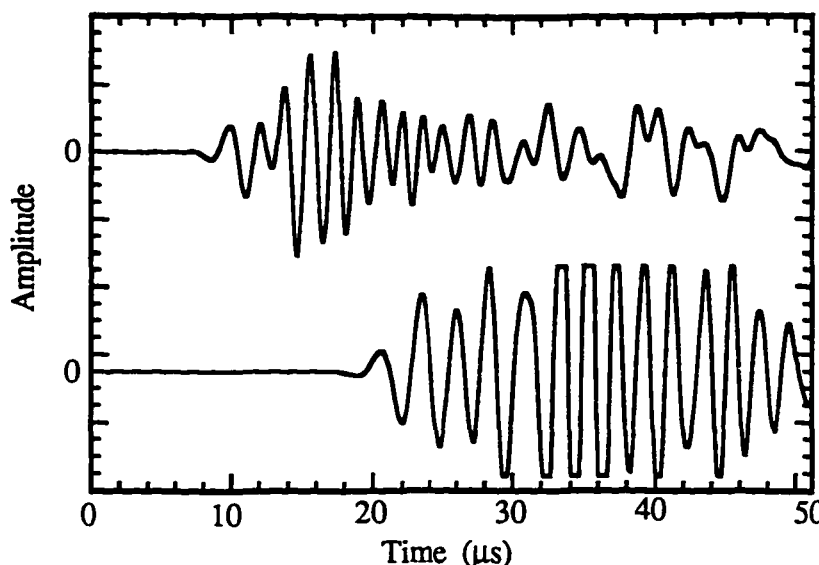


Figure 5.6 Sample signals separated by a distance of 5.5 cm. The amplitudes have been offset from each other in order to show the waveforms clearly.

methods. A computational time delay may be imposed on the first signal to overlap the signal received at a greater distance. Even though the symmetric mode is not very dispersive, there still exists a small difference in the frequency content of the two signals. Therefore, only the initial portion of the signal is overlapped. Another method of calculating the time difference is to perform a cross-correlation on the two signals. Again, only the first portion of the wave is used due to the slightly dispersive nature of the mode. Figure 5.7 shows an original signal, the cutoff waveform (which limits the correlation to only the initial arrival), and the resulting cross-correlation. The desired time difference is obtained from the value of the maximum correlation.

Not shown in the figure is the second waveform received at a further distance. It is cut off in the same manner as the signal shown in Figure 5.7b, and the correlation shown in Figure 5.7c is the result. In order to eliminate noise and isolate the first sig-

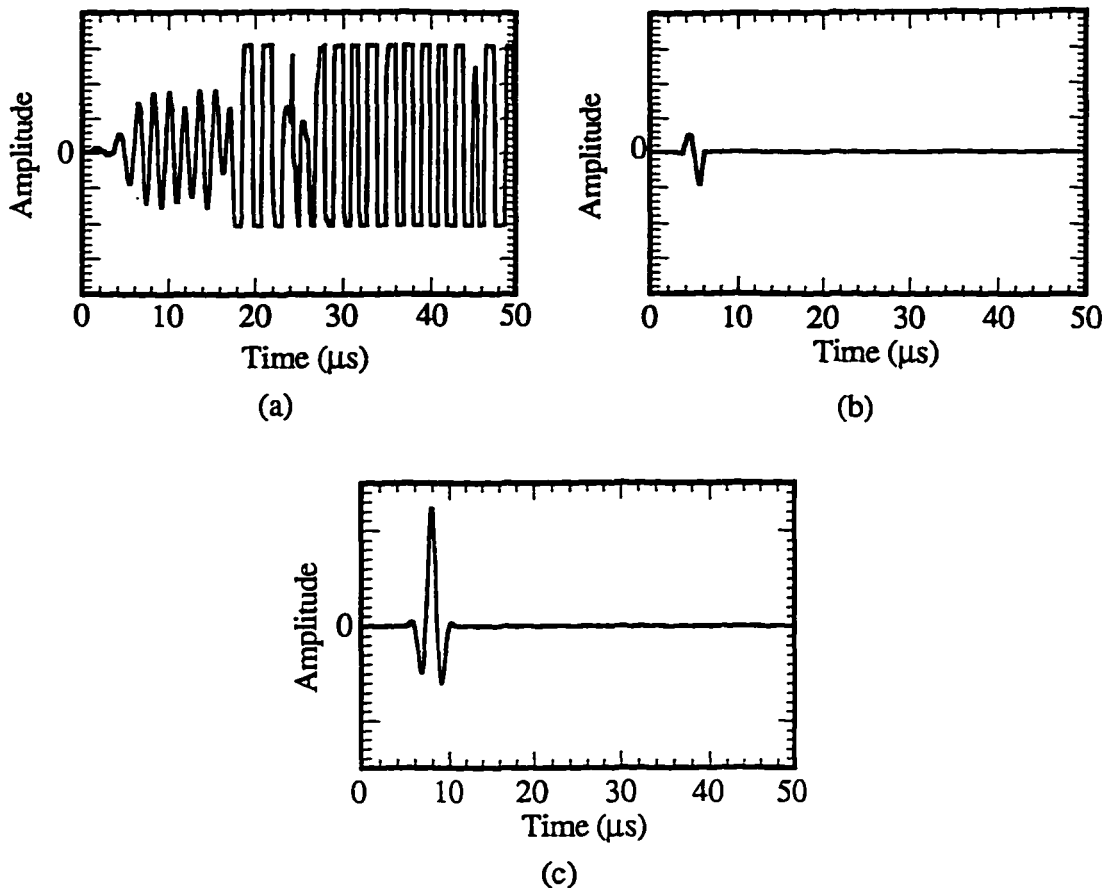


Figure 5.7 Cross-correlation technique for determining the time difference between signals showing: (a) the original signal, (b) the initial portion of the wave cut off for correlation, and (c) the resulting cross-correlation of the cut-off waveforms.

nal arrival, the initial portion of the signal is exponentially fit to zero and, after one full wave, the trailing portion is cut off at the zero crossing (after which all values are set equal to zero).

5.2.3 Comparison of Lead Break and Tone Burst Velocities

Both lead break and tone burst velocities were measured for an AS4/3501-6 composite samples with an architecture of $[0/90_3]_S$. For the lead break measurement, two

Panametrics model V103 1.0 MHz, 0.5 inch diameter transducers were used to receive the signal. The arrangement used was as shown in Figure 5.5a. The separation distance, center-to-center, was measured using a ruler and the signal was digitized at 5.0 MHz. The time differences were measured using a cross-correlation. Four distance and time pairs were measured, and a least-squares fit was done to obtain the velocity.

For the tone burst measurement, a 2 cycle sine wave was used to excite the wave. A second transducer was used to detect the wave at various positions. Both the sending and receiving transducers were the same as used in the above lead break measurement. The separation distances were measured to an accuracy of 0.01 cm using a Graf/Bar sonic ranger and the signals were digitized at 10 MHz. The time differences were measured by imposing a computational delay on the first signal to overlap those received at a greater distance. Again, four distance and time pairs were measured, and a least-squares fit was done to obtain the velocity. Table 5.1 shows the results of these measurements.

The velocities for the tone burst measurement are the average of three measurements and the errors shown are the standard deviation for the three values. The lead break velocities are for a single measurement. The errors shown are an estimated by assuming a ± 2 mm error in the distance measurement using a ruler and a ± 1 channel error in the time measurement due to the cross-correlation overlap of the digital signals. These estimates translate into an approximate total error of 5% for the lead break velocities.

The errors in the averages for all nine samples are the standard deviations of the tone burst and lead break velocities, respectively. The velocities measured using two

Table 5.1 Tone burst velocity measurements versus lead break velocity measurements for nine composite samples with the same architecture.

Sample	Tone Burst Velocity (km/s)	Lead Break Velocity (km/s)
1	5.25 ± 0.11	5.20 ± 0.26
2	5.37 ± 0.14	5.29 ± 0.26
3	5.43 ± 0.14	5.04 ± 0.25
4	5.48 ± 0.08	4.94 ± 0.25
5	5.36 ± 0.08	5.73 ± 0.29
6	5.41 ± 0.05	5.04 ± 0.25
7	5.35 ± 0.14	5.13 ± 0.26
8	5.33 ± 0.09	5.03 ± 0.25
9	5.54 ± 0.06	5.10 ± 0.26
Avg. Vel. (km/s)	5.39 ± 0.09	5.17 ± 0.23

different techniques compare well. The main thing to note, however, is that the standard deviation in the average of all nine samples for the tone burst velocities is much less (1.5% of the average) than the lead break velocities (4.5% of the average). Also, for each individual sample, the error in the velocity is lower in the tone burst measurements than the lead break measurements. This is primarily due to the more consistent generation of the tone burst signal and better distance measurement accuracy using the sonic ranger. Also, the signal from the tone burst source was less noisy than the signal from the lead break. This allows for a better overlap of the waveforms. Finally, for the tone burst technique, the plate was being driven at a constant frequency of 0.5 MHz. For the lead break measurements, the frequency content ranged anywhere from 200-300 kHz. As mentioned before, the S_0 mode is slightly dispersive. This inconsistency

in frequency could account for the scatter in velocity in the lead break signals, as well as the difference in the velocity measurements between the tone burst and lead break.

5.3 Immersion Method

The tone burst technique described in the above section involves the measurement of the velocity of the S_0 Lamb mode at a single frequency. This allows the determination of only one point on the dispersion curves. The lead break method described above provides broadband signals which can be analyzed for dispersion, however, an alternate method is available to determine a portion of the dispersion curves over a particular frequency range. The only drawback to this technique is that it requires the sample to be immersed in water, which is usually impossible for large structures such as aircraft. The experimental arrangement for this type of measurement is detailed by Balasubramaniam, et al. [68] and is shown in Figure 5.8.

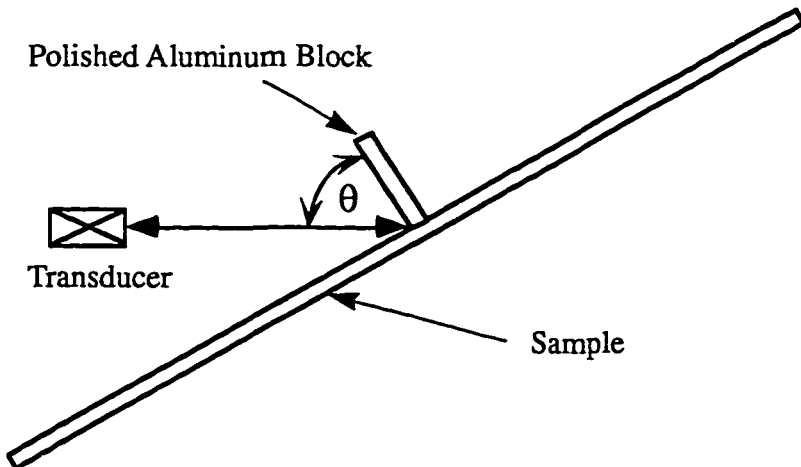


Figure 5.8 Experimental arrangement for determining dispersion curves of thin plates.

In this method, the sample is immersed in water, which serves as the couplant between the transducer and the plate, and the same transducer is used to generate and receive the ultrasonic signal. This type of arrangement is known as a pulse-echo technique. An aluminum block serves as a corner reflector for the input pulse. In this experiment, the specimen is rotated about the corner. When a Lamb wave is excited in the plate, part of the total energy is converted to a propagating Lamb mode. Due to this loss of energy, a minimum in the frequency spectrum of the reflected signal corresponds to the frequency at which a Lamb mode is propagating.

The reflected waveform at each angle is saved for later analysis of the frequency content. The velocity can be determined from Snell's law using the fact that only a longitudinal wave is supported in water and that the Lamb mode is propagating in the plate. The velocity of the Lamb wave is, therefore, given by

$$v_{\text{Lamb}} = \frac{v_{\text{water}}}{\sin(\theta)} . \quad (5.1)$$

After determining the frequency of the minimum for each angle, the velocity versus the frequency-thickness product can be plotted to obtain the dispersion curve. The frequency range is determined by the bandwidth and frequency of the transducer used. Using a 1.0 MHz, 1.125 inch diameter Harisonic (model I80118T) immersion transducer, a sample reflected signal, taken at an angle of incidence of 30°, and the resulting Fourier transform showing the minimum for an AS4/3501-6, [0/90]S composite are shown in Figure 5.9. The resulting dispersion curve for this sample is shown in Figure 5.10.

The experimental curves were determined using a 1.0 MHz transducer to solve

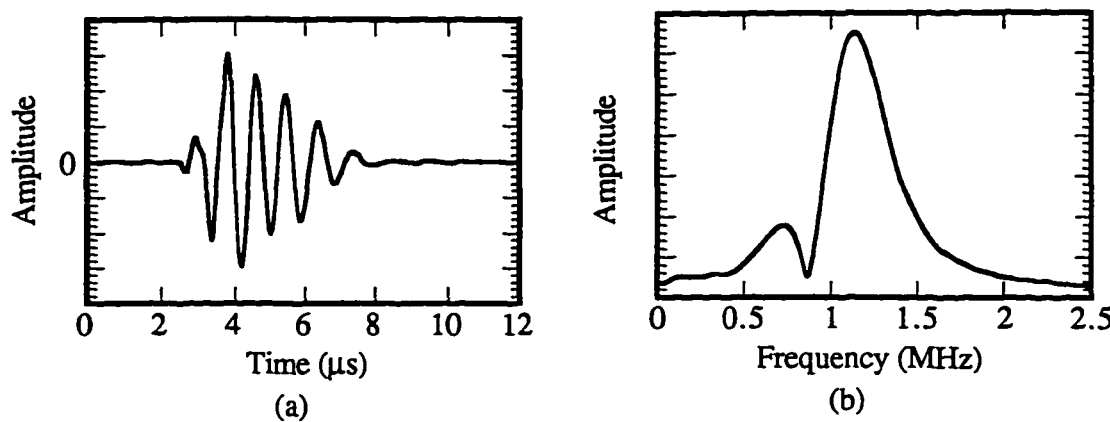


Figure 5.9 Plot of (a) the reflected signal and (b) the Fourier transform, showing a minimum.

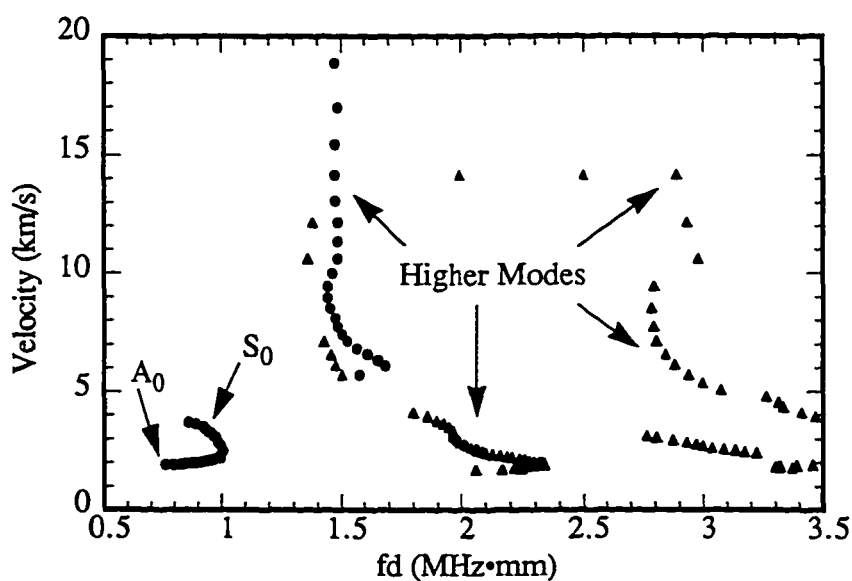


Figure 5.10 Experimentally determined dispersion curves for an AS4/3501-6, [0/90]_S composite. Circles represent values obtained using a 1.0 MHz transducer and triangles are those obtained using a 2.25 MHz transducer.

for the lower modes and a 2.25 MHz, 0.5 inch diameter Physical Acoustics Corporation (model IU2G2) transducer to obtain higher modes. The lower modes are easily identifiable, and there exist several higher order modes. For the higher modes, what appear in the figure as discontinuous or anomalous points are actually just the result of the excitation of different modes. This can be readily seen if the experimental dispersion curves are compared to the theoretical curves which were shown in Figure 4.7. A comparison between the numerical and experimental curves are shown in Figure 5.11. Although the agreement is good, discrepancies exist between the numerical and theoretical curves. This variance is most likely a result of a superposition of two modes in the experimental curves or a result of an inaccurate choice of the elastic stiffness parameters for the manufactured sample (as discussed in Sections 4.2 and 4.3).

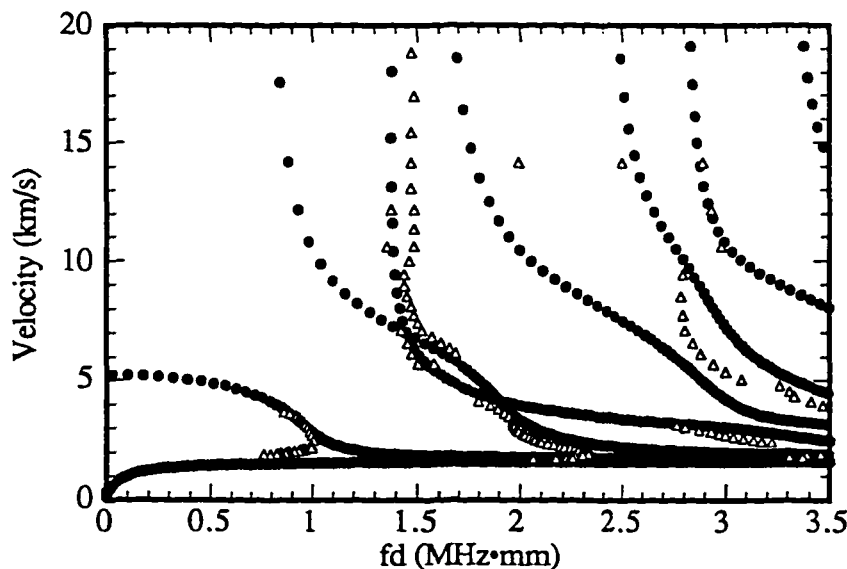


Figure 5.11 A comparison of numerical (solid circles) and experimental (open triangles) dispersion curves for an AS4/3501-6, [0/90]₃s composite.

This chapter has focused on a variety of methods available to generate, detect, and measure the velocity of Lamb waves. Since the Lamb wave velocity depends on the elastic properties of a solid, an effective method exists to monitor damage in composite materials. The next chapter makes use of the techniques mentioned here to generate and detect Lamb waves in composite materials. The velocity of the lowest order symmetric Lamb mode is monitored in order to investigate the effects of a variety of damage mechanisms in composite structures.

Chapter 6

Lamb Wave Monitoring of Damage in Composites

Lamb waves offer a promising method of evaluating damage in composite materials. As a material is damaged, the material properties are altered. Since the Lamb wave velocity is directly related to these parameters, an effective tool can be developed to monitor damage in composites by measuring the velocity of these waves. Lamb waves can propagate several tens of centimeters for most thin planar structures and thus, provide a large interrogation length across the sample.

In this work, studies have been conducted which monitor fatigue, thermal, and a combination of thermal and fatigue damage in composite samples using Lamb wave velocity measurements. Two separate fatigue studies involving crossply composites and a thermal damage study on a unidirectional composite are described in this chapter. Additionally, a study of the combined effects of thermal and mechanical damage is conducted on candidate advanced aerospace composites for use in future aircraft. The following sections detail each of these studies by describing the test samples, the experimental procedure, and the results obtained. The first two sections cover the fatigue damage studies, the third covers thermally damaged composites, and the fourth covers combined thermal and fatigue damage.

6.1 First Fatigue Damage Study

In this experiment, studies have been conducted which monitor fatigue damage in composite samples using strain gage measurements as well as Lamb wave velocity measurements. A description of the test samples is followed by the results of two different measurements of Lamb wave velocity. The first technique is a contact measurement done at a single frequency, while the second involves an immersion study of Lamb waves in which dispersion curves are obtained. The results of the Lamb wave method for monitoring fatigue damage are compared to the damage progression measured using strain gages. The final section discusses the results and conclusions.

6.1.1 Samples

The composite samples studied were AS-4/3501-6 graphite/epoxy with a stacking sequence of $[0/90_3]_S$. The theoretical dispersion curves for this composite were already calculated and are shown in Figure 4.7. Two 12 by 15 inch plates were manufactured and C-scanned prior to being cut into specimens to check for any abnormalities. The scans revealed a moderate level of porosity in the samples. The plates were then cut into 11 by 1.5 inch coupons.

Two type CEA-06-250UW-350, $\frac{1}{4}$ inch strain gages were attached to each sample: one axial and one transverse. The gages give a measurement of the deformation of the sample for a given amount of load. From the values measured for the stress (load/area), axial strain, and transverse strain, one can obtain Young's modulus and Poisson's ratio for the sample. Young's modulus is defined as

$$E = \frac{\text{Axial Stress}}{\text{Axial Strain}} \quad (6.1)$$

and Poisson's ratio is defined as

$$\nu = \frac{\text{Transverse Strain}}{\text{Axial Strain}}. \quad (6.2)$$

Taking the slope of a plot of axial stress and transverse strain versus axial strain yields Young's modulus and Poisson's ratio, respectively. A plot of each is shown in Figure 6.1 for the samples which were studied here. The data in the figure was obtained by placing the samples in a load frame and ramping the load from 0 to 720 pounds ($2000 \mu\text{in/in}$ of strain) at a rate of 0.02 in/min for a duration of 2 minutes. From the graphs, the values for the modulus and Poisson's ratio for this coupon are found to be

$$E = 5.623 \text{ MSI} = 38.779 \text{ GPa}$$

and

$$\nu = 0.0346,$$

where the modulus is typically defined in MSI (megapounds per square inch) and Poisson's ratio is a dimensionless quantity.

Before the fatiguing process, two samples were loaded quasi-statically to failure to obtain Young's modulus, Poisson's ratio, and ultimate strength. Each of these coupons was loaded from 0 to $3250 \mu\text{in/in}$ of strain and back twice. On the third run, the samples were loaded to failure. Values of modulus and Poisson's ratio were obtained

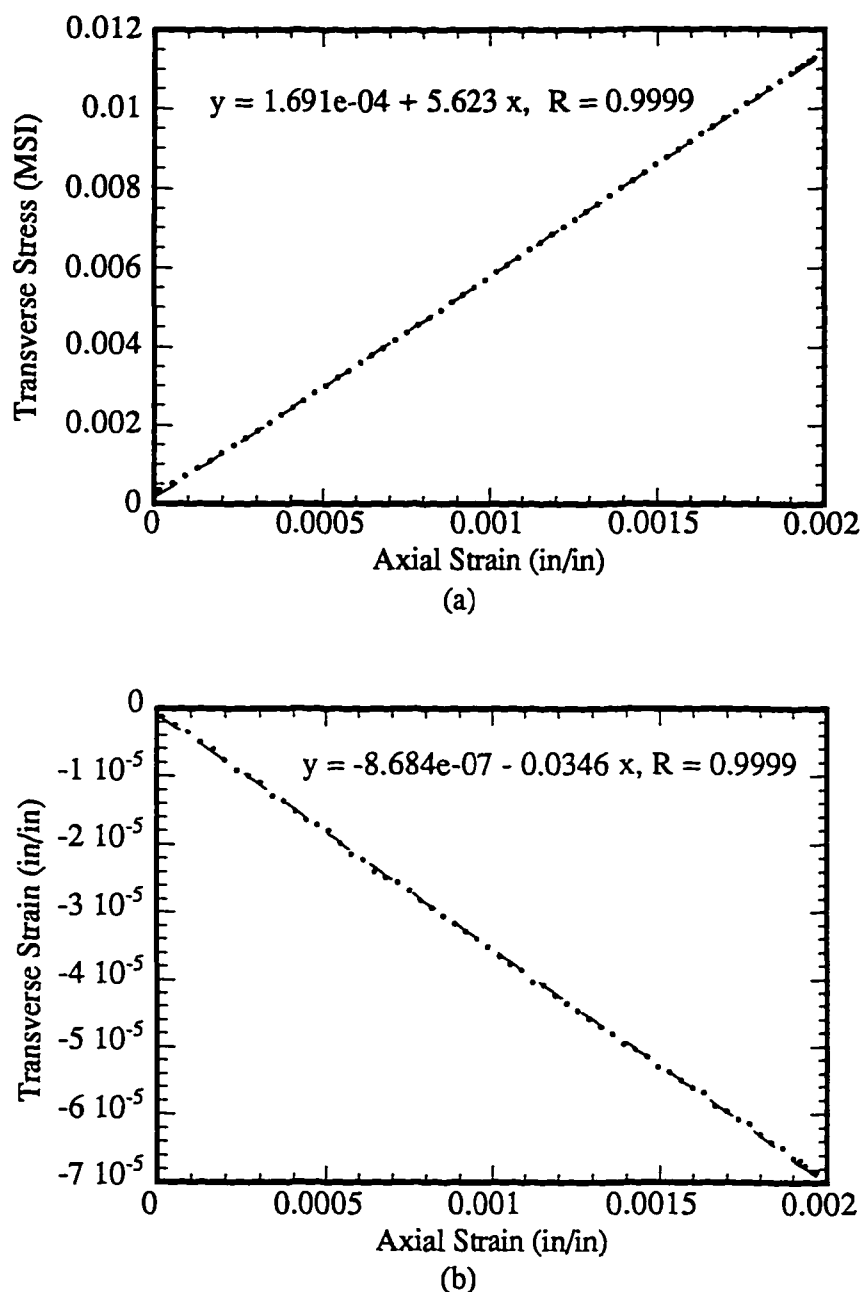


Figure 6.1 Plot of strain gage data to obtain (a) Young's modulus and (b) Poisson's ratio from the slope.

by averaging the slopes measured for each of the three load cycles described above.

The ultimate strength is defined as the load at which the samples failed. The results for the two coupons are shown in Table 6.1, where the errors listed are the standard deviations for the three measurements.

One obvious result from the data, as eluded to earlier, is the variability in the final product due to the manufacturing of the composite. The coupons, f1-1 and f2-1, were cut from two different, but identically made, larger samples. The load at failure for each sample is similar, but the modulus differs by almost 10% between the two coupons. The data obtained for these samples was used to determine the procedure for fatiguing the remaining samples. The fatiguing process is discussed in the next section.

6.1.2 Fatigue Process

The specimens have been subjected to tension-tension fatigue in an MTS model 810 (55 kip capacity) load frame. The samples were fatigued at a frequency of 10 Hz and at an R value (minimum load/maximum load) of 0.3. The upper load was taken to be 33% of the ultimate strength, which has a value of 1450 pounds (160 MPa). To demonstrate the variability of composites described above, some samples were

Table 6.1 Results for two samples loaded to failure.

Sample	E_{avg} (MSI)	v_{avg}	Load at Failure
f1-1	5.73 ± 0.01	0.027 ± 0.001	4234 lbs
f2-1	6.14 ± 0.01	0.029 ± 0.001	4226 lbs

fatigued to a terminal cycle value. To obtain results consistent across a single sample, other specimens were successively raised to higher fatigue cycle values. The velocity of the lowest order symmetric Lamb mode was measured and the modulus obtained from strain gage measurements both before and after each cyclic loading. The samples raised to successive cycle values were removed from the load frame at intermediate values of fatigue cycles in order to make the contact measurements.

6.1.3 Contact Measurement

A Lamb wave was generated by using a 2 cycle, 0.5 MHz sine wave to excite the sending transducer. The signal was received at various positions, digitized at 10 MHz on a Data Precision model DP6000 digitizer, and the waveforms saved on a PC. Both the sending and receiving transducers were Panametrics model V103 broadband longitudinal wave transducers with a nominal center frequency of 1.0 MHz and a diameter of 0.5 inches. A coupling gel was used between the transducers and the plate.

The time differences were measured by imposing a computational delay on the first signal to overlap the signals received at greater distances. The leading part of both waves is identified as the lowest order symmetric Lamb wave, which is not very dispersive. The trailing portion of the signals contains the dispersive antisymmetric wave as well as edge reflections. The distances were measured to an accuracy of 0.01 cm using a Graf/Bar sonic ranger. A least-squares fit from a plot of time and distance was performed to obtain the velocity of the prompt S_0 mode.

6.1.4 Contact Results

To examine the variability of response to fatigue, various samples, which were cut from each of the two larger plates, were loaded to terminal values. The modulus and velocity of the lowest order symmetric Lamb wave were measured both before and after fatiguing. Shown in Table 6.2 are the results of the measurements. The velocities listed in the table are the average of three measurements.

As is obvious from the table, there is a wide scatter in initial modulus measurements for the various samples. When comparisons are made across different samples, the drop in modulus as well as velocity seems to depend more on the material than the number of fatigue cycles. To show this, the data in the table is plotted in Figure 6.2.

In the plot, the velocity was normalized to the velocity measured before fatiguing. The normalized modulus was obtained in a similar manner. The velocity error bars are an estimate of the total error due to the uncertainties in the distance measurement and the digital signal overlap to obtain the time differences. Some of values for

Table 6.2 Data for various samples loaded to a terminal number of cycles.

Sample	Total Fatigue Cycles	Modulus Before (MSI)	Modulus After (MSI)	S ₀ vel. Before (km/s)	S ₀ vel. After (km/s)
f1-3	10 ⁵	5.652	5.188	5.42	5.13
f1-4	10 ⁵	5.805	5.221	5.37	5.09
f2-2	10 ³	5.884	5.540	5.48	5.20
f2-6	10 ⁶	6.204	5.883	5.44	5.37
f2-7	10 ⁴	5.625	5.215	5.33	5.05

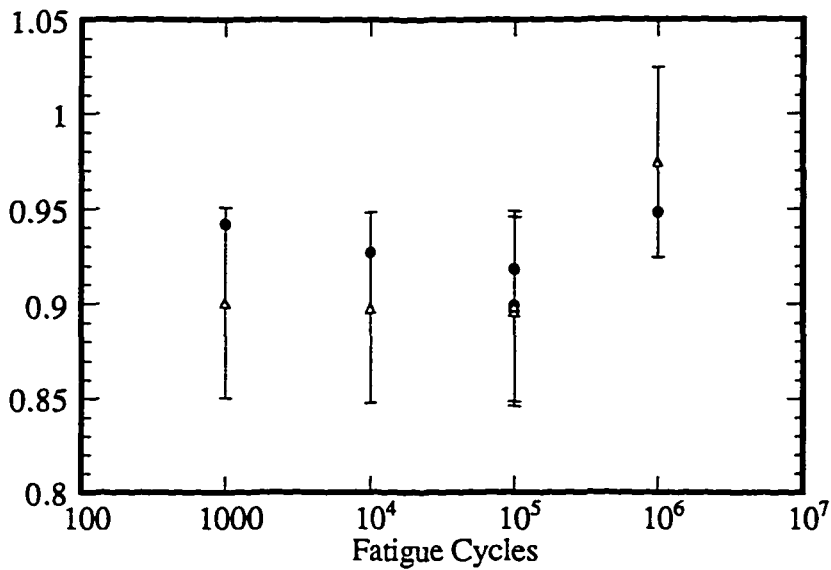


Figure 6.2 Plot of normalized modulus (solid circles) and normalized velocity squared (open triangles) versus fatigue cycles for various samples fatigued to terminal levels.

the three measurements varied as much as 8-10% from the average. Using a similar technique, Tang and Henneke, [22], have reported deviations as great as 10% from the average of three measurements as well.

The velocity of the lowest order symmetric mode depends on the square root of the modulus for isotropic plates and the square root of the in-plane stiffness values for unidirectional composites [58]. Since the modulus shown in the plot was obtained from strain gage measurements of the in-plane stiffness, the square of the velocity was chosen to plot against the number of fatigue cycles for convenience. For the case of different specimens fatigued to various terminal cycle values, the velocity squared and modulus follow the same general trend. However, the overall plot reveals no discern-

ible trend when the modulus and velocity squared are compared to the number of fatigue cycles. This result was due to the material variations across the manufactured plates, which had appreciable levels of porosity.

To examine the influence of fatigue cycles on the modulus and Lamb wave velocity and to obtain consistency, three different samples were each subjected to increasing fatigue cycles. The samples were fatigued 10^n cycles ($n = 1, 2, 3, 4, 5$, and 6). The velocity and modulus were obtained after each cyclic loading. The results are tabulated in Table 6.3. The velocities listed are the average of three measurements

As the samples underwent increasing amounts of fatigue, an increasing number of cracks in the 90° plies was observed under a microscope. These cracks degrade the modulus. Photomicrographs at different magnifications were taken of the edge of a fatigued composite and are shown in Figure 6.3. The thickness of the sample shown in the figure is 0.12 cm. For the lowest magnification, the fibers from the 0° laminas are the vertical bright streaks on the outer edges and the six 90° laminas are what appear as dots in between the outer layers. The ends of the fibers for these laminas is seen quite clearly at the higher magnification shown in Figure 6.3d.

The composite samples exhibit a decrease in the velocity as the modulus degraded due to increasing fatigue. Both the modulus and velocity follow the same general trend with increasing fatigue cycles. To show this schematically, the results for sample f1-8 are shown in Figure 6.4. As before, the velocity and modulus were normalized and the velocity error bars are an estimate of the total error due to the uncertainty in the distance and time measurements.

Table 6.3 Data from samples fatigued 10^n cycles.

Sample	Fatigue Cycles	Modulus (MSI)	Velocity (km/s)
f1-8	0	5.914	5.43
	10	5.910	5.43
	100	5.847	5.34
	1000	5.720	5.34
	10^4	5.615	5.24
	10^5	5.520	5.02
	10^6	5.447	5.04
f2-4	0	5.783	5.36
	10	5.785	5.25
	100	5.780	5.32
	1000	5.778	5.21
	10^4	5.353	5.32
	10^5	5.274	4.96
	10^6	5.321	5.21
f2-5	0	5.821	5.41
	10	5.808	5.24
	100	5.811	5.39
	1000	5.791	5.11
	10^4	5.561	5.18
	10^5	5.450	5.16
	10^6	5.240	4.94

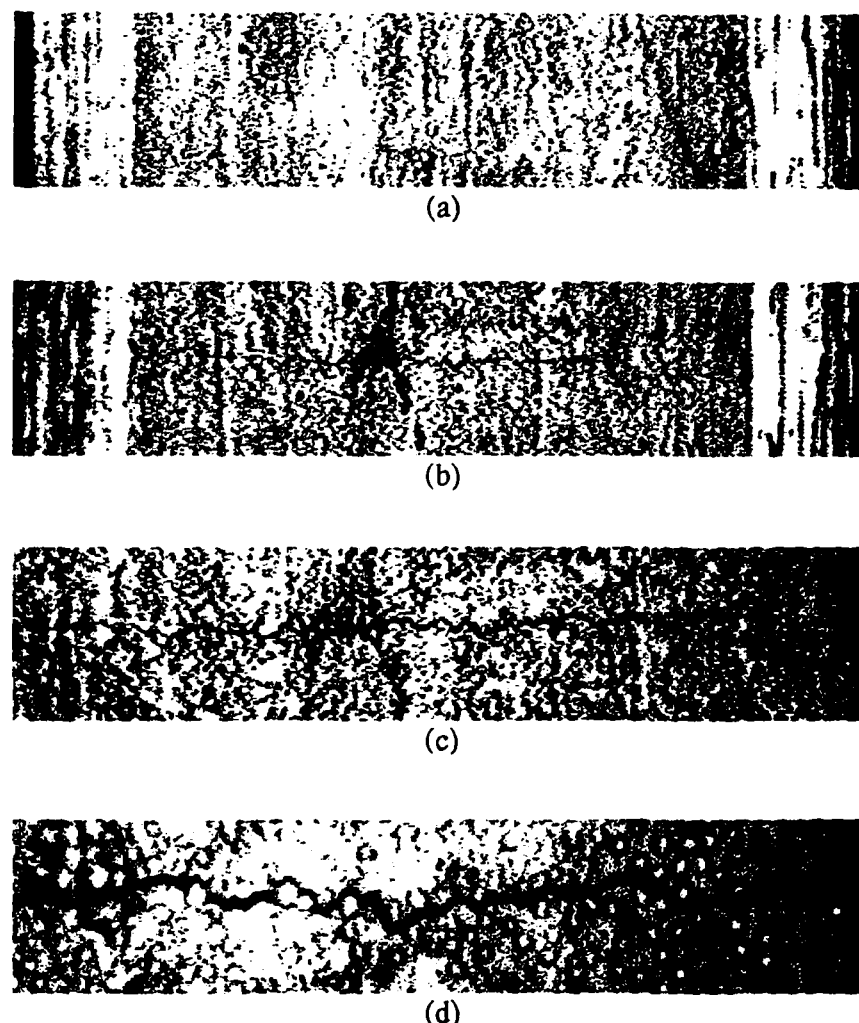


Figure 6.3 Photomicrographs of the edge of a composite sample: (a) without a crack and (b)-(d) with a transverse matrix crack. The magnification for each was: (a) 5.5, (b) 5.5, (c) 11.0, and (d) 28.0. The thickness of the sample is 0.12 cm.

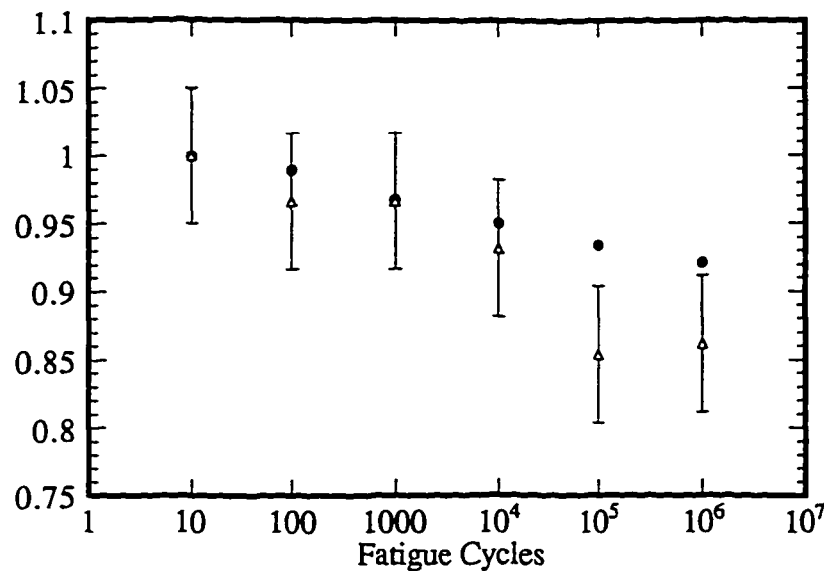


Figure 6.4 Plot of normalized modulus (solid circles) and normalized velocity squared (open triangles) versus fatigue cycles for sample f1-8.

6.1.5 Immersion Measurement

In addition to the contact measurements, which were done at a single frequency, an immersion method, detailed in Section 5.3, was used to obtain dispersion curves for three different samples: one with no load history, one sample which was loaded to a terminal value of 10^5 fatigue cycles, and a third sample that had undergone a total of one million fatigue cycles.

In this experiment, a Harisonic model I80118T immersion transducer with a nominal center frequency of 1.0 MHz and diameter of 1.125 inches was used in a pulse-echo arrangement. The specimen was rotated 0.4-60° in steps of 0.4° and the reflected waveform at each angle was saved for later analysis of the frequency content. After

determining the frequency of the minimum for each angle, the velocity (from Snell's Law) versus the frequency-thickness product was plotted to obtain the dispersion curves. The results are shown in Figures 6.5 and 6.6. The dispersion curves for the fatigued samples are clearly shifted from the undamaged sample for both the higher and lower modes. Despite the difference in number of fatigue cycles between the two samples, the shift in the dispersion curves for both is similar. However, this is to be expected because both samples show a similar drop in modulus and velocity. The sample with 10^6 cycles shows a 7.2% drop in velocity and a 7.9% drop in modulus. The sample with 10^5 cycles shows a 5.2% velocity drop and a decrease in modulus of 10.1%. Since the contact measurements were conducted at a lower frequency and the velocity of the S_0 mode monitored, this region of the dispersion curves will be examined more carefully. For reference, since both curves are very similar, the lower two modes in Figure 6.6 are shown in Figure 6.7.

6.1.6 Immersion Results

The dispersion curves for the two lowest order modes are significantly separated for the two samples (Figure 6.7). The curves have roughly a 7% difference in velocity for the symmetric mode. This is in good agreement with the contact result for the same sample, which had a 7.2% relative decrease in velocity after one million fatigue cycles.

It is also noted in the figure that the A_0 mode velocity variation is much less than that of the S_0 mode. This can be understood by examining how the velocity relates to the modulus. The velocity changes as the square root of the stiffness for the symmetric

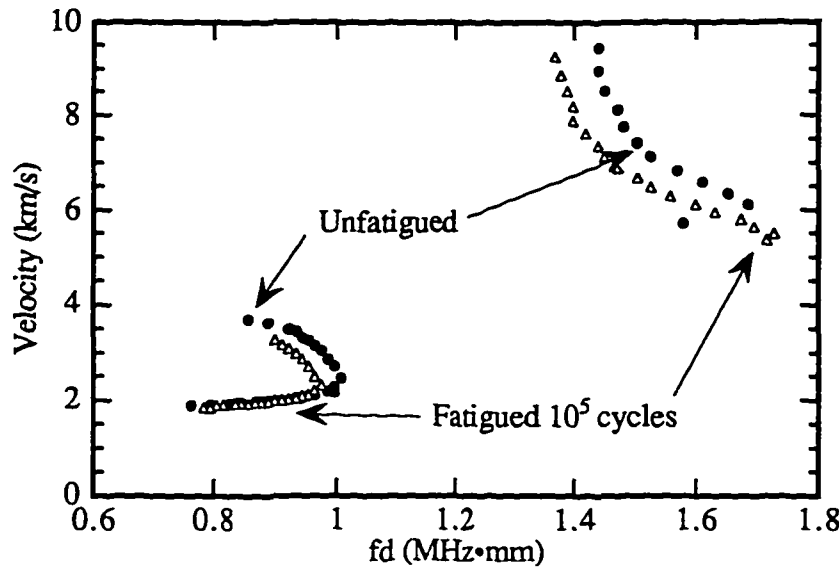


Figure 6.5 Experimental dispersion curves for a sample which is undamaged (solid circles) and one which has been fatigued 10^5 cycles (open triangles).

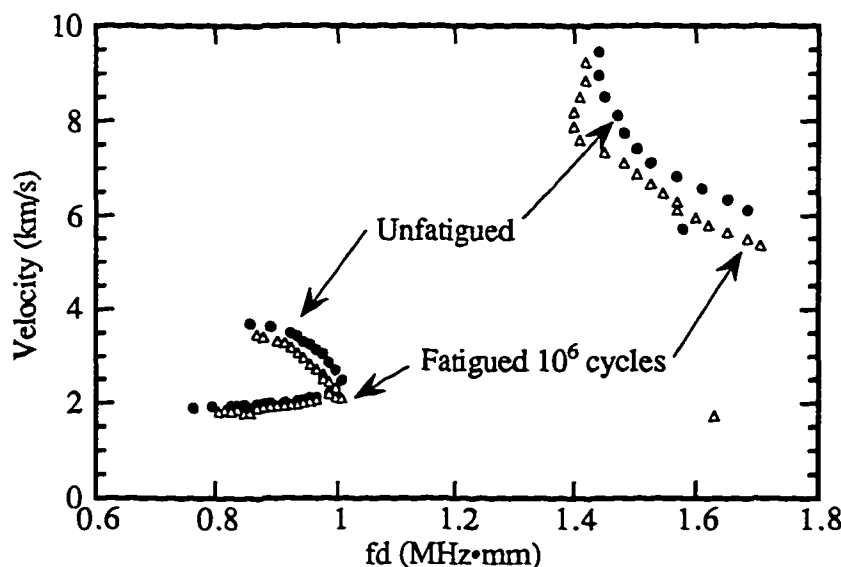


Figure 6.6 Experimental dispersion curves for a sample which is undamaged (solid circles) and one which has been fatigued 10^6 cycles (open triangles).

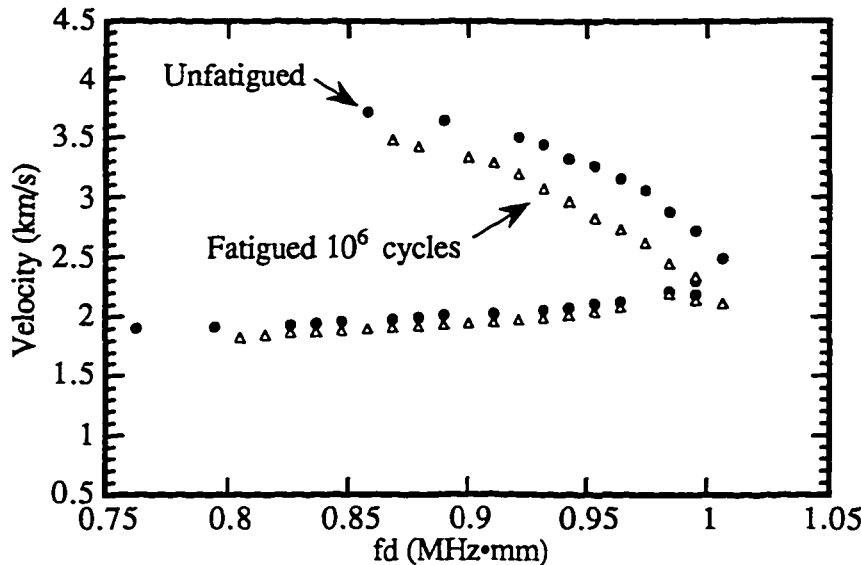


Figure 6.7 Plot of the lower two modes of the dispersion curve shown in Figure 6.6.

mode, but as the fourth root of the stiffness for the antisymmetric mode [58]. Therefore, the A_0 mode velocity will change less than the S_0 mode velocity for a given decrease in modulus.

For an undamaged composite, the numerical and experimental dispersion curves were already shown to be in good agreement (Figure 5.11). It was also discussed, and shown in Figure 4.10d, that, for propagation perpendicular to the fibers, a decrease in the parameter c_{33} alters the dispersion curves. This is due to the fact that c_{33} is the modulus across the fibers. The transverse matrix cracks (due to fatigue damage) should, therefore, lead to a decrease in the elastic stiffness constant c_{33} .

To examine the effect of the matrix cracks in the 90° laminas, numerical dispersion curves were calculated in which the value of c_{33} was reduced by 5% in only these

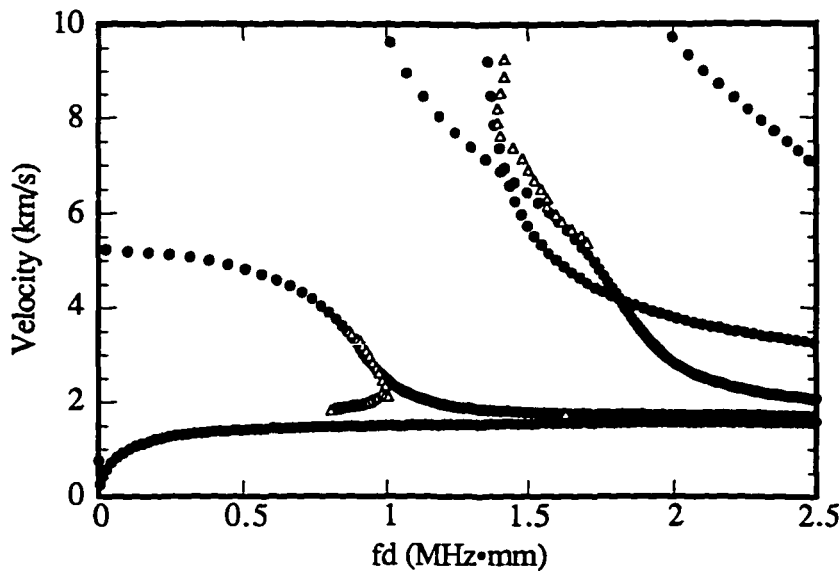


Figure 6.8 Comparison of numerical dispersion curve with c_{33} reduced by 5% in the 90° layers (solid circles) and experimental curve for a one million cycle fatigue sample with transverse matrix cracks (open triangles).

layers. The model was then compared to the sample which had undergone 1 million cycles of fatigue damage. The results compare well and are shown in Figure 6.8.

Finally, a comparison is done for the numerical dispersion curves for the lower modes. The curves for the lower modes calculated using the full elastic parameters and those calculated using c_{33} reduced by 5% in the 90° layers are shown in Figure 6.9. When compared in the region where the experimental data was obtained ($0.75 \leq fd \leq 1.05$ MHz·mm), the numerical results are in good agreement with the experimental dispersion curves shown in Figure 6.7. For the theoretical curves in this region, the S_0 velocity shows roughly a 7% decrease and the A_0 mode variation is much less than the S_0 velocity change. These are exactly the characteristics which were observed in the experimental curves (Figure 6.7).

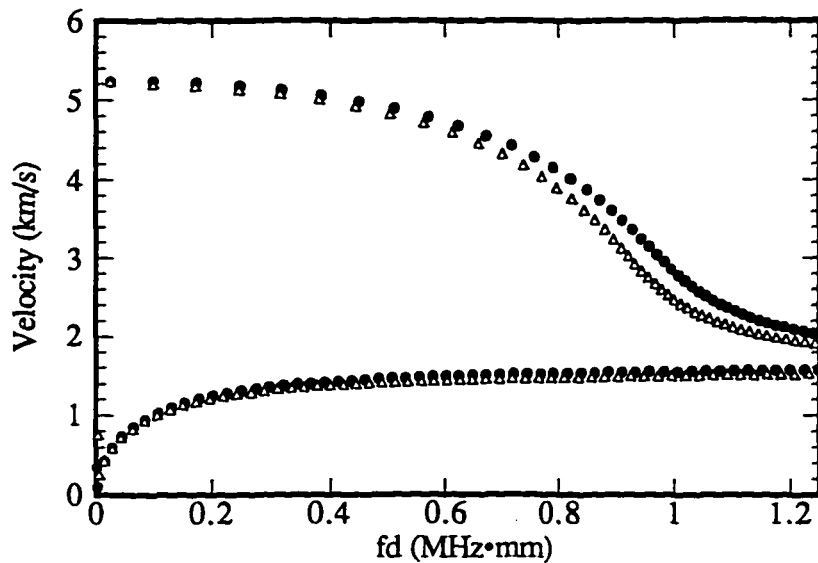


Figure 6.9 Comparison of lower modes of numerical curves using full parameters (solid circles) and with c_{33} reduced by 5% (open triangles).

6.1.7 Discussion

Presented above are the results of two techniques for determining the Lamb wave velocity in composites. The results of the contact measurement show that the change in modulus, as measured using strain gages, and the change in velocity squared follow the same general trend. A change in velocity due to the modulus degradation was also seen in the results of the immersion measurement. The theoretical curves generated using a reduced value of c_{33} in the 90° layers also compared very well to the experimental data for samples which exhibited transverse matrix cracking. Thus, the model can be effectively used to predict damage due to fatigue.

The Lamb wave velocity measurements in this study were conducted at long wavelengths. This was done for several reasons. First, if the wavelength is large compared to the diameter of the fibers, the composite can be treated as homogeneous. Second, only the lowest order modes propagate in the frequency range where the contact measurements were conducted. Finally, global information about the effective elastic properties of the material can be obtained using long wavelengths.

It has been noted by other Charewicz and Daniel [7] that strain gages only measure a local change in modulus and do not measure a global change in the specimen. Since the strain gages used in this study had a gauge length of $\frac{1}{4}$ inch, they may not give an accurate account of damage throughout the entire plate. This would be especially true at the lower fatigue levels where very few cracks were observed in the samples. As the samples were damaged further, the cracking became more uniform. Thus, a Lamb wave technique at low frequencies used to track the modulus as a function of fatigue history may provide improved global interrogation over the propagation length of the wave.

6.2 Second Fatigue Damage Study

Due to the high levels of porosity in the previous coupons, additional composite samples of the same material, AS4/3501-6, and same architecture, $[0/90_3]_S$, were obtained. Also, the new composites were loaded to greater levels in order to induce damage more quickly in the samples. This section describes the details and results of this fatigue study.

6.2.1 Samples

Two composite plates identical to those used in the previous study were obtained. The new composite plates were C-scanned prior to cutting them into coupons to check for porosity. The images were very uniform and, therefore, no large scale areas of porosity were expected. The plates were then cut into 18 1.5 by 11 inch coupons. The edges were then polished and photomicrographs were taken. Again, no appreciable amounts of porosity were found.

Again, as before, several samples were loaded quasi-statically to failure to obtain Young's modulus, Poisson's ratio, and ultimate strength. This time for coupons, two from each plate, were broken. The results for the four coupons are shown in Table 6.4. As seen previously, there are inconsistent results in the final product due to the manufacturing of the composite. This variability is seen across the same plate, as well as between plates. The coupons jm1-1 and jm1-9 were cut from the same larger plate and the coupons jm2-1 and jm2-9 from a different, but identical, sample. The modulus between the two extreme values in the table differs by over 5%. The load at failure for

Table 6.4 Results from four samples loaded to failure.

Sample	E_{avg} (MSI)	ν_{avg}	Load at Failure
jm1-1	5.971	0.033	4850 lbs.
jm1-9	6.064	0.030	4452 lbs.
jm2-1	6.343	0.035	4626 lbs.
jm2-9	6.198	0.034	4509 lbs.

each sample varies quite a bit as well. As before, the data obtained for these samples was used to determine the procedure for fatiguing, which is discussed in the next section.

6.2.2 Fatigue Process

Similar to the first study, the specimens have been subjected to tension-tension fatigue in an MTS model 810 (55 kip capacity) load frame. The samples were fatigued at a frequency of 10 Hz and at an R value of 0.35. For this study, however, the upper load was taken to be 45% of the ultimate strength, which has a value of 2070 pounds (200 MPa). The samples were fatigued for a range of 10^n cycles ($n = 3, 4$, and 5). Again, the samples were removed from the load frame at intermediate values of fatigue cycles and the velocity of the lowest order symmetric Lamb mode was measured. In addition to loading these samples at higher levels, the crack density was also monitored during the process.

6.2.3 Velocity and Crack Density Measurements

A Lamb wave was generated by using a 6 cycle, 0.5 MHz sine wave to excite a Harisonic model CM-00080S longitudinal wave transducer with a nominal center frequency of 0.5 MHz and a diameter of 0.5 inches. The signal was received at various positions by an array of pinducers (Valpey-Fisher model VP-1093) with active elements of 0.135 cm. The pinducers were placed in a holder at a fixed separation dis-

tance of 1.0 cm between each transducer. As was discussed in Section 5.2.1, this receiving arrangement greatly reduces the error in the measurement of the velocity due to the uncertainty in the distance between the transducers. Since a differential measurement is being made, fixing the transducers in a holder virtually eliminates the distance error. As before, a coupling gel was used between the transducers and the plate.

A commercial MacScope NuBus board, which allows the computer to act as an 8-bit digitizer, was used in a Macintosh IIx computer to acquire the signals. The software used was a LabView VI (Virtual Instrument) which was provided with the MacScope board. The signals were digitized at 10 MHz, averaged, and the waveforms saved to the computer.

In an effort to reduce the error in the time measurement, the time differences between the pinducers were measured by performing a cross-correlation, described in Section 5.2.2. The leading part of both waves, which is identified as the lowest order symmetric Lamb wave, was used in the correlation. The distances between the five pinducers in the array were held fixed at 1, 2, 3, and 4 cm, respectively. The velocity of the prompt S_0 mode was obtained by a least-squares fit from a plot of time and distance.

To measure the crack density, a 2.5 cm section in the middle of the plate was marked. This was done in order to count the number of cracks occurring in the same 2.5 cm length in the sample. Keeping the same measurement area is especially important at the lower cycle levels where the cracking is not very uniform. The number of cracks was counted by examining the edges of the coupons under a microscope. The velocity measurements described above were centered over the same region where the crack density was monitored.

6.2.4 Results

The influence of fatigue cycles on transverse matrix cracking and Lamb wave velocity was examined. Five different samples were each subjected to increasing fatigue values of 10^n cycles for $n = 3, 4$, and 5 . The velocity and crack density were obtained after each cyclic loading. The results are tabulated in Table 6.5. Each velocity listed is the average of three measurements. The standard deviation for all of the samples was less than 5% from the average of the three measurements and most were within 2.5% of the average. Thus, the accuracy of the measurements is quite good and provides an improvement over the technique used in the first fatigue study. Also, these results are similar to those obtained by Tang and Henneke, [22], who report a variation of 1.5% using a similar technique.

As the samples underwent increasing amounts of fatigue, an increase in the crack density in the 90° laminas was observed under a microscope. These cracks degrade the modulus and thus, a decrease in the velocity is observed with increasing fatigue cycles. To show this schematically, the crack density and normalized velocity squared are shown as a function of fatigue cycles in Figures 6.10 and 6.11, respectively. The velocity was normalized in a similar manner as described in the previous study. Since the uncertainty in the distance and time measurements in this study is less than that of the previous study, the velocity error bars are not as large as were previously shown in Figures 6.2 and 6.4. The error bars in the plot of the crack density assume a ± 1 error in the total number cracks counted in the 2.5 cm length.

As expected, the crack density for these samples increased with increasing cycles

Table 6.5 Data for fatigue samples.

Sample	Fatigue Cycles	Crack Density (cracks/mm)	Velocity (km/s)
jm1-3	0	0	4.49
	10^4	0.560	4.23
	10^5	0.640	4.26
jm1-4	0	0	4.54
	1000	0.240	4.55
	10^4	0.360	4.22
	10^5	0.480	4.23
jm1-5	0	0	4.40
	10^4	0.560	4.03
	10^5	0.720	4.14
jm1-6	0	0	4.41
	1000	0.200	4.41
	10^4	0.400	4.27
	10^5	0.520	4.22
jm1-7	0	0	4.56
	1000	0.240	4.38
	10^4	0.480	4.37
	10^5	0.760	4.14

and, as with the previous study, the velocity squared decreased with fatigue cycles.

Since strain gages were not used on these samples, the decrease in modulus will be estimated from the crack density. An expression which relates reduced modulus to crack density is given in Caslini, et al. [69]. For a $[0_m/90_n]_S$ laminate, the stiffness loss is given by [69]

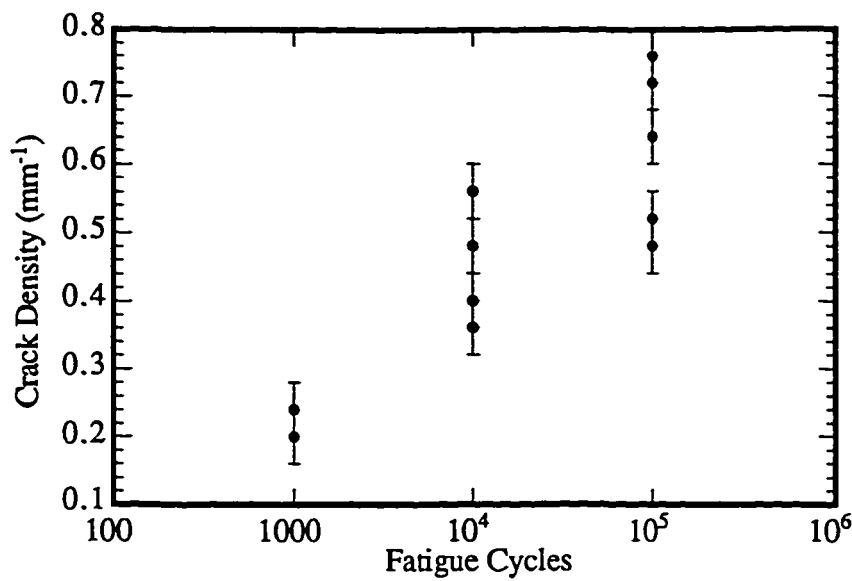


Figure 6.10 Crack density versus fatigue cycles for all samples listed in Table 6.5.

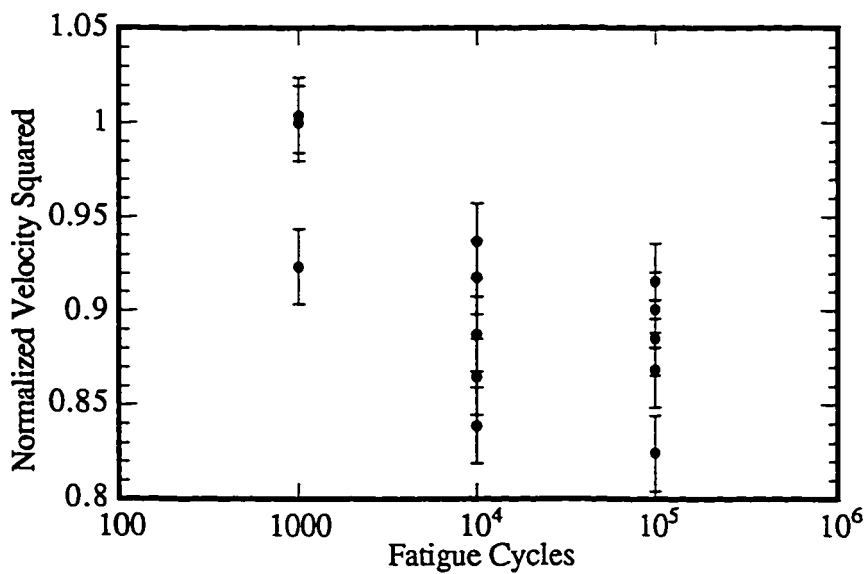


Figure 6.11 Normalized velocity squared versus fatigue cycles for all samples listed in Table 6.5.

$$\frac{E}{E_0} = \frac{1}{1 + \frac{nE_2}{mE_1} \frac{\tanh(\lambda/2D)}{(\lambda/2D)}}, \quad (6.3)$$

where

$$\lambda^2 = \frac{3G_{12}E_0(n+m)}{h^2E_1E_2n^2m}. \quad (6.4)$$

In the above equations, E and E_0 are the values of the modulus for the damaged and undamaged laminate, respectively. E_1 , E_2 , and G_{12} are the moduli (longitudinal, transverse, and shear, respectively) for each individual unidirectional lamina in the plate. D is the crack density, h is the lamina thickness, and m and n are the number of 0° and 90° layers, respectively, in the half-thickness of the plate.

For the case presented here, $m = 1$, $n = 3$, and $h = 0.15$ cm. The value for the undamaged modulus, E_0 , is obtained from the average of the four modulus measurements (Table 6.4) for the samples which were loaded to failure. The engineering constants for AS4/3501-6, are taken to be [2]

$$E_1 = 20.6, \quad E_2 = 1.50, \quad G_{12} = 1.04,$$

where all values are listed in MSI. A discussion of the relationship between the engineering constants and the elastic stiffness constants (c_{IJ}) can be found in Appendix A.

The reduced stiffness as a function of crack density is calculated from the parameters given above using equations (6.3) and (6.4). Figure 6.12 shows a comparison of the calculated reduced stiffness and the normalized velocity squared listed in Table 6.5. The figure shows a larger decrease for the normalized velocity squared than for

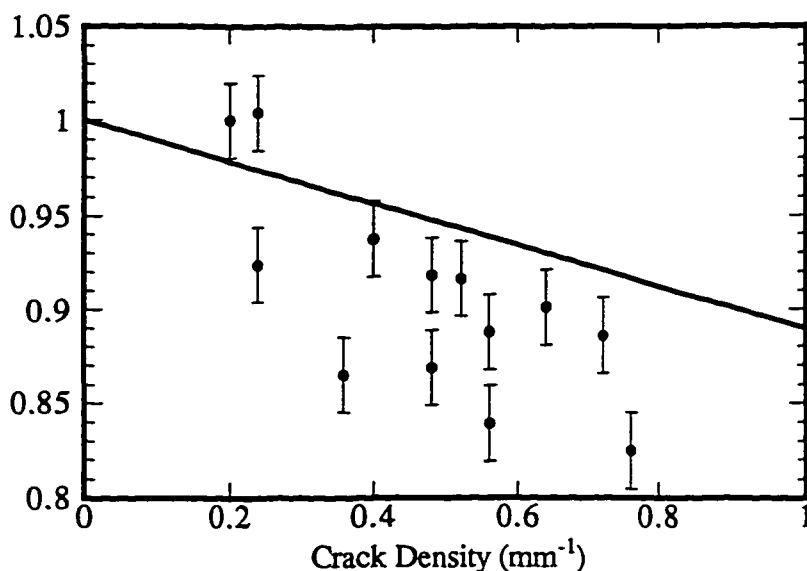


Figure 6.12 Calculated normalized modulus (solid line) versus normalized velocity squared (solid circles) as a function of crack density.

the normalized modulus which was calculated from the crack density. Though not as pronounced as the results shown in Figure 6.12, this behavior was evident in the previous study when the modulus was measured using strain gages (see Figure 6.4). To see this effect for all of the samples examined in the previous study, the normalized modulus and normalized velocity squared for the data in Tables 6.2 and 6.3 are plotted in Figure 6.13.

In the figure, the error bars have been removed from the velocity measurements for clarity. The solid and dashed lines represent the curve fits for the normalized modulus and normalized velocity squared, respectively. As can be seen from the curve fits, the normalized velocity reduction is greater than the loss of stiffness for the initial fatigue study. This is in agreement with the results obtained in the present fatigue study.

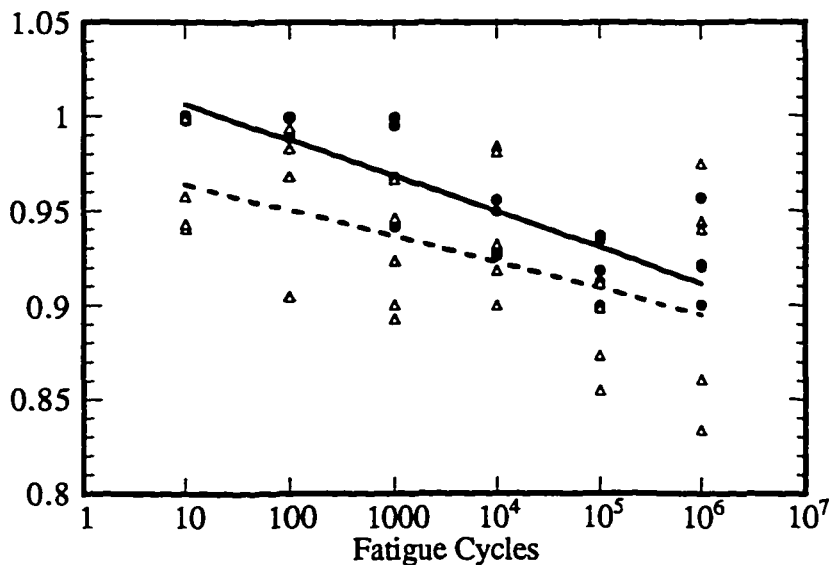


Figure 6.13 Plot of normalized modulus (solid circles) and normalized velocity squared (open triangles) for all data obtained in previous fatigue study.

These results are also in agreement with those found by Dayal, et al. [23], who examined the modulus degradation of an AS4/3502, [0/90₃]_S composite using velocity measurement of the lowest order symmetric Lamb mode. The architecture and the fibers (AS4) of the samples used by Dayal, et al. [23] are identical to the ones studied here. The epoxy matrix used (3502) is slightly different than the one used here, but the material properties of the two samples are very close. The properties for AS4/3501-6 and AS4/3502 can be found in Tables 4.1 and 4.2, respectively.

Similar to the measurements done here, the tests by Dayal, et al. [23] were also done at a frequency of 0.5 MHz. The velocity of the S₀ mode, measured using a different technique, and the crack density, measured using edge replication, were monitored as the samples underwent increasing damage. The modulus was calculated directly

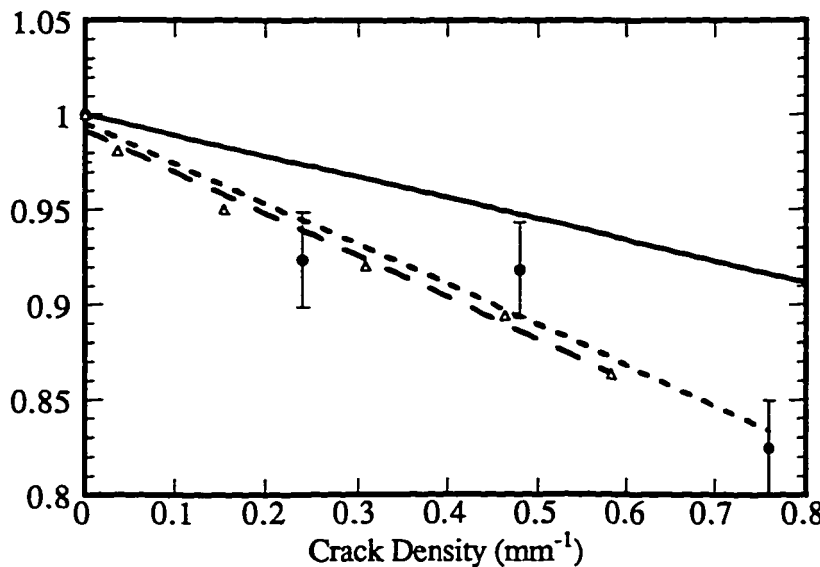


Figure 6.14 A plot of the normalized velocity squared for sample jm1-7 (solid circles) versus data from Dayal, et al. [23] (open triangles). Curve fits are shown for the data in this study (short dashes) and for the data of Dayal, et al. [23] (long dashes). The solid line is the theoretical modulus reduction described earlier.

from the velocity measurement using the relation $E = \rho v^2$ [23], where E is the modulus, ρ is the density, and v is the velocity of the S_0 Lamb mode. Given this relation, the normalized modulus will also be equal to the normalized velocity squared. The results from Dayal, et al. [23] are presented, along with the results for a representative sample (jm1-7) from this study, in Figure 6.14.

In the figure, the solid line represents the theoretical reduced modulus previously calculated using the material parameters for AS4/3501-6. However, as mentioned earlier, the parameters for this type of composite are extremely close to those of AS4/3502. Therefore, the theoretical curve shown in the figure is representative of the composites used in both studies. Another interesting feature in the figure involves the comparison of the two velocity measurements. Both sets of data show a larger decrease in normal-

ized velocity squared than what is theoretically predicted for the modulus reduction.

Dayal, et al. [23] reported similar results when the modulus reduction measured using the Lamb wave technique was compared with the results of analytical modeling and static stiffness measurements conducted by other authors. Thus, the Lamb wave velocity technique may provide a more sensitive method of damage detection than modulus reduction measurements.

6.2.5 Discussion

Presented above are the results of a different technique than that which was used in the previous study for determining the Lamb wave velocity in composites. Due to a reduction in the uncertainty in the distance and time measurements, the velocity measurements were found to be more accurate using this technique than those found in the first study. The crack density was also monitored as a function of fatigue cycles, which was not done previously. A decrease in normalized velocity squared with increasing fatigue cycles was noted. This was expected and agrees with the results presented in the initial study.

The main difference between this study and the initial fatigue study was the monitoring of the crack density with fatigue cycles. The density was shown to increase with an increasing number of cycles, as is to be expected. The Lamb wave velocity, when plotted against crack density, exhibited a decrease with increasing crack density. This drop in velocity as a function of crack density was compared with the results of Dayal, et al. [21], who saw a similar velocity decrease.

As was mentioned in Section 6.1.7, strain gages only measure a local change in modulus and do not measure a global change in the specimen. The strain gages used in the previous study had a gauge length of $\frac{1}{4}$ inch and therefore, may not have given an accurate account of damage throughout the entire plate. It was shown in Caslini, et al. [69] that the crack density can be theoretically related to stiffness reduction. Since the crack density was monitored over a 2.5 cm length, this becomes the effective gage length for measuring the modulus reduction via the crack density.

The modulus reduction, calculated from the crack density, was compared to the results obtained using the Lamb wave velocity measurements. A more dramatic decrease was observed in the velocity measurements than in the theoretical modulus reduction. Thus, a Lamb wave technique used at low frequencies to track damage as a function of fatigue history may be more sensitive and provide an improved method of interrogation over the techniques which only measure modulus degradation.

6.3 Thermal Damage

Determining the response of composites to thermal damage is necessary for a complete understanding of the total use environment of these materials. The objective of the research presented in this section is to provide a method of quantifying the amount of thermal damage in composite materials. Components which have non-visible damage, but have degraded performance on the order of several percent, are of interest. At this level of damage the safety margin designed into the structure may be compromised.

Thermal damage of these structures can occur in different scenarios. The first is damage caused during repair operations of an aircraft component. A thermal cure cycle, similar to the method used to repair cracks on B-1 bombers (described in Section 2.4.3), is used to effect repairs using thermoset or thermoplastic polymers, and the heater blanket may undergo an undocumented or unintentional over temperature excursion leading to a loss of integrity. Second is damage that is incurred in a composite in a heat affected zone of an aircraft, such as near engine exhausts or leading edges. A third is a fire either on board the aircraft or in the immediate vicinity of a parked aircraft.

6.3.1 Samples

The heat damaged samples, which simulate typical thermal damage on carbon/epoxy aircraft structures, were provided by McDonnell Douglas Aerospace. These 6 by 6 inch samples were fabricated as 16 ply, uniaxial plates of AS4/977-3. All samples had received different levels of heat damage, had been C-scanned, and had Barcol hardness readings performed. The exposure temperatures ranged from 550°F to 1000°F for a duration of 3 minutes and included a sample which was exposed to 600°F for 10 minutes.

6.3.2 Velocity Measurement

In these studies Lamb waves were generated by using a 5 cycle, 0.5 MHz sine wave to excite the sending transducer. The transmitting transducer (Panametrics model

V103) was a broadband longitudinal wave transducer with a nominal center frequency of 1.0 MHz and a diameter of 0.5 inches. The receiving transducers were of the previously described pinducer type, which were fixed in a holder with separations of 4, 5, 6, and 7 cm. The signal was received at various positions and digitized at 10 MHz on a Data Precision model DP6000 digitizer. The time differences were measured by imposing a computational delay on the first signal to overlap the signals received at greater distances. A least-squares fit from a plot of time and distance was performed to obtain the velocity of the prompt S_0 mode. A coupling gel was used between the transducers and the plate.

6.3.3 Results

The velocity of the lowest order symmetric Lamb mode was measured in the fiber direction for ten different thermally damaged samples. Table 6.6 shows the phase velocity of the S_0 mode, the exposure temperature, and duration for the set of specimens. Besides the control, sample 1811, all of the samples were exposed for a 3 minute duration, with one exception, sample 1813, which saw a 10 minute duration at 600°F.

The data listed in Table 6.6 is plotted in Figure 6.15. The error bars are an estimate in the velocity error, mainly due to uncertainty in the digital channel alignment, and are quite liberal. The decrease in velocity with increasing thermal damage is quite dramatic. The variation in velocity is on the order of 18% for the two extremes of temperature exposure. The correlation with extended temperatures is excellent and pro-

Table 6.6 Data for the thermally damaged samples.

Sample	Duration (minutes)	Exposure Temperature (°F)	Velocity (km/s)
1802	3	1000	7.57
1803	3	800	8.26
1804	3	700	8.92
1805	3	650	8.77
1806	3	600	9.12
1807	3	750	8.03
1809	3	575	8.66
1810	3	550	9.12
1811	0	0	8.88
1813	10	600	8.65

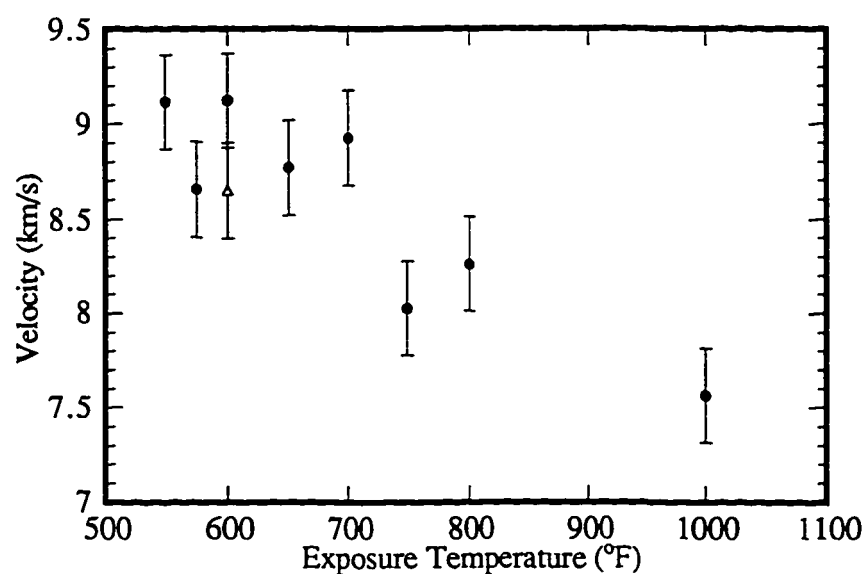
**Figure 6.15** Plot of S_0 velocity for a range of samples exposed to different temperatures for durations of 3 minutes (solid circles) and 10 minutes (open triangles).

Table 6.7 Engineering constants[†] and associated elastic stiffness parameters.

Engineering Constant	Value (GPa)	Elastic Stiffness Constant	Value (GPa)
E_1	133.1	c_{11}	135.0
E_2	8.76	c_{13}	3.20
G_{12}	5.03	c_{33}	9.09
v_{12}	0.30	c_{23}	1.59
c_{44} (see text)	3.75	c_{55}	5.03

[†]Provided by McDonnell Douglas

vides a method to assess thermal damage. Although the velocity showed a large change with thermal damage, the Barcol hardness numbers provided by McDonnell Douglas showed little variation over this temperature range. Therefore, measurement of the Lamb wave velocity could provide a better technique to assess thermal damage than conventional methods.

A model calculation to determine the dispersion curves for this material system was computed using material parameters in Table 6.7, which includes not only the engineering constants supplied by McDonnell Douglas, but the corresponding elastic stiffness constants. The engineering values can be used to calculate the elastic constants using various techniques [2]. A further discussion of the relationship between the elastic stiffness constants and engineering parameters is presented in Appendix A.

Since a value for G_{23} was not available, the value of c_{44} (where $c_{44} = (c_{22} - c_{23})/2$) must be estimated using common values for polymer matrix/graphite fiber composites

[70]. The value of c_{44} typically ranges from 3.5-4.0 GPa, so a median value of 3.75 GPa was chosen for the calculation. The density of the material was taken to be 1560 kg/m³. A 5 layer model calculation of the dispersion curves in the fiber direction is shown in Figure 6.16.

From the dispersion curve, one can see that the S_0 mode is almost completely non-dispersive for the lower frequency-thickness products. Also, the S_0 velocity in this region is around 9 km/s, which is exactly the velocity that was measured for the samples with little or no damage (see Table 6.6). Thus, the model compares well with the experimentally determined velocity.

Theoretical dispersion curves were also calculated for AS4/977-3 using reduced stiffness constants. The effect of reducing different c_{IJ} 's by 20% on the low frequency, non-dispersive region of the lowest order symmetric mode ($0.0 \leq fd \leq 1.0$ MHz·mm)

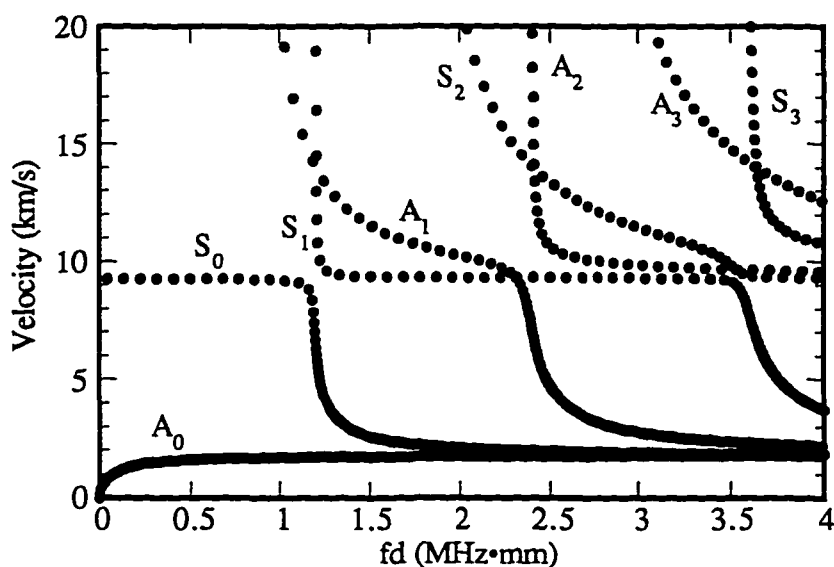


Figure 6.16 Theoretical dispersion curves for an AS4/977-3 unidirectional composite.

was investigated. The only parameter which alters the velocity of the S_0 mode in this region for propagation along the fibers is c_{II} (see Figure 4.9).

Figure 6.17 shows a plot of the experimentally determined normalized velocity versus exposure temperature, where the normalized velocity is the velocity in the damaged sample divided by the velocity in an undamaged control sample. Also plotted is the normalized velocity of the S_0 mode with reduced values of c_{II} . Here, the normalized velocity is the velocity with c_{II} reduced divided by the velocity with the full values of the elastic stiffness constants. Both velocities were taken at a constant frequency-thickness product of 0.5 MHz-mm on the dispersion curve.

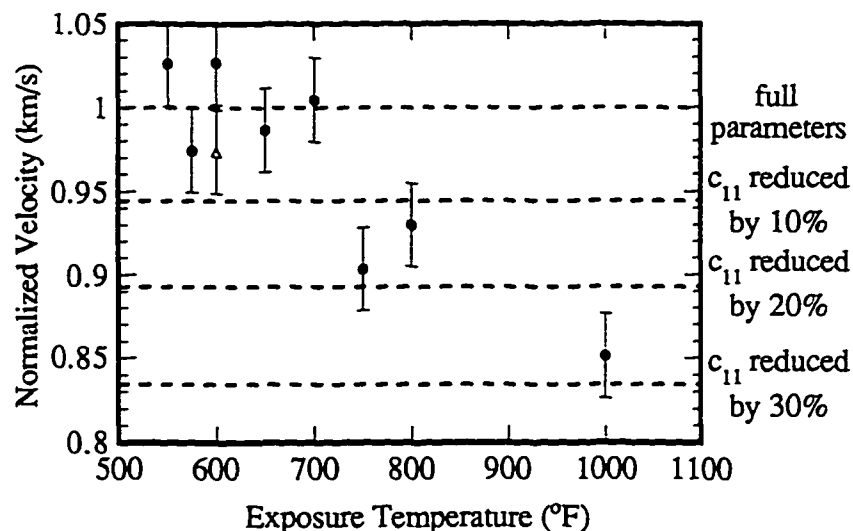


Figure 6.17 Plot of the normalized S_0 velocity of samples exposed to different temperatures. The duration times are 3 minutes (solid circles) and 10 minutes (open triangle). Also shown (dashed lines) is the theoretically determined normalized S_0 velocity with reduced values of c_{II} , as described in the text.

6.3.4 Discussion

Presented above are the results of Lamb wave velocity measurements in thermally damaged composites. The results of the experimental measurement show that the velocity of the lowest order symmetric Lamb mode dropped significantly for extended thermal damage. Theoretical calculations with reduced values of c_{11} show that a 25-30% reduction in this parameter lowered velocities of the S_0 mode by 15%. This value corresponds to the velocity reduction of the sample which saw an exposure temperature of 1000°F. Barcol hardness tests reported by McDonnell Douglas did not show a significant change for the samples studied.

The Lamb wave velocity is a quantitative measurement and can be used to verify the integrity of a composite structure over the service life of the component. This is an important measurement for flight qualified composite hardware that may have undergone some measure of thermal damage. Since the Lamb wave velocity depends on the material properties, an ideal technique can be developed to monitor composites as damage is incurred. Finally, because Lamb waves can propagate a long distance, global information about the integrity of the material can be obtained.

6.4 Combined Thermal and Mechanical Damage

The Lamb wave technique has been shown to be an effective means of interrogating fatigue damage (Sections 6.1 and 6.2) as well as thermal damage (Section 6.3) in composite materials. Future advanced aerospace composite materials, however, will be required to respond well to combined thermal and mechanical loading. Therefore, it is

of interest to investigate the feasibility of the Lamb wave technique in the detection of thermal-mechanical fatigue.

Arrangements were made to monitor candidate composite materials being examined under the High-Speed Research (HSR) program at NASA Langley Research Center in Hampton, Virginia. Duration tests are currently being conducted on specimens which are being cycled both thermally and mechanically through various flight profiles. Since it is not well understood how to accelerate the aging process for a composite material, the samples will be run between 5,000 and 60,000 real flight hours. Thus, the final tests are not scheduled for completion until after the turn of the century.

This study will investigate the use of the Lamb wave technique to monitor the early stages of thermal-mechanical fatigue in the candidate specimens. Lamb wave velocity measurements have been taken at various stages throughout the fatigue process. However, given the fact that not many hours have been accrued, much of the data involves only baseline measurements on undamaged samples. Also, only one or two velocity measurement have been made on other samples which have been cycled due to the fact that the duration tests are only in their early stages. Data from these experiments will help determine the viability of using Lamb waves to monitor thermal-mechanical fatigue damage in aerospace structures of today, as well as those of the future.

6.4.1 Samples

A variety of samples which measure 12 inches wide by 36 inches long were provided by The Boeing Commercial Airplane Group and McDonnell Douglas Aerospace-

East. The Douglas samples were all 16 layer panels with a quasi-isotropic stacking sequence, i.e. varying 0°, 45°, -45°, and 90° layers. Boeing provided both 16 and 32 layer quasi-isotropic samples. The proprietary nature of the information, however, prohibits the disclosure of the exact composite material used, or the stacking sequence employed, in these samples.

A model calculation to determine the dispersion curves for these samples was computed using material parameters listed in Tables 6.8 and 6.9, which include the engineering constants supplied by NASA Langley and the corresponding elastic stiffness constants. As discussed previously, since a value for G_{23} was not available, the value of c_{44} was estimated to be 3.75 GPa in the calculation. The density of the material was taken to be 1560 kg/m³. For all of the calculations, one nodal layer per lamina was used. The dispersion curves for propagation along the length of the Boeing and Douglas 16 layer samples are shown in Figures 6.18 and 6.19, respectively. Not shown are the curves for the 32 layer Boeing samples, which were very similar to the Boeing 16 layer model. Also, since the samples are quasi-isotropic, the dispersion curves for propagation across the width of the samples are similar to what is shown for propagation along the length of the specimens.

6.4.2 Thermal-Mechanical Cycling

The combined thermal-mechanical fatigue to which these candidate materials are subjected must be representative of a typical several hour flight profile which these airplanes will undergo. Flights which cover takeoff, climbing to high altitudes, cruising

Table 6.8 Engineering constants[†] and associated elastic stiffness parameters for the Boeing samples.

Engineering Constant	Value (GPa)	Elastic Stiffness Constant	Value (GPa)
E_1	149.0	c_{11}	151.6
E_2	8.83	c_{13}	3.82
G_{12}	19.59	c_{33}	9.21
ν_{12}	0.35	c_{23}	1.71
c_{44} (see text)	3.75	c_{55}	19.59

[†]Provided by NASA Langley

Table 6.9 Engineering constants[†] and associated elastic stiffness parameters for the Douglas samples.

Engineering Constant	Value (GPa)	Elastic Stiffness Constant	Value (GPa)
E_1	153.1	c_{11}	155.0
E_2	8.69	c_{13}	3.14
G_{12}	5.17	c_{33}	8.98
ν_{12}	0.30	c_{23}	1.48
c_{44} (see text)	3.75	c_{55}	5.17

[†]Provided by NASA Langley

at extreme speeds, and finally, descending to land, subject the aircraft to a wide range of temperatures and load variations.

For the temperature profile, the initial temperature is merely that of the air on the ground. As the plane climbs to high altitude, the temperature drops. Once the cruising

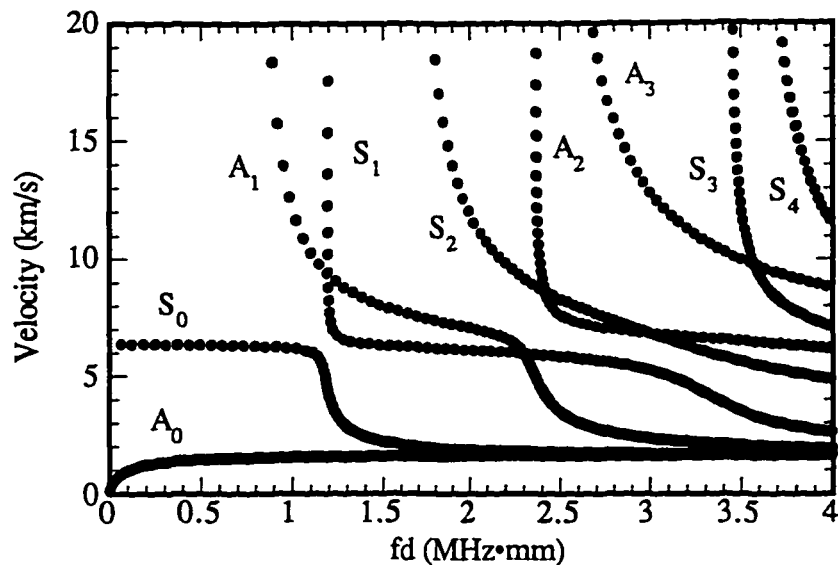


Figure 6.18 Plot of the dispersion curves for the 16 layer Boeing samples.

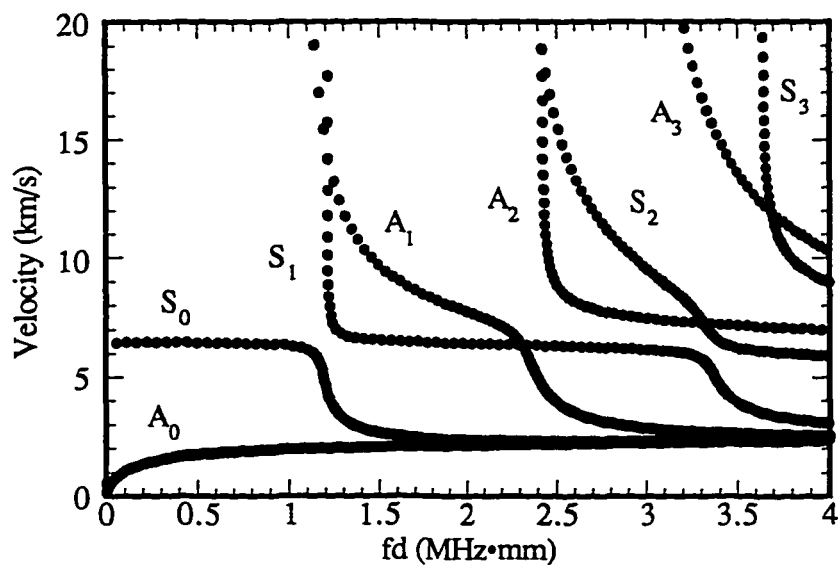


Figure 6.19 Plot of the dispersion curves for the 16 layer Douglas samples.

altitude is established, acceleration to a velocity of Mach 2.4 begins. This acceleration to higher speeds increases the temperature of the skin, especially on the leading edges of the aircraft. The skin temperature remains elevated the entire time while cruising at Mach 2.4. Finally, when descending for a landing, the airplane's speed and thus, temperature, decreases.

The strain profile is quite similar to the temperature profile. During takeoff, vibrations in the structure are evident which result in variations in the strain on the structure. As the aircraft undergoes acceleration to speeds of Mach 2.4, the strain increases. Once the cruising speed is reached, the strain decreases slightly, but stays at a sustained level due to the extreme speed. During the deceleration and decent to landing, the strain once again increases to higher levels. Finally, at any time during the flight, turbulence can be encountered which can cause momentary, quick spikes in the strain profile.

It is the combined nature of the these temperature and strain profiles which the candidate composites must be subjected. A typical profile as described above would look similar to that shown in Figure 6.20. The temperature profile shown is adapted from information contained in [71] and [72]. The strain profile shown is adapted from information obtained from [73]. The units of the temperature and strain have been omitted due to the fact that different areas of the aircraft are subject to differing levels of both strain and temperature. Obviously, the leading edges will be subjected to a higher temperature excursion than other portions of the plane. A figure showing the various skin temperatures on a Mach 2.4 aircraft can be found in [74]. A plot of the skin temperature of the aircraft as a function of Mach number and altitude can be

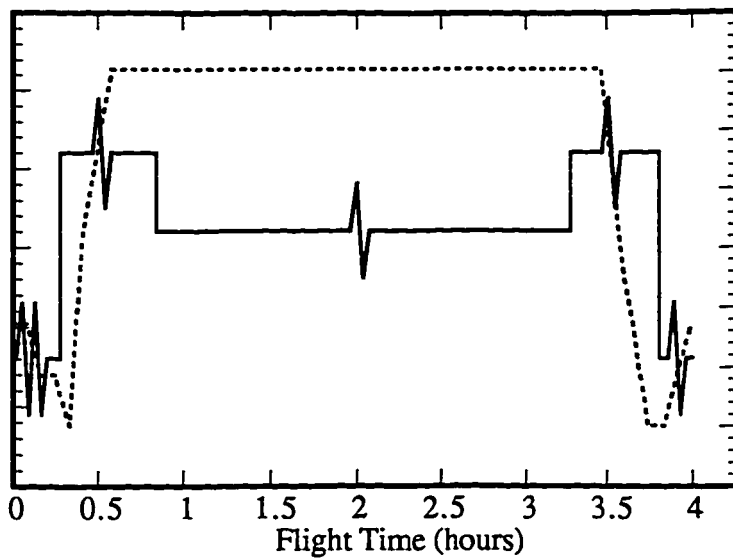


Figure 6.20 A typical several hour flight profile for the temperature (dashed line) and strain (solid line) incurred by a supersonic aircraft. The temperature profile is adapted from references 71 and 72. The strain profile is adapted from reference 73.

found in [71], which shows skin temperatures for a Mach 2.4 flight at 60,000 feet to be in the neighborhood of 300°F.

The High-Speed Research (HSR) program at NASA Langley Research Center is currently conducting duration tests for candidate advanced composite aerospace materials. The samples provided by Boeing and Douglas are undergoing a total of up to 60,000 hours of simulated flight at various strain and temperature profiles. All of the Boeing 16 ply samples are being subjected to low strain values and the Boeing 32 ply samples are being subjected to high strain values. The Douglas samples (all 16 ply) are undergoing both high and low strain levels. Again, the proprietary nature of the information prohibits the disclosure of the exact values of strain and temperature. Table 6.10 lists the details of the various samples which have been examined using the Lamb wave technique.

Table 6.10 Description of HSR test samples.

Sample	Description
Boeing 3	16 ply, isothermal, low strain #1
Boeing 4	16 ply, isothermal, low strain #2
Boeing 7	16 ply, 10,000 hour, low strain
Boeing 11	16 ply, 5,000 hour, low strain
Boeing 15	32 ply, isothermal, 40,000 cycles
Boeing 16	32 ply, 15,000 hour, high strain
Boeing 18	32 ply, 10,000 hour, high strain
Douglas 1	16 ply, 5,000 hour
Douglas 2	16 ply, 1,000 hour, accelerated
Douglas 3	16 ply, 5,000 hour
Douglas 4	16 ply, 1,000 hour, accelerated
Douglas 5	16 ply, 60,000 hour, low strain
Douglas 6	16 ply, 15,000 hour, low strain
Douglas 7	16 ply, 5,000 hour, high strain
Douglas 9	16 ply, 15,000 hour, high strain
Douglas 10	16 ply, 60,000 hour, high strain
Douglas 11	16 ply, 5,000 hour, low strain

6.4.3 Velocity Measurements

A Lamb wave was generated by using a 6 cycle, 0.5 MHz sine wave to excite a contact longitudinal wave transducer (Panametrics model V103) with a nominal center frequency of 1.0 MHz and a diameter of 0.5 inches. The signal was received at various

positions by an array of pinducers fixed in a holder, as described earlier. As before, a coupling gel was used between the transducers and the plate.

For the earlier measurements, the signals were averaged, digitized at 10 MHz on a Data Precision model DP6000 digitizer, and the waveforms saved to a PC. The separation distances of the pinducers was taken to be 4, 5, 6, and 7 cm. After acquiring and installing the commercial MacScope NuBus board, described earlier, subsequent waveforms were captured using a Macintosh IIx as a digitizer. The signals were digitized at 10 MHz, averaged, and the waveforms saved to the computer. The separation distances between the pinducers were also changed to 1, 2, 3, and 4 cm.

The time differences between the pinducers were measured by performing a cross-correlation. As before, the leading part of both waves, identified as the lowest order symmetric Lamb wave, was used in the correlation. The distances between the five pinducers in the array were held fixed at 4, 5, 6, and 7 cm (for the earlier measurements) and 1, 2, 3, and 4 cm (for subsequent measurements), respectively. The velocity of the prompt S_0 mode was obtained by a least-squares fit from a plot of time and distance.

Velocity measurements were taken in four different regions along the length of the samples, which will be defined as the 0° direction. The four values were then averaged to obtain a representative velocity along the length of the entire plate. Similarly, measurements were taken in three regions across the width of the sample, which will be defined as the 90° direction. The values were averaged to obtain a representative velocity across the width of the sample. The different regions of the measurements are shown schematically in Figure 6.21.

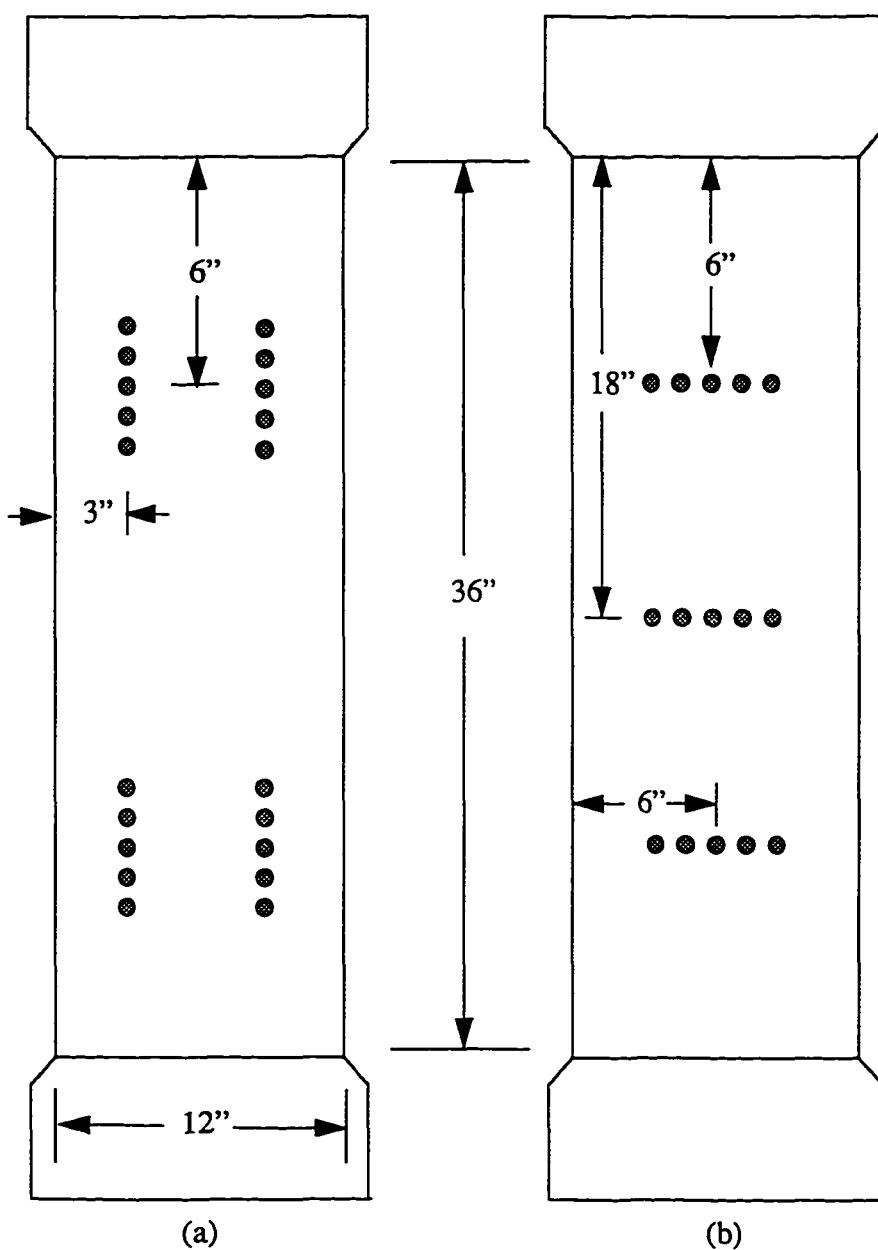


Figure 6.21 Identification of the regions for (a) the four 0° and (b) the three 90° measurements on the HSR samples. The shaded circles indicate the placement of the pinducer array.

6.4.4 Results

A total of 17 HSR samples have been examined: 7 Boeing and 10 Douglas. Of the Boeing samples, only two with fatigue hours on them have had a second velocity measurement. The remaining five samples have only had baseline (0 hours) velocities measured. All of the Douglas samples have had velocity measurements done at two different cycle times. The results of the Boeing and Douglas specimens are discussed below.

6.4.4.1 Results From the Boeing Samples

All seven Boeing samples have had baseline velocities established for them. However, no measurements have been acquired on five of the specimens since they were returned to the load frames and ovens. The results for the baseline velocities of all of the samples is shown in Table 6.11. All velocities listed are the average of the measurements taken in the 0° and 90° directions, respectively. The standard deviation for most of the measurements was within 2.5% of the average.

Of interest to note from these measurements is that the average velocity is just above 6 km/s. This is encouraging to see since this is the predicted velocity for the S₀ mode in the low frequency-thickness range (see Figure 6.18). Another interesting result is the 6% standard deviation in the average across all of the different samples. This variability is believed to be due to the high degree of inconsistency in manufacturing composites.

Table 6.11 Baseline velocity measurements for the Boeing samples.

Sample	0° direction v_{avg} (km/s)	90° direction v_{avg} (km/s)
Boeing 3	6.23	6.17
Boeing 4	6.16	6.15
Boeing 7	5.60	5.37
Boeing 11	6.31	6.35
Boeing 15	6.53	6.31
Boeing 16	6.66	6.34
Boeing 18	6.37	Not measurable [†]
Avg. Vel.	6.27 ± 0.34	6.12 ± 0.38

[†]Poor waveform and signal-to-noise ratio

Table 6.12 Velocity measurements for the Boeing samples which have had fatigue time.

Sample	Damage description	0° direction vel. (km/s)	90° direction vel. (km/s)
Boeing 11	5,281 hours	5.57	5.56
Boeing 15	40,000 cycles, isothermal	6.62	Not measurable [†]

[†]Poor waveform and signal-to-noise ratio

Two of the Boeing samples have had velocity measurements done after receiving fatigue time. The velocity measurement and damage description are shown in Table 6.12. Again, for all of the measurements, the deviation was within 2.5% of the average. When compared to the baseline value (shown in Table 6.11) for the Boeing 11 sample, the velocity dropped by around 12% in both the 0° and 90° directions. This

decrease is quite dramatic. The Boeing 15 sample actually showed just over a 1% increase in velocity, which is insignificant, however, due to the fact that the error in the measurement is on the order of 2.5%.

Not detecting any damage after 40,000 cycles in the Boeing 15 panel is not surprising. The sample was only subjected to load variations and did not undergo thermal fluctuations. Thus, the extent of damage should not be as severe as damage which is incurred under combined thermal-mechanical loading. Also, the sample is 32 plies thick (as compared to the 16 layer samples) and, therefore, should be more tolerant to damage. Finally, from an HSR standpoint, this is exactly the result which is desired because the focus of the program is to develop materials which can withstand these strenuous flight profiles without incurring much damage. The Douglas samples, discussed next, show similar results.

6.4.4.2 Results From the Douglas Samples

All of the Douglas samples had velocity measurements obtained at two different cycle levels. The first four specimens, Douglas 1 thru Douglas 4, have been run to their specified terminal cycle values. The remaining samples are presently continuing in the duration tests. The first four specimens will be treated first, followed by the remaining samples.

Douglas samples 1 and 3 were fatigued to a total of 5,000 hours. Samples 2 and 4 were fatigued, at an assumed accelerated rate, to a total of 1,000 hours. Theoretically, 1,000 accelerated hours will coincide with 5,000 normal hours of damage. Base-

line (0 hours) and 1,000 hour velocity measurements were conducted on samples 2 and

4. No baseline measurements were attained on samples 1 and 3 due to the fact that

involvement in this project did not start until after the panels had been subjected to

3,500 hours of damage. Since all four panels are identical, however, a good estimate of

a baseline velocity is available from the 0 hour velocities measured on samples 1 and

3. The results of the velocity measurements are shown in Table 6.13, where, once

again, the variation in all of the velocities for each measurement is within 2.5% of the

average.

For measurements in the 90° direction, the only sample which shows a large decrease in velocity was the 1,000 hour, Douglas 4 panel. This is an unexplained drop because the velocity in the 0° direction shows a slight increase. For the velocities in the 0° direction, the only significant decrease is seen at 5,000 hours in the Douglas 3 sample. This is mainly due to the fact that the velocity measured in one of the regions

Table 6.13 Velocity data for Douglas samples 1-4.

Sample	Damage (hours)	0° vel. (km/s)	90° vel. (km/s)
Douglas 1	3,500	6.35	6.28
	5,000	6.29	6.20
Douglas 2	0	6.43	6.50
	1,000 accelerated	6.41	6.35
Douglas 3	3,500	6.27	6.23
	5,000	5.99	6.36
Douglas 4	0	6.31	6.35
	1,000 accelerated	6.45	5.98

was found to be significantly lower than the rest of the values. Before other measurements were conducted, it was noted that this region could be near a localized damage area. A subsequent C-scan of the panel showed a large area of delamination (15 by 3 cm) in this region. The 90° velocity measurement did not show a change because none of the three measurements were done near this region.

To further investigate the damage region, panels 3 and 4 were sectioned into 6 by 1.5 inch pieces. Two coupons from each panel were obtained and the 0° velocity measured once again. For the Douglas 4 panel, the velocities in each of the two coupons were 6.42 km/s and 6.30 km/s, respectively. These are in good agreement with the measurements prior to sectioning the panel. For the Douglas 3 panel, one coupon was examined which was cut far from the delamination zone and the other coupon contained a portion of the delaminated area. For the sample with the damage, the measurement had to be done next to the delamination because the Lamb waves scattered too much when propagating within the delaminated area. The velocity for the delaminated coupon was measured to be 5.84 km/s and the velocity for the additional coupon was found to be 6.26 km/s. Thus, a significant decrease, almost 7%, is observed for the velocity measured near the delamination. These values are in good agreement with previous measurements conducted before the sample was sectioned.

The remaining six Douglas samples have had baseline measurements as well as velocity measurements after time has been accrued. The data obtained is shown in Table 6.14. Again, of interest to note is that the average baseline velocity along the length of the sample is 6.05 ± 0.09 km/s, which is in good agreement with the velocity of the S_0 mode shown in the dispersion curve for this material (Figure 6.19).

Table 6.14 Velocity measurements for remaining Douglas samples.

Sample	Damage (hours)	0° vel. (km/s)	90° vel. (km/s)
Douglas 5	0	6.05	6.13
	1,201	6.04	5.93
Douglas 6	0	5.93	6.26
	1,285	5.99	5.94
Douglas 7	0	6.03	6.03
	1,439	6.07	5.88
Douglas 9	0	6.00	6.06
	1,416	6.09	6.12
Douglas 10	0	6.11	6.00
	1,025	6.12	5.94
Douglas 11	0	6.20	6.13
	1,874	6.06	5.83

As can be seen from the table, not many hours have been accrued on the samples. Thus, as is to be expected, the velocity measurements have not changed much. For convenience, the normalized velocity is plotted as a function of damage hours in Figure 6.22, where the velocity has been normalized to the baseline value. The error bars represent estimates in the total error due mainly to the uncertainty in the signal overlap to obtain the time measurement.

The results do not show a significant decrease for the samples. However, there are two interesting features. First, the normalized velocity for the 90° direction is consistently lower than the normalized velocity in the 0° direction. The significance of this, if any, is unknown because the velocity changes are still within the error of the

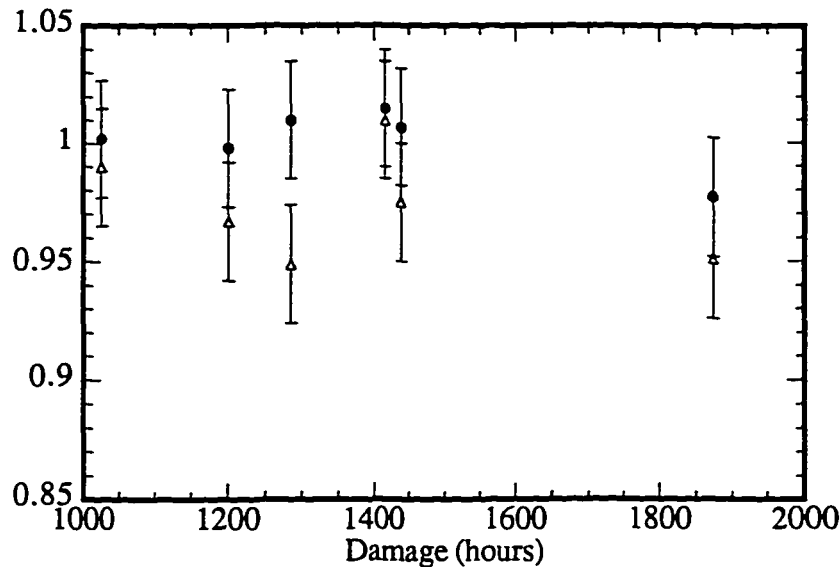


Figure 6.22 Plot of the normalized velocity in the 0° direction (solid circles) and 90° direction (open triangles) versus damage hours for the Douglas samples.

measurement. If the same trend continues as the samples are further damaged, then additional investigation is warranted. Second, the velocity drop for both directions on the sample with over 1,800 hours is slightly more than that of those grouped together with under 1,450 hours. Again, this may not be significant given the error in the measurement, but there does seem to be consistent drop in the velocity in both directions, which is not evident in the other samples with fewer hours.

6.4.5 Discussion

Presented above are the results of Lamb wave velocity measurements in thermal-mechanically damaged composite materials. These results, at present, provide the only quantitative measure of degradation for these candidate composites being investigated

under NASA's High-Speed Research (HSR) program. Due to the fact that the project is in its initial stages, the samples have not yet been subjected to extended damage. Therefore, not much change in velocity has been observed. If the specimens react well to these flight profiles, as hoped for by the HSR program, then no damage or velocity change will be observed after extended cycling. Therefore, the results obtained thus far from the Lamb wave velocity measurements are very favorable to the long range goals of the HSR program.

The results of the experimental measurements show that the baseline Lamb wave velocities compare well with those predicted by the theoretical dispersion curves. The Lamb wave technique was also able to predict a localized defect in one sample, which was later found to have a large delamination zone. A significant decrease in velocity was observed near the delamination area. The damage area was predicted via the Lamb wave technique and later verified by a C-scan.

Lamb waves have once again been shown to be useful in detecting damage. However, this time the defect was caused by thermal-mechanical cycling. Of the remaining Douglas samples, no significant changes in velocity were observed, but there did appear to be a slight drop in velocity for the sample which had been extended to over 1,800 hours. This could be an indication of the onset of damage due to thermal-mechanical fatigue.

Chapter 7

Summary and Conclusions

Determining the response to a variety of damage mechanisms (fatigue, thermal, and thermal-mechanical) is necessary for a complete understanding of the total use environment of composite structures. The objective of the research presented here was to provide a method of quantifying the amount of damage in composite materials for a number of different damage scenarios. Components which have non-visible damage, but have degraded performance, are of interest. At this level of damage, the safety margin designed into the structure may be compromised.

Lamb waves offer a useful technique for characterizing many forms of damage in composite materials. Lamb waves velocity measurements are better than conventional ultrasonic measurement schemes (i.e. through-the-thickness measurements) because they can propagate over long distances and are sensitive to the desired in-plane elastic properties of the material. It was shown in Chapter 3 that the propagation of Lamb waves depends on a variety of material properties: elastic stiffness constants, density, and thickness. As a material is damaged in some fashion, one or more of these material properties are altered. Since the Lamb wave velocity is directly related to these parameters, an effective tool exists to monitor damage in composites by measuring the velocity of these waves.

Presented in Chapter 6 are the results involving the investigation of a variety of damage mechanisms using the Lamb wave technique. The fatigue studies were conducted on a [0/90₃]_S composite where the samples were subjected to tension-tension loading in the 0° direction to induce transverse matrix cracks. The thermal damage studies were conducted on unidirectional samples which had been exposed to a range of temperatures. To study thermal-mechanical damage, quasi-isotropic composites were examined which had undergone both thermal fluctuations as well as mechanical loading.

The initial fatigue study showed that, for the results of the contact measurement, the change in modulus as measured using strain gages and change in velocity squared follow the same general trend. A change in velocity due to the modulus degradation was also seen in the results of the immersion measurement. A comparison to the numerical model showed that a reduction in c_{22} for the cracked plies produced the same change in Lamb wave velocities as were observed experimentally.

The second fatigue study examined identical samples as the first study, but the maximum load was increased and a slightly different technique was used to obtain the velocity of the Lamb waves. The crack density was also monitored as a function of fatigue cycles, which was not done previously. The results showed a decrease in normalized velocity squared with increasing fatigue cycles, which was in good agreement with the results presented in the first study. Also, the crack density was shown to increase with an increasing number of cycles and the Lamb wave velocity exhibited a decrease with increasing crack density. Thus, the Lamb wave technique gives an effective measure of the crack density in a composite.

Additionally, the modulus reduction, calculated from the crack density, was compared to the results obtained using the Lamb wave velocity measurements. A more dramatic decrease with increasing crack density was observed in the velocity measurements than in the theoretical modulus reduction. This same trend was evident in the first fatigue study, where the velocity measurements were compared to the modulus measurement obtained using strain gages. Thus, a Lamb wave technique used at low frequencies may be more sensitive and provide an improved method of interrogation over other techniques which measure damage progression.

Presented in the third experiment are the results of Lamb wave velocity measurements in thermally damaged composites. The velocity was measured in the fiber direction for unidirectional samples which had varying levels of thermal damage. The results showed that the velocity of the lowest order symmetric Lamb mode dropped significantly for extended thermal damage. Theoretical calculations with reduced values of c_{11} showed that a reduction in this parameter lowered velocities of the S_0 mode, which corresponded well to the velocity reduction of the samples.

Finally, Lamb wave velocity measurements were used to examine thermally damaged candidate composite materials being investigated under NASA's High-Speed Research (HSR) program. The results of the experimental measurements showed that the Lamb wave velocities measured for the undamaged samples compare well with theoretical predictions. Also, it was found that the Lamb wave technique was also able to predict a local defect in a specimen when one sample, which was later found to have a large delamination zone, was characterized well using Lamb wave velocity measurements. A significant decrease in velocity was observed near the

predicted delamination area, which was later verified by a C-scan of the sample. Of the Douglas samples which were measured with less than 1,500 hours damage, no significant changes in velocity were noted. However, a slight drop in velocity in both the 0° and 90° directions was observed for a sample which had been extended to over 1,800 hours of damage. This could be an indication of the onset of damage due to thermal-mechanical fatigue.

The Lamb wave velocity measurements in all of the studies were conducted at long wavelengths. In this regime, the composite can be treated as homogeneous. Also, the effective elastic properties of the material can be measured because local defects, which scatter high frequency waves, will not be observed at long wavelengths. The measurement of the Lamb wave velocity was also found to be more sensitive to fatigue damage than modulus measurements. Thus, a Lamb wave technique used at long wavelengths to track damage in composites may provide improved interrogation of the effective stiffness of a structure over the propagation length of the wave.

Composites are being widely used in aerospace structures, as well as a number of other applications, because of their many advantages over metals. As technology increases, the use of composite structures will continue to spread and they will become an integral part of our lives, whether it be travel, health, or recreation. Further understanding of these materials is vital in determining the safety and reliability of such structures.

The Lamb wave velocity is a quantitative measurement and it has been shown by this work to be an effective tool in monitoring a variety of damage in composites. Thus, the Lamb wave method can be used to verify the integrity of a composite struc-

ture over the service life of a component. This is an important measurement for flight qualified composite materials that may have undergone some measure of non-visible damage, which could seriously degrade the performance of the structure. Since the Lamb wave velocity depends on a variety of material properties, an ideal technique exists to monitor composites as damage is incurred. With the continued development of damage assessment techniques such as the Lamb wave method, the safety of such structures can be assured.

Appendix A

Laminated composites are used in a manner such that they carry mainly in-plane loads. Therefore, the majority of composite applications involve thin plate structures where the stresses in the out-of-plane direction can be considered to be zero. In abbreviated subscript notation, this means that

$$T_3 = 0, \quad T_4 = 0, \quad T_5 = 0. \quad (\text{A.1})$$

Given equation (A.1) and using the fact that unidirectional laminas can be considered to be transversely isotropic, i.e. $c_{12} = c_{13}$, $c_{22} = c_{33}$, and $c_{55} = c_{66}$, the stress-strain relation can now takes the form

$$\begin{bmatrix} T_1 \\ T_2 \\ 0 \\ 0 \\ 0 \\ T_6 \end{bmatrix} = \begin{bmatrix} c_{11} & c_{13} & c_{13} & 0 & 0 & 0 \\ c_{13} & c_{33} & c_{23} & 0 & 0 & 0 \\ c_{13} & c_{23} & c_{33} & 0 & 0 & 0 \\ 0 & 0 & 0 & c_{44} & 0 & 0 \\ 0 & 0 & 0 & 0 & c_{55} & 0 \\ 0 & 0 & 0 & 0 & 0 & c_{55} \end{bmatrix} \begin{bmatrix} S_1 \\ S_2 \\ S_3 \\ S_4 \\ S_5 \\ S_6 \end{bmatrix}. \quad (\text{A.2})$$

Multiplying out and disregarding the terms which are zero gives the relations

$$\begin{aligned}
 T_1 &= c_{11}S_1 + c_{13}(S_2 + S_3), \\
 T_2 &= c_{13}S_1 + c_{33}S_2 + c_{23}S_3, \\
 0 &= c_{13}S_1 + c_{23}S_2 + c_{33}S_3, \\
 T_6 &= c_{55}S_6.
 \end{aligned} \tag{A.3}$$

Eliminating the out-of-plane strain, S_3 , yields

$$\begin{aligned}
 T_1 &= \left(c_{11} - \frac{c_{13}^2}{c_{33}}\right)S_1 + \left(c_{13} - \frac{c_{13}c_{23}}{c_{33}}\right)S_2, \\
 T_2 &= \left(c_{13} - \frac{c_{13}c_{23}}{c_{33}}\right)S_1 + \left(c_{33} - \frac{c_{23}^2}{c_{33}}\right)S_2, \\
 T_6 &= c_{55}S_6.
 \end{aligned} \tag{A.4}$$

In a more compact notation, equation (A.4) can be written as

$$[T] = [Q][S], \tag{A.5}$$

where

$$[T] = \begin{bmatrix} T_1 \\ T_2 \\ T_6 \end{bmatrix}, \quad [Q] = \begin{bmatrix} Q_{11} & Q_{12} & 0 \\ Q_{12} & Q_{22} & 0 \\ 0 & 0 & Q_{66} \end{bmatrix}, \quad [S] = \begin{bmatrix} S_1 \\ S_2 \\ S_6 \end{bmatrix}. \tag{A.6}$$

The Q_{IJ} are defined as the reduced stiffness components and have the values

$$\begin{aligned}
 Q_{11} &= \left(c_{11} - \frac{c_{13}^2}{c_{33}}\right), & Q_{12} &= \left(c_{13} - \frac{c_{13}c_{23}}{c_{33}}\right), \\
 Q_{22} &= \left(c_{33} - \frac{c_{23}^2}{c_{33}}\right), & Q_{66} &= c_{55}.
 \end{aligned} \tag{A.7}$$

As can be seen, only four reduced stiffness constants (written in terms of the five elastic stiffness constants) are needed to describe a transversely isotropic composite. This is the reason four engineering constants are commonly used to describe thin composite plates. The engineering constants are related to the reduced stiffness constant by [2]

$$\begin{aligned} Q_{11} &= \frac{E_1}{1 - v_{12}v_{21}}, & Q_{12} &= \frac{v_{12}E_2}{1 - v_{12}v_{21}}, \\ Q_{22} &= \frac{E_2}{1 - v_{12}v_{21}}, & Q_{66} &= G_{12}, \end{aligned} \quad (\text{A.8})$$

where E_1 , E_2 , and G_{12} are the moduli (longitudinal, transverse, and shear, respectively), and the v_{IJ} are Poisson's ratios for stress in the i -direction and strain in the J -direction [2]. The Poisson's ratios are not independent, however, and are shown to be related by [2]

$$v_{21} = \frac{E_2}{E_1} v_{12}. \quad (\text{A.9})$$

Therefore, only four independent engineering parameters are needed to describe the system. Also, from the transversely isotropic symmetry, the relations between the various engineering constants are given by [2]

$$E_2 = E_3, \quad G_{12} = G_{13}, \quad v_{12} = v_{13}. \quad (\text{A.10})$$

It was noted earlier that the four reduced stiffness parameters in equation (A.7) are expressed in terms of five elastic stiffness constants. This is due to the fact that only in-plane stresses were considered. To solve for the c_{IJ} 's, a fifth equation must be

introduced. Since a value of G_{23} ($= c_{44}$) is not available, it must be estimated using common values for laminated composites. It was shown previously that c_{44} is not independent from the other elastic stiffness constants and has a value

$$c_{44} = \frac{c_{33} - c_{23}}{2}. \quad (\text{A.11})$$

This is the fifth equation needed to solve for the elastic stiffness constants in terms of the engineering constants E_1 , E_2 , G_{12} , v_{12} , and G_{23} ($= c_{44}$). Using equations (A.7), (A.8), (A.9), and (A.11), the five elastic stiffness parameters are found to be

$$\begin{aligned} c_{11} &= \frac{E_1^2(E_2 - 4c_{44})}{4c_{44}(v_{12}^2 E_2 - E_1) + E_1 E_2}, \\ c_{13} &= \frac{2c_{44}v_{12}E_1E_2}{4c_{44}(E_1 - v_{12}^2 E_2) - E_1 E_2}, \\ c_{33} &= \frac{4c_{44}^2(E_1 - v_{12}^2 E_2)}{4c_{44}(E_1 - v_{12}^2 E_2) - E_1 E_2}, \\ c_{23} &= \frac{2c_{44}(2c_{44}E_1 - E_1 E_2 - 2c_{44}v_{12}^2 E_2)}{4c_{44}(v_{12}^2 E_2 - E_1) + E_1 E_2}, \\ c_{55} &= G_{12}. \end{aligned} \quad (\text{A.12})$$

Therefore, given four engineering parameters, which can be found widely in the literature [2], and estimating c_{44} allows one to compute the five elastic stiffness constants for the material. These five parameters are the values which are used in the numerical model to calculate the dispersion curves for a laminated composite plate.

Appendix B

This appendix contains the source code in FORTRAN for the program which was written in order to generate numerical dispersion curves for composite samples. The theory, developed in Chapter 4, is based on the development of Datta, et al. [60]. When compiled, the program is linked to the object file cg.o, which is a subroutine that finds the eigenvalues and eigenvectors of a complex matrix. The source code was obtained from [75]. Also, a subroutine used to invert a matrix is adapted from Lee [76]. The program was written with the more commonly used nomenclature of c_{22} and c_{12} , instead of c_{33} and c_{13} (which were used in the theory). However, since $c_{33} = c_{22}$ and $c_{13} = c_{12}$, the program is consistent with the theoretical development. The source code for the program now follows.

C PROGRAM: lamb1.f

C This program will calculate dispersion curves for composite
C samples. The theory is based on a paper by Datta. The arrays
C are dimensioned large enough to allow up to 50 layers (provided
C there is only one nodal layer per layer). The array dimensions
C allow for specifications where $4 * (\text{number of layers in composite}) *$
C $(\text{number of sub-layers per layer [nodal layers]}) + 2$ is less than
C 250. Besides these restrictions on size (which can be altered by
C larger dimensions in the array declarations), the user is allowed to
C input any density, any thickness, and any angle for each layer
C throughout the plate. The user is also instructed to enter the 5
C C_{ij} 's (given the coordinate system specified in the program). After
C calculating the full matrix for the plate, the user inputs ranges of
C k (wavenumbers) for which the eigenfrequencies ω^2 will be solved.

C Given the omega and k values, one can convert these to velocity
C (ω/k) and frequency*thickness values. Thus, a dispersion curve
C is generated. The values of fd (MHz*mm) and vel. (km/s) is then saved
C to a file. The user is also allowed to do a mode identification if
C desired. The values of fd and velocity are saved to a file which also
C states if the modes are symmetric (S) or antisymmetric (A).
C Referencing this file while looking at the dispersion curves allows
C the user to identify each mode (for $fd < 5$ and $vel < 40$) in the plot.
C The program when compiled, is linked to the object routine cg.o (which
C is the routine that solves complex eigenvalues and vectors).

C Programmed by: Mike Seale
C Last modified: 06/06/96

PARAMETER (Pi= 3.14159)

```
INTEGER numlayers, l, r, n, dim, i, j, k, nodes, del, nkpts
INTEGER flag, totnodes, err, matdim, laydim, matz
REAL density, h, ih, fd(1000,250), low, step, wn
REAL ik1(50,6,6), ik2(50,6,6), ik3(50,6,6), im(50,6,6)
REAL c(50,5,5), k1(250,250), k2(250,250), k3(250,250)
REAL k2star(250,250), vel, freq, D, root, Dtemp, veltemp
REAL v(1000,250), m(250,250)
REAL treal(250,250), timag(250,250), invmk1(250,250), invmk2(250,250)
REAL invmk3(250,250), er(250), ei(250), evr(250,250), evi(250,250)
REAL z1(250), z2(250), z3(250), omega, idfd(250), idv(250)
CHARACTER*20 fname,ans
```

```
laydim = 50
matdim = 250
```

5 FORMAT(A)

C Get specifications of composite (layup, thickness, etc.)

```
CALL GETSPECS(laydim, density, numlayers, h, c, nodes)
```

```
WRITE(6,*)"Orientation and Specs done."
WRITE(6,*),''
```

```
totnodes= nodes*numlayers
ih= h/FLOAT(totnodes)
dim= INT(4*totnodes + 2)
```

```
WRITE(6,*)"layers in composite =      ', numlayers
WRITE(6,*)"density (kg/m^3) =      ',density
WRITE(6,*)"total thickness (meters) =   ',h
```

```

WRITE(6,*)"nodes per layer =      ", nodes
WRITE(6,*)"total nodal layers in plate =  ",totnodes
WRITE(6,*)"thickness of each nodal layer = ',ih
WRITE(6,*)"dimension of matrix =      ",dim
WRITE(6,*)""

```

C Zero out all elements of matricies for each sub-layer

```

CALL ZEROLAYER(laydim, ik1, totnodes, 6)
CALL ZEROLAYER(laydim, ik2, totnodes, 6)
CALL ZEROLAYER(laydim, ik3, totnodes, 6)
CALL ZEROLAYER(laydim, im, totnodes, 6)

```

C Zero out all elements of matricies for entire plate

```

CALL ZEROMATRIX(madim, dim, k1)
CALL ZEROMATRIX(madim, dim, k2)
CALL ZEROMATRIX(madim, dim, k3)
CALL ZEROMATRIX(madim, dim, m)

```

C Generate 6 x 6 individual element matricies for each nodal layer.

```
CALL GETELEMENT(laydim,6,numlayers,ik1,ik2,ik3,im,c,density,ih, nodes)
```

C Generate dim x dim matricies (add up all layers)

```

DO i= 1, totnodes
    del= INT(4*(i-1))
    DO j= 1, 6
        DO k= 1, 6
            m(j+del,k+del)= m(j+del,k+del)+im(i,j,k)
            k1(j+del,k+del)= k1(j+del,k+del)+ik1(i,j,k)
            k2(j+del,k+del)= k2(j+del,k+del)+ik2(i,j,k)
            k3(j+del,k+del)= k3(j+del,k+del)+ik3(i,j,k)
        END DO
    END DO
END DO

```

C Evaluate k2* in the thoeretical equation

```

DO i= 1,dim
    DO j= 1,dim
        k2star(i,j)= k2(i,j) - k2(j,i)
    END DO
END DO

```

```

      WRITE(6,*)"Full matrices done for entire plate."
      WRITE(6,*)""

C   Invert the matrix m
C   Subroutine adapted from Lee [76]

      CALL INVERT(matdim,m,dim)

C   Multiply eigenvalue equation through by m-inverse.

      CALL ZEROMATRIX(matdim,dim,invmk1)
      CALL ZEROMATRIX(matdim,dim,invmk2)
      CALL ZEROMATRIX(matdim,dim,invmk3)

      CALL MATMULT(matdim,m,k1,invmk1,dim)
      CALL MATMULT(matdim,m,k2star,invmk2,dim)
      CALL MATMULT(matdim,m,k3,invmk3,dim)

C   Get the range of wavenumber (wn) values for which to solve and
C   find roots for eigenvalue equation (wn~1/m, freq~1/s). The eigenvalues
C   for each k point (wavenumber) are angular frequency squared (omega~1/s^2).

      CALL GETVALS(low,step,nkpts, fname)

      DO k = 1,nkpts
          wn = low + step*FLOAT(k-1)
          DO i = 1,dim
              DO j = 1,dim
                  treal(i,j) = invmk1(i,j)*wn*wn + invmk3(i,j)
                  timag(i,j) = -invmk2(i,j)*wn
              END DO
          END DO

          matz = 0
          flag = 0

          IF (k .eq. INT(nkpts/10)) THEN
              WRITE(6,*)""
              WRITE(6,*)"Want to do a mode ID (y or n)?"
              READ(5,5), ans
              WRITE(6,*)""
          ELSE
              ans = 'n'
          END IF

          IF (ans .EQ. 'y' .OR. ans .EQ. 'Y') THEN

```

```

        matz = 1
        flag = 1
    END IF

    CALL CG(matdim,dim,treal,timag,er,ei,matz,evr,evi,z1,z2,z3,err)

    DO j = 1,dim
        IF (er(j) .lt. 0) THEN
            er(j) = 0.0
        END IF
        omega = SQRT(er(j))/1000000.0
        fd(k,j) = omega*h*500/Pi
        v(k,j) = omega*1000.0/wn
    END DO

    WRITE(6,*)"Eigenvalues done for k point ',k,' of ',nkpts

    IF (flag .EQ. 1) THEN
        DO j = 1,dim
            idfd(j) = fd(k,j)
            idv(j) = v(k,j)
        END DO

        CALL MODEID(matdim,dim,evr,h,idfd,idv)

    END IF
END DO

OPEN (UNIT= 8, FILE= fname, STATUS='NEW')

WRITE(8,*)"fd (MHz*mm)',CHAR(9),'vel. (km/s)'
DO i= 1, nkpts
    DO j= 1, dim
        WRITE(8,*) fd(i,j), CHAR(9), v(i,j)
    END DO
END DO

CLOSE(8)

WRITE(6,*)"'
WRITE(6,*)" File saved: ',fname
WRITE(6,*)"'

END

```

C

SUBROUTINE GETSPECS(ld, density, numlayers, h, c, nodes)

C Get material parameters and spect for the calculation.
 C Options 1-9 are pre-made documents from which the material
 C parameters can be read.

PARAMETER (pi=3.14159)

INTEGER numlayers, nodes, ld, opt, numopts
 REAL density, h, angle(50), a, c(ld,5,5), para(6)
 REAL c11, c12, c22, c23, c44, c55, b1, b2, b3
 CHARACTER*25 ans, material, ans1

numopts = 10

10 WRITE(6,*)"Choose one of the following material options:'

WRITE(6,*) ''
 WRITE(6,*)' 1) Aluminum'
 WRITE(6,*)' 2) AS4/3501-6'
 WRITE(6,*)' 3) AS4/3502'
 WRITE(6,*)' 4) AS4/976'
 WRITE(6,*)' 5) AS4/977-3'
 WRITE(6,*)' 6) IM7/977-3'
 WRITE(6,*)' 7) IM6/SC1081'
 WRITE(6,*)' 8) Douglas IM7/K3B'
 WRITE(6,*)' 9) Boeing IM7/5260'
 WRITE(6,*)'10) Input your own values for Cij'
 WRITE(6,*) ''
 READ(5,*) opt

IF (opt .LT. numopts) THEN

CALL GETPROP(opt,material,para)

ELSE IF (opt .EQ. numopts) THEN

material = 'values entered by you'

WRITE(6,*) ''

WRITE(6,*) 'Input the denisty (kg/m^3):'

READ(5,*) para(1)

WRITE(6,*) ''

WRITE(6,*) 'Assuming x is in the fiber direction and z is'

WRITE(6,*) 'perpendicular to the plate, enter the following:'

WRITE(6,*) ''

WRITE(6,*) 'Enter c11 (GPa): '

READ(5,*) para(2)

WRITE(6,*) 'Enter c12 (GPa): '

READ(5,*) para(3)

WRITE(6,*) 'Enter c22 (GPa): '

READ(5,*) para(4)

```

      WRITE(6,*) 'Enter c23 (GPa): '
      READ(5,*) para(5)
      WRITE(6,*) 'Enter c55 (GPa): '
      READ(5,*) para(6)
   ELSE
      GOTO 10
   END IF

density = para(1)
c11= para(2)
c12= para(3)
c22= para(4)
c23= para(5)
c55= para(6)

      WRITE(6,*)'
      WRITE(6,*)"Material: ',material
      WRITE(6,*)'
      WRITE(6,*)"Density (kg/m^3) = ',density
      WRITE(6,*)"c11 (GPa) =      ',c11
      WRITE(6,*)"c12 (GPa) =      ',c12
      WRITE(6,*)"c22 (GPa) =      ',c22
      WRITE(6,*)"c23 (GPa) =      ',c23
      WRITE(6,*)"c55 (GPa) =      ',c55
      WRITE(6,*)'

      WRITE(6,*) 'Enter the total thickness of the plate (meters): '
      READ(5,*) h
      WRITE(6,*)'
      WRITE(6,*)"How many layers does the plate have? "
      READ(5,*) numlayers
      WRITE(6,*)"How many nodes per layer do you want? "
      READ(5,*) nodes

      DO i= 1, numlayers
         DO j= 1,5
            DO k= 1,5
               c(i,j,k)= 0.0
            END DO
         END DO
      END DO

```

C Find Cij's for various angles of the plies.

```

      WRITE(6,*) 'Enter the angle in degrees of ply # ',i
      READ(5,*) angle(i)

```

```

a= REAL(pi*angle(i)/180.0)

c(i,2,2)= c22*1.0E9
c(i,1,2)= (c12*cos(a)**2 + c23*sin(a)**2)*1.0E9
b1= sin(a)**2*(c12*cos(a)**2 + c22*sin(a)**2)
b2= cos(a)**2*(c11*cos(a)**2 + c12*sin(a)**2)
b3= (c55*sin(2*a)**2)/2.0
c(i,1,1)= (b1 + b2 + b3)*1.0E9
c(i,5,5)= (c55*cos(a)**2+((c22-c23)/2)*sin(a)**2)*1.0E9

END DO

WRITE(6,*)''

C Allow user to reduce the Cij's in specific layers to simulate
C damage in those layers.

5 FORMAT(A)
WRITE(6,*)"Do you want to reduce the stiffnesses in specific layers?"
READ(5,5) ans1

IF (ans1.EQ.'Y' .OR. ans1.EQ.'y') THEN
    CALL REDUCE(ld,numlayers,angle,c)
END IF

C Check to see if Cij's reduced correctly.

C DO i=1,numlayers
C     WRITE(6,*)"Stiffnesses for layer #",i
C     WRITE(6,*)"c11 = ",c(i,1,1)
C     WRITE(6,*)"c12 = ",c(i,1,2)
C     WRITE(6,*)"c22 = ",c(i,2,2)
C     WRITE(6,*)"c55 = ",c(i,5,5)
C     WRITE(6,*)""
C END DO

RETURN
END
C _____

SUBROUTINE ZEROMATRIX(md, max, t)

C Zero matrices for entire plate before defining them.

INTEGER max, md
REAL t(md,md)

```

```

DO i= 1, max
  DO j= 1, max
    t(i,j)= 0.0
  END DO
END DO

```

```

RETURN
END

```

C

```
SUBROUTINE GETELEMENT(ld,max,num,ik1,ik2,ik3,im,c,s,ih,nodes)
```

C Define matrix elements for m, k1, k2, and k3 matrices

```

INTEGER num, nodes,i, j, k, m, n, ld, max
REAL ik1(ld,max,max), ik2(ld,max,max), ik3(ld,max,max)
REAL im(ld,max,max), c(ld,5,5), s, ih

```

```

DO i= 1, num
  DO j= 1, nodes
    k= INT(nodes*(i-1) + j)

    im(k,1,1)= 2.*s*ih/15.
    im(k,2,2)= im(k,1,1)
    im(k,3,3)= 8.*s*ih/15.
    im(k,4,4)= im(k,3,3)
    im(k,5,5)= im(k,1,1)
    im(k,6,6)= im(k,1,1)
    im(k,1,3)= s*ih/15.
    im(k,2,4)= im(k,1,3)
    im(k,3,5)= im(k,1,3)
    im(k,4,6)= im(k,1,3)
    im(k,1,5)= -s*ih/30.
    im(k,2,6)= im(k,1,5)

```

```

ik1(k,1,1)= 2.*ih*c(i,1,1)/15.
ik1(k,2,2)= 2.*ih*c(i,5,5)/15.
ik1(k,3,3)= 8.*ih*c(i,1,1)/15.
ik1(k,4,4)= 8.*ih*c(i,5,5)/15.
ik1(k,5,5)= ik1(k,1,1)
ik1(k,6,6)= ik1(k,2,2)
ik1(k,1,3)= ih*c(i,1,1)/15.
ik1(k,2,4)= ih*c(i,5,5)/15.
ik1(k,3,5)= ik1(k,1,3)
ik1(k,4,6)= ik1(k,2,4)

```

$ik1(k,1,5) = -ih*c(i,1,1)/30.$
 $ik1(k,2,6) = -ih*c(i,5,5)/30.$

$ik3(k,1,1) = 7.*c(i,5,5)/(3.*ih)$
 $ik3(k,2,2) = 7.*c(i,2,2)/(3.*ih)$
 $ik3(k,3,3) = 16.*c(i,5,5)/(3.*ih)$
 $ik3(k,4,4) = 16.*c(i,2,2)/(3.*ih)$
 $ik3(k,5,5) = ik3(k,1,1)$
 $ik3(k,6,6) = ik3(k,2,2)$
 $ik3(k,1,3) = -8.*c(i,5,5)/(3.*ih)$
 $ik3(k,2,4) = -8.*c(i,2,2)/(3.*ih)$
 $ik3(k,3,5) = ik3(k,1,3)$
 $ik3(k,4,6) = ik3(k,2,4)$
 $ik3(k,1,5) = c(i,5,5)/(3.*ih)$
 $ik3(k,2,6) = c(i,2,2)/(3.*ih)$

```
DO m=1,6
  DO n= 1,6
    im(k,n,m)= im(k,m,n)
    ik1(k,n,m)= ik1(k,m,n)
    ik3(k,n,m)= ik3(k,m,n)
  END DO
END DO
```

$ik2(k,1,2) = -c(i,1,2)/2.$
 $ik2(k,1,4) = 2.*c(i,1,2)/3.$
 $ik2(k,1,6) = -c(i,1,2)/6.$
 $ik2(k,2,1) = -c(i,5,5)/2.$
 $ik2(k,2,3) = 2.*c(i,5,5)/3.$
 $ik2(k,2,5) = -c(i,5,5)/6.$
 $ik2(k,3,2) = -2.*c(i,1,2)/3$
 $ik2(k,3,6) = 2.*c(i,1,2)/3.$
 $ik2(k,4,1) = -2.*c(i,5,5)/3.$
 $ik2(k,4,5) = 2.*c(i,5,5)/3.$
 $ik2(k,5,2) = c(i,1,2)/6.$
 $ik2(k,5,4) = -2.*c(i,1,2)/3.$
 $ik2(k,5,6) = c(i,1,2)/2.$
 $ik2(k,6,1) = c(i,5,5)/6.$
 $ik2(k,6,3) = -2.*c(i,5,5)/3.$
 $ik2(k,6,5) = c(i,5,5)/2.$

```
END DO
END DO
```

```
RETURN
END
```

C

SUBROUTINE ZEROLAYER(ld, t, number, max)

C Zero matrix elements for each layer before defining them.

INTEGER max, number, ld
REAL t(ld,max,max)

```
DO k= 1, number
    DO i= 1, max
        DO j= 1, max
            t(k,i,j)= 0.0
        END DO
    END DO
END DO
```

RETURN
END

C

SUBROUTINE INVERT(md, a, n)

C Invert a matrix (adapted from Lee [76])

INTEGER n, md
REAL a(md,md),x

```
DO 1 i = 1,n
    x = a(i,i)
    a(i,i) = 1.0
    DO 2 j = 1,n
        a(i,j) = a(i,j)/x
        DO 1 k = 1,n
            IF (k-i) 3,1,3
3           x = a(k,i)
            a(k,i) = 0.0
            DO 4 j = 1,n
4           a(k,j) = a(k,j) - x*a(i,j)
1       CONTINUE
      RETURN
END
```

C

```

SUBROUTINE MATMULT(md, a, b, c, n)

C   Multiply two matrices.

INTEGER i,j,k,n
REAL a(md,md),b(md,md),c(md,md)

DO i = 1,n
    DO j = 1,n
        c(i,j) = 0.0
        DO k = 1,n
            c(i,j) = c(i,j) + a(i,k)*b(k,j)
        END DO
    END DO
END DO

RETURN
END

C _____
```

```

SUBROUTINE GETVALS(low, step, numk, filename)

C   Get range of wavenumbers for which to solve.

INTEGER numk
REAL step, low
CHARACTER*20 filename

c   low = 10.0
c   step = 20.0
c   numk = 250

      WRITE(6,*)"Enter the number of k (wavenumber) points to solve for:"
      READ(5,*),numk
      WRITE(6,*)"Enter the low value for the wavenumbers (1/m):"
      READ(5,*),low
      WRITE(6,*)"Enter the step size for the wavenumbers:"
      READ(5,*),step

5   FORMAT(A)
      WRITE(6,*)"Enter file name to be stored:"
      READ(5,5), filename

      RETURN
END
```

```

SUBROUTINE MODEID(md,dim,vects,h,idfd,idv)

C The graphs are shown for the eigenvectors in the x-direction
C (along the length of the plate - ie. Ux displacements). The
C thickness direction is along the z-axis. Therefore, the z=0
C plane is the mid-plane of the plate. Thus, the symmetry with
C respect to the x-axis (in plot which is shown, not material
C x-axis) is the symmetry of the mode.

INTEGER i,j,md,dim
REAL vects(md,*),h,x(250),y(250),idfd(md),idv(md)
CHARACTER*20 file, mode

5 FORMAT(A)

WRITE(6,*) ''
WRITE(6,*)'Enter file to store mode IDs in:'
READ(5,5),file

OPEN (UNIT= 8, FILE=file, STATUS='NEW')
WRITE(8,*) 'fd (MHz*mm)',CHAR(9),'vel. (km/s)',CHAR(9),'mode'

DO j = 1, dim
    DO i = 1, dim/2
        x(i) = vects(2*i - 1,j)
        y(i) = h*(0.5 - FLOAT(2*i-2)/FLOAT(dim-2))
    END DO

    IF (idfd(j) .LT. 5.0 .AND. idv(j) .LT. 40.0) THEN
        WRITE(6,*)"fd = ',idfd(j),' v = ',idv(j)
        CALL GENPLT(x,y,dim/2)
        WRITE(6,*)"Is the mode symmetric (s) or antisymmetric (a)?"
        READ(5,5), mode
        WRITE(8,*) idfd(j), CHAR(9), idv(j),CHAR(9),mode
    END IF

END DO

CLOSE(8)

RETURN
END

```

C _____

```

SUBROUTINE GENPLT(x,y,npts)

C Just a subroutine (on DECstation) to plot x vs. y.

DIMENSION x(2048),y(2048)
INTEGER npts

OPEN(UNIT=1,FILE='graph.xg',STATUS='NEW',FORM='FORMATTED')

DO j=1,npts

WRITE(1,*)x(j),y(j)

END DO

CLOSE(1)

p=system('/usr/users/btsmith/xgraph/xgraph graph.xg')

IF (p .EQ. 0) THEN

    type*, 'status return ok'
ELSE

    type *, 'ERROR STATUS = ',p
END IF

OPEN(UNIT=1,FILE='graph.xg',STATUS='OLD',FORM='FORMATTED')
CLOSE (UNIT=1,STATUS='DELETE')

END

```

C

```

SUBROUTINE GETPROP(opt,material,para)

C Retrieves properties already saved for some materials.

INTEGER opt
REAL para(6)
CHARACTER*25 material, fname

IF (opt .EQ. 1) THEN
    fname = 'alum.doc'
ELSE IF (opt .EQ. 2) THEN
    fname = 'as435016.doc'
ELSE IF (opt .EQ. 3) THEN

```

```

        fname = 'as43502.doc'
ELSE IF (opt .EQ. 4) THEN
    fname = 'as4976.doc'
ELSE IF (opt .EQ. 5) THEN
    fname = 'as49773.doc'
ELSE IF (opt .EQ. 6) THEN
    fname = 'im79773.doc'
ELSE IF (opt .EQ. 7) THEN
    fname = 'im6sc1081.doc'
ELSE IF (opt .EQ. 8) THEN
    fname = 'im7k3b.doc'
ELSE
    fname = 'im75260.doc'
END IF

```

5 FORMAT(A)

```

OPEN (UNIT=10,FILE =fname,STATUS= 'OLD', FORM= 'FORMATTED')
READ(10,5) material
DO i = 1,6
    READ(10,*) para(i)
END DO
CLOSE(10)

```

```

RETURN
END

```

C

SUBROUTINE REDUCE(ld,numlayers,angle,c)

C Reduces the values of Cij in specific layers.

```

PARAMETER (pi=3.14159)
INTEGER numlayers, ld, opt
REAL angle(50), c(ld,5,5), a, ang, c11, c12, c22, c23, c55

```

15 WRITE(6,*)' '
WRITE(6,*)"Choose an option:"
WRITE(6,*)' '
WRITE(6,*)"1) Reduce Cij in layers of a particular angle"
WRITE(6,*)"2) Finished"
WRITE(6,*)' '
READ(5,*) opt

IF (opt.EQ.1) THEN
 WRITE(6,*)"Reduce layers of angle (degrees):"

```

READ(5,*) ang

WRITE(6,*)"Enter c11 (GPa) for these layers:"
READ(5,*) c11
WRITE(6,*)"Enter c12 (GPa) for these layers:"
READ(5,*) c12
WRITE(6,*)"Enter c22 (GPa) for these layers:"
READ(5,*) c22
WRITE(6,*)"Enter c23 (GPa) for these layers:"
READ(5,*) c23
WRITE(6,*)"Enter c55 (GPa) for these layers:"
READ(5,*) c55

a = REAL(pi*ang/180.0)

DO i = 1,numlayers
  IF (angle(i).EQ.ang) THEN

    c(i,2,2)=c22*1.0E9
    c(i,1,2)=(c12*cos(a)**2 + c23*sin(a)**2)*1.0E9
    b1= sin(a)**2*(c12*cos(a)**2 + c22*sin(a)**2)
    b2= cos(a)**2*(c11*cos(a)**2 + c12*sin(a)**2)
    b3= 2*c55*cos(a)**2*sin(a)**2
    c(i,1,1)=(b1 + b2 + b3)*1.0E9
    c(i,5,5)=(c55*cos(a)**2+((c22-c23)/2)*sin(a)**2)*1.0E9

  END IF
END DO

ELSE
  GOTO 25
END IF

GOTO 15

25  RETURN
END

```

Bibliography

- [1] Eric Baer, Anne Hiltner, and Roger J. Morgan, "Biological and Synthetic Hierarchical Composites," *Physics Today*, Vol. 45, No. 10, Oct. 1992, pp. 60-67.
- [2] Isaac M. Daniel and Ori Ishai, *Engineering Mechanics of Composite Materials*, Oxford University Press, Inc., New York, 1994, pp. 3-76.
- [3] D. Stover, senior editor, "Composites Use Increases on New Commercial Transports...," *Advanced Composites*, Vol. 6, No. 5, Sept./Oct. 1991, pp. 30-40.
- [4] Composites News, "Boron/Epoxy System to Repair Entire B-1 Fleet," *Advanced Composites*, Vol. 6, No. 5, Sept./Oct. 1991, pp. 18-20.
- [5] James Ott and Richard G. O'Lone, "737 Fuselage Separation Spurs Review of Safeguards," *Aviation Week & Space Technology*, Vol. 128, No. 19, May 9, 1988, pp. 92-95.
- [6] T. K. O'Brien, M. Rigamonti, and C. Zanotti, "Tension Fatigue Analysis and Life Prediction for Composite Laminates," *International Journal of Fatigue*, Vol. 11, No. 6, 1989, pp. 379-393.
- [7] A. Charewicz and I. M. Daniel, "Damage Mechanisms and Accumulation in Graphite/Epoxy Laminates," *Composite Materials: Fatigue and Fracture*, ASTM STP 907, H. T. Hahn, ed., American Society for Testing and Materials, Philadelphia, 1986, pp. 274-297.
- [8] S.L. Ogin, P.A. Smith, and P.W.R. Beaumont, "Matrix Cracking and Stiffness Reduction During the Fatigue of a (0/90)s GFRP Laminate," *Composite Science and Technology*, Vol. 22, 1985, pp. 23-31.
- [9] S.L. Ogin, P.A. Smith, and P.W.R. Beaumont, "A Stress Intensity Factor Approach to the Fatigue Growth of Transverse Ply Cracks," *Composite Science and Technology*, Vol. 24, 1985, pp. 47-59.
- [10] S.G. Lim and C.S. Hong, "Prediction of Transverse Cracking and Stiffness Reduction in Cross-Ply Laminated Composites," *Journal of Composite Materials*, Vol. 23, July 1989, pp. 695-713.

- [11] Norman Laws and George J. Dvorak, "Progressive Transverse Cracking In Composite Laminates," *Journal of Composite Materials*, Vol. 22, Oct. 1988, pp. 900-916.
- [12] K.N. Street, A.J. Russell and F. Bonsang, "Thermal Damage Effects on Delamination Toughness of a Graphite/Epoxy Composite", *Composites Science and Technology*, Vol. 32, No. 1, 1988, pp. 1-14.
- [13] Carl T. Herakovich and M.W. Hyer, "Damage-Induced Property Changes in Composites Subjected to Cyclic Thermal Loading," *Engineering Fracture Mechanics*, Vol. 25, Nos. 5/6, 1986, pp. 779-791.
- [14] P.G. Ermer and S. Mall, "Damage Mechanisms in a Unidirectional Metal Matrix Composite During Thermal Cycling," *American Society for Composites, Technical Conference*, 5th, East Lansing, MI, June 12-14, 1990, Proceedings (A91-26701 10-24). Lancaster, PA, Technomic Publishing Co., Inc., 1990, pp. 528-536.
- [15] K.E. Stansfield and E. Pritchard, "Damage Generation and Healing During Composite Thermal Spikes," *Proceedings of the International SAMPE Technical Conference*, 21st, Atlantic City, NJ, Sept. 25-28, 1989, pp. 120-129.
- [16] C.A. Griffis, J.A. Nemes, F.R. Stonesifer, and C.I. Chang, "Degradation in Strength of Laminated Composites Subjected to Intense Heating and Mechanical Loading," *Journal of Composite Materials*, Vol. 20, May 1986, pp. 216-235.
- [17] J.J. Schubbe and Shankar Mall, "Damage Mechanisms in a Cross-Ply Metal Matrix Composite Under Thermal-Mechanical Cycling," *Composites, Proceedings of the 8th International Conference on Composite Materials (ICCM8)*, Honolulu, HI, July 15-19, 1991. Section 12-21 (A92-32535 13-39). Covina, CA, Society for the Advancement of Material and Process Engineering, 1991, p. 20-B-1 to 20-B-9.
- [18] M.J. Salkind, "Early Detection of Fatigue Damage in Composite Materials," AIAA Paper No. 75-772, *AIAA/ASME/SAE 16th Structures, Structural Dynamics, and Materials Conference*, Denver, Colorado, May 27-29, 1975, pp. 1-8.
- [19] Wayne W. Stinchcomb, "Nondestructive Evaluation of Damage Accumulation Processes in Composite Laminates," *Composites Science and Technology*, Vol. 25, No. 2, 1986, pp. 103-118.
- [20] Isaac M. Daniel, Shi-Chang Wooh, and Jae-Won Lee, "Nondestructive Evaluation of Damage Development in Composite Materials," *Elastic Waves and Ultrasonic Nondestructive Evaluation*, S.K. Datta, J.D. Achenbach, and Y.S. Rajapakse, eds., Elsevier Science Publishers B.V., North Holland, 1990, pp. 183-189.

- [21] V. Dayal and V.K. Kinra, "Ultrasonic NDE of Composites for Transverse Cracking," *Optical Methods in Composites; Proceedings of the SEM Fall Conference on Experimental Mechanics*, Keystone, CO, Nov. 2-5, 1986 (A88-13876 03-24). Bethel, CT, Society for Experimental Mechanics, Inc., 1986, pp. 17-22.
- [22] B. Tang and E.G. Henneke, II, "Lamb-Wave Monitoring of Axial Stiffness Reduction of Laminated Composite Plates," *Materials Evaluation*, Vol. 47, Aug. 1989, pp. 928-934.
- [23] V. Dayal, V. Iyer, and V.K. Kinra, "Ultrasonic Evaluation of Microcracks in Composites," *Advances in Fracture Research; Proceedings of the Seventh International Conference on Fracture (ICF7)*, Houston, TX, Mar. 20-24, 1989. Vol. 5 (A90-41276 18-39). Oxford, England and Elmsford, NY, Pergamon Press, 1989, pp. 3291-3300.
- [24] Horace Lamb, "On Waves in an Elastic Plate," *Proceedings of the Royal Society of London*, Series A, Vol. XCIII, Oct. 1917, pp. 114,128.
- [25] D.C. Worton, "Ultrasonic Testing With Lamb Waves," *Nondestructive Testing*, July/August, 1957, pp. 218-222.
- [26] D.C. Worton, "Experimental Confirmation of Lamb Waves at Megacycle Frequencies," *Journal of Applied Physics*, Vol. 32, No. 6, June 1961, pp. 967-971.
- [27] M.R. Karim, A.K. Mal, and Y. Bar-Cohen, "Inversion of Leaky Lamb Wave Data by Simplex Algorithm," *Journal of the Acoustical Society of America*, Vol. 88, No. 4, July 1990, pp. 482-491.
- [28] Ajit K. Mal, Michael R. Gorman, and William H. Prosser, "Material Characterization of Composite Laminates Using Low-Frequency Plate Wave Dispersion Data," *Review of Progress in Quantitative Nondestructive Evaluation*, Vol. 11, D.O. Thompson and D.E. Chimenti, eds., Plenum Press, 1992, pp. 1451-1458.
- [29] C.C. Habeger, R.W. Mann, and G.A. Baum, "Ultrasonic Plate Waves in Paper," *Ultrasonics*, Vol. 17, March 1979, pp. 57-62.
- [30] R.A. Kline and M.M. Doroudian, "Ultrasonic Evaluation of Adhesively Bonded Composites Using Guided Waves," *Advances in Composite Materials and Structures (A91-23701 08-24)*, New York, American Society of Mechanical Engineers, 1989, pp. 63-67.
- [31] Paul N. Dewen and Peter Cawley, "An Ultrasonic Scanning Technique for the Quantitative Determination of the Cohesive Properties of Adhesive Joints," *Review of Progress in Quantitative Nondestructive Evaluation*, Vol. 11, D.O. Thompson and D.E. Chimenti, eds., Plenum Press, 1992, pp. 1253-1260.

- [32] M.J.S. Lowe and P. Cawley, "The Applicability of Plate Wave Techniques for the Inspection of Adhesive and Diffusion Bonded Joints," *Journal of Nondestructive Evaluation*, Vol. 13, No. 4, 1994, pp. 185-200.
- [33] Keun J. Sun, "Application of Guided Acoustic Waves to Delamination Detection," *Review of Progress in Quantitative Nondestructive Evaluation*, Vol. 11, D.O. Thompson and D.E. Chimenti, eds., Plenum Press, 1992, pp. 1213-1219.
- [34] N. Guo and P. Cawley, "The Interaction of Lamb Waves with Delaminations in Composite Laminates," *Journal of the Acoustical Society of America*, Vol. 94, No. 4, Oct. 1993, pp. 2240-2246.
- [35] Ningqun Guo and Peter Cawley, "Lamb Waves for the NDE of Composite Laminates," *Review of Progress in Quantitative Nondestructive Evaluation*, Vol. 11, D.O. Thompson and D.E. Chimenti, eds., Plenum Press, 1992, pp. 1443-1450.
- [36] Y. Bar-Cohen and D.E. Chimenti, "NDE of Defects in Composites Using Leaky Lamb Waves," *Symposium on Nondestructive Evaluation*, 15th, San Antonio, TX, April 23-25, 1985, Proceedings (A86-47129 22-38). San Antonio, TX, Nondestructive Testing Information Analysis Center, 1986, pp. 202-208.
- [37] Krishnan Balasubramaniam and Joseph L. Rose, "Guided Plate Wave Potential for Damage Analysis of Composite Materials," *Review of Progress in Quantitative Nondestructive Evaluation*, Vol. 9, D.O. Thompson and D.E. Chimenti, eds., Plenum Press, 1990, pp. 1505-1512.
- [38] Y.J. Lee, B.T. Khuri-Yakub, and K.C. Saraswat, "Temperature Measurements in Rapid Thermal Processing Using Acoustic Techniques," *Review of Scientific Instruments*, Vol. 65, No. 4, April 1994, pp. 974-976,
- [39] Jun Pei, F. Levent Degertekin, Butrus T. Khuri-Yakub, and Krishna C. Saraswat, "In Situ Thin Film Thickness Measurement with Acoustic Lamb Waves," *Applied Physics Letters*, Vol. 66, No. 17, April 24, 1995, pp. 2177-2179.
- [40] S.I. Rokhlin, "Resonance Phenomena of Lamb Waves Scattering by a Finite Crack in a Solid Layer," *Journal of the Acoustical Society of America*, Vol. 69, No. 4, April 1981, pp. 922-928.
- [41] S.K. Datta, W.M. Karunasena, and A.H. Shah, "Guided Waves in a Multilayered Composite and Ultrasonic Nondestructive Evaluation," *Composites; Proceedings of the 8th International Conference on Composite Materials (ICCM8)*, Honolulu, HI, July 15-19, 1991. Section 30-39 (A92-32535 13-39). Covina, CA, Society for the Advancement of Material and Process Engineering, 1991, pp. 39-E-1 to 39-E-10.

- [42] S.K. Datta, Y. Al-Nassar, and A.H. Shah, "Lamb Wave Scattering by a Surface-Breaking Crack in a Plate," *Review of Progress in Quantitative Nondestructive Evaluation*, Vol. 10, D.O. Thompson and D.E. Chimenti, eds., Plenum Press, 1991, pp. 97-104.
- [43] Robert Bratton, Subhendu Datta, and Arvind Shah, "Scattering of Lamb Waves in a Composite Plate," *Review of Progress in Quantitative Nondestructive Evaluation*, Vol. 10, D.O. Thompson and D.E. Chimenti, eds., Plenum Press, 1991, pp. 1507-1514.
- [44] Deborah D.L. Chung, *Carbon Fiber Composites*, Butterworth-Heinemann, Newton, MA, 1994.
- [45] Vicki P. McConnell, senior editor, "Demystifying Prepreg," *Advanced Composites*, Vol. 6, No. 5, Sept./Oct. 1991, pp. 53-55.
- [46] World Wide Web, http://axon.sgra.org/Organizations/Grumman/Products/Aircraft_Technologies/X-29.html, Sept. 30, 1995.
- [47] World Wide Web, <http://www.boeing.com/dsg.b-2.html>, Sept. 30, 1995.
- [48] World Wide Web, <http://www.boeing.com/dsg.darkstar.html>, April 24, 1996.
- [49] Tim Studt, "New Horizons for Aerospace," *R&D Magazine*, Vol. 38, No. 1, Jan. 1996, pp. 28-31.
- [50] "The Next Generation of Supersonic Airliners," *NASA Technology Today, Supplement to NASA Tech Briefs*, Vol. 20, No. 4, April 1996, pp. 2-5.
- [51] World Wide Web, <http://www.british-airways.com/bans/bworld/planes/conc.htm>, June 12, 1996.
- [52] NASA Innovations, "Green Machine," *NASA Tech Briefs*, Vol. 9, No. 10, Oct. 1995, p. 21.
- [53] J. Krautkrämer and H. Krautkrämer, *Ultrasonic Testing of Materials*, 4th Fully Revised Edition, Springer-Verlag, New York, 1990, p. 4.
- [54] Herbert Goldstein, *Classical Mechanics*, Second Edition, Addison-Wesley Publishing Company, Reading, MA, 1981, pp. 545-547.
- [55] B.A. Auld, *Acoustic Fields and Waves in Solids*, 2nd Edition, Vols. 1 and 2, Robert E. Krieger Publishing Company, Malabar, Florida, 1990.
- [56] Igor Aleksandrovich Viktorov, *Rayleigh and Lamb Waves*, Plenum Press, New York, 1967.

- [57] George Arfken, *Mathematical Methods For Physicists*, Third Edition, Academic Press, Inc., Harcourt Brace Jovanovich, Publishers, New York, 1985, pp. 78-83.
- [58] William H. Prosser, "The Propagation of Characteristics of the Plate Modes of Acoustic Emission Waves in Thin Aluminum Plates and Thin Graphite/Epoxy Composite Plates and Tubes," Ph.D. Thesis, The Johns Hopkins University, Nov., 1991.
- [59] S.B. Dong and K.H. Huang, "Edge Vibrations in Laminated Composite Plates," *Journal of Applied Mechanics*, Vol. 52, June 1985, pp. 433-438.
- [60] Subhendu K. Datta, A.H. Shah, and W. Karunasena, "Wave Propagation in Composite Media and Material Characterization," *Elastic Waves and Ultrasonic Nondestructive Evaluation*, S.K. Datta, J.D. Achenbach, and Y.S. Raja-pakse, eds., Elsevier Science Publishers B.V., North-Holland, 1990, pp. 159-167.
- [61] R.A. Kline, M.M. Doroudian, and C.P. Hsiao, "Plate Wave Propagation in Transversely Isotropic Materials," *Journal of Composite Materials*, Vol. 23, May 1989, pp. 505-533.
- [62] Adnan H. Nayfeh and D.E. Chimenti, "Free Wave Propagation in Plates of General Anisotropic Media," *Journal of Applied Mechanics*, Vol. 56, Dec., 1989, pp. 881-886.
- [63] A.K. Mal, C.-C. Yin, and Y. Bar-Cohen, "Ultrasonic Nondestructive Evaluation of Cracked Composite Laminates," *Composites Engineering*, Vol. 1, No. 2, 1991, pp. 85-101.
- [64] Ajit K. Mal, Shyh-Shiu Lih, and Yoseph Bar-Cohen, "Nondestructive Characterization of the Elastic Constants of Fiber Reinforced Composites," *34th AIAA/ASME/ASCE/AHS/ASC Structures, Structural Dynamics and Materials Conference*, La Jolla, CA, April 19-22, 1993, pp. 472-484.
- [65] M.G. Silk, *Ultrasonic Transducers for Nondestructive Testing*, Adam Hilger, Ltd., Bristol, 1984.
- [66] Erwin Meyer and Ernst-Georg Neumann, translated by John M Taylor, Jr., *Physical and Applied Acoustics*, Academic Press, New York and London, 1972, p. 8.
- [67] J.J. Ditri, A. Pilarski, B. Pavlakovic, and J.L. Rose, "Generation of Guided Waves in a Plate By Axisymmetric Normal Surface Loading," *Review of Progress in Quantitative Nondestructive Evaluation*, Vol. 13, D.O. Thompson and D.E. Chimenti, eds., Plenum Press, 1994, pp. 133-140.

- [68] Krishnan Balasubramaniam and Joseph L. Rose, "Physically Based Dispersion Curve Feature Analysis in the NDE of Composites," *Research in Nondestructive Evaluation*, Vol. 3, No. 1, 1991, Springer-Verlag, New York, Inc., pp. 41-67.
- [69] Caslini, M., Zanotti, C., and O'Brien, T.K., "Study of Matrix Cracking and Delamination in Glass/Epoxy Laminates," *Journal of Composites Technology & Research*, Vol. 9, No. 4, Winter 1987, pp. 121-130.
- [70] William H. Prosser, "Ultrasonic Characterization of the Nonlinear Elastic Properties of Unidirectional Graphite/Epoxy Composites," *NASA Contractor Report 4100*, NASA Langley Research Center, Oct., 1987, p. 65.
- [71] Ahmed K. Noor and Samuel L. Venneri, senior editors, "New and Projected Aeronautical and Space Systems, Design Concepts, and Loads," *Flight-Vehicle Materials, Structures, and Dynamics - Assessment and Future Directions*, Vol. 1, The American Society of Mechanical Engineers, New York, 1994, p. 84.
- [72] Sir Graham Sutton, *Mastery of the Air*, Basic Books, Inc., Publishers, New York, 1965, pp. 157-166.
- [73] Private communication with D.M. Heath, NASA Langley Research Center, Hampton, Virginia.
- [74] Ahmed K. Noor and Samuel L. Venneri, senior editors, "Advanced Metallics, Metal-Matrix, and Polymer-Matrix Composites," *Flight-Vehicle Materials, Structures, and Dynamics - Assessment and Future Directions*, Vol. 2, The American Society of Mechanical Engineers, New York, 1994, p. 15.
- [75] NIST Guide to Available Math Software, Fullsource for module CG from package SLATEC (EISPACK), Retrieved from CAMSUN on Sat Jun 3 13:23:12 1995.
- [76] John A.N. Lee, *Numerical Analysis for Computers*, Reinhold Publishing Corporation, New York, 1966, p. 165.

Vita

Michael David Seale

Born in Crawfordsville, Indiana, on November 9, 1967 to Carl R. and Patricia M. Seale. Graduated from North Montgomery High School in that city, May 1986. Graduated *Summa Cum Laude* from Wabash College, Crawfordsville, Indiana, with his B.A., May 1990. Received his M.S. in physics from the College of William and Mary, Williamsburg, Virginia in December 1991 and will receive his Ph.D. in physics from that same institute in August 1996. Has accepted a one-year appointment, starting the Fall of 1996, as an Assistant Professor of Physics at Wheeling Jesuit College, Wheeling, West Virginia.